SCUOLA DI DOTTORATO
UNIVERSITÀ DEGLI STUDI DI MILANO-BICOCCA

Dipartimento di / Department of

Materials Science

Dottorato di Ricerca in / PhD program: **Materials Science and Nanotechnology**

Ciclo / Cycle: **XXXVII**

Curriculum in (se presente / if it is): **Materials Science**

The Multifaceted Applications of ^{129}Xe NMR: Insights into Complex Systems from Structured Liquids to Catalysts

Cognome / Surname: Boventi Nome / Name: Matteo

Matricola / Registration number: 816320

Tutore / Tutor: Prof. Roberto Simonutti

Coordinatore / Coordinator: Prof. Francesco Cimbro Mattia Montalenti

ANNO ACCADEMICO / ACADEMIC YEAR 2023/2024

Contents

Abstract and structure of the work 7

1. Introduction to NMR Spectroscopy 11

1.1 NMR interactions 12

1.1.1 Zeeman interaction 12
1.1.2 Chemical shift 15
1.1.3 Dipolar interaction 16
1.1.4 *J*-coupling 18
1.1.5 Quadrupolar interaction 19
1.1.6 Interaction with a radiofrequency field 20

1.2 Relaxation 21

1.2.1 Spin-lattice relaxation 22
1.2.2 Spin-spin relaxation 24
1.2.3 Mechanisms of relaxation 26

1.3 Instrumental aspects of NMR 29

1.3.1 Fourier Transform and Time Domain NMR 29
1.3.2 Pulsed Field Gradient NMR 31

1.4 ^{129}Xe NMR Spectroscopy 34

1.4.1 Basic principles 34
1.4.2 ^{129}Xe chemical shift 35
1.4.3 Proposed chemical shift models for porous materials 38

1.5 Conclusions 41
1.6 Bibliography 42

2. Probing the structure of halomethanes with xenon 49

2.1 Introduction 49
2.2 Experimental section 53

2.2.1 Materials 53
2.2.2 Sample preparation 53
2.2.3 NMR spectroscopy 53
2.2.4 MD simulations 54
2.2.5 QM calculations 56

2.3 Results and discussion 57

2.3.1 ^{129}Xe NMR Spectroscopy 57
2.3.2 MD simulations and QM calculations 64

2.4 Conclusions 72
2.5 Bibliography 73

3. Exploring cavities in type II porous liquids with ^{129}Xe NMR 77

3.1 Introduction 77

3.2 Experimental section 84
3.2.1 Synthesis of Noria-OEt and preparation of type II PLs 84
3.2.2 Sample preparation 84
3.2.3 NMR Spectroscopy 85
3.3 Results and discussion 86
3.3.1 ^{129}Xe NMR at 298 K 86
3.3.2 Variable temperature ^{129}Xe NMR 92
3.3.3 Xenon relaxation and diffusion 94
3.4 Conclusions 96
3.5 Bibliography 98
4. Insights into the structure of type V deep eutectic solvents 103
4.1 Introduction 103
4.2 Experimental section 107
4.2.1 Materials 107
4.2.2 Binary mixtures preparation 107
4.2.3 NMR sample preparation 109
4.2.4 NMR spectroscopy 110
4.3 Results and discussion 111
4.3.1 Eutectic mixtures and deep eutectic solvents 111
4.3.2 Mixtures with variable compositions and comparisons 117
4.3.3 Variable temperature ^{129}Xe NMR chemical shifts 120
4.4 Conclusions 123
4.5 Bibliography 124
5. Characterization of hemp-derived electrocatalysts 131
5.1 Introduction 131
5.2 Experimental section 133
5.2.1 Preparation of hemp-derived electrocatalysts 133
5.2.2 Non-NMR physicochemical characterization of the electrocatalysts 135
5.2.3 ^{129}Xe NMR spectroscopy 137
5.3 Results and discussion 138
5.3.1 Synthesis of electrocatalysts 138
5.3.2 Non-NMR physicochemical characterization of electrocatalysts 139
5.3.3 ^{129}Xe NMR spectroscopy 148
5.4 Conclusions 161
5.5 Bibliography 163
6. General conclusions 169
List of publications 171
Acknowledgements 173

Abstract and structure of the work

Nuclear magnetic resonance (NMR) is a powerful and incredibly versatile spectroscopic technique that has found wide use in many different scientific disciplines, including chemistry, biology, physics, and medicine. The applications of NMR span an impressively broad variety, ranging, for example, from the structural elucidation of organic compounds to the study of protein folding in biology, from the investigation of the metabolic pathways of organisms to the study of the properties of complex materials and polymers, and from the analysis of contaminants and pollutants in environmental science to the imaging of human tissues.

The broad diversity of applications of this technique also encompasses the use of NMR-active noble gases as inert and non-invasive probes that are highly sensitive to their local environment. Among the various noble gas options, xenon-129 (^{129}Xe) stands out as the optimal choice due to its high natural abundance, remarkable inertness, and 1/2 nuclear spin. ^{129}Xe NMR has proven to be an invaluable tool for investigating the presence and characteristics of pores in solid-state materials, including pore size, shape, interconnectivity, hierarchy, and blocking. Moreover, it has also found applications in elucidating the structural organization and free volume of both simple and complex liquids, giving important information about their behavior at the molecular level.

In this work, we aimed to push the boundaries of ^{129}Xe NMR by performing a fundamental study on the interactions governing the NMR parameters of xenon dissolved in liquids, and, subsequently, by applying the technique to a wide range of neoteric liquid and solid-state materials.

The first Chapter of this Thesis offers an overview of the NMR technique by exploring the underlying physics of nuclear magnetic resonance. The different physical interactions experienced by nuclear spins immersed in a magnetic field are briefly described in terms of their Hamiltonians. Then, the phenomenon of NMR relaxation and its mechanisms are discussed, along with some instrumental aspects and NMR techniques, such as pulsed field gradient NMR. Lastly, the first Chapter introduces the reader to the ^{129}Xe NMR technique, outlining the basic principles and some of the physical models proposed over the years.

The fundamental research of Chapter 2 aims to deepen the understanding of the complex interactions governing the NMR parameters of xenon dissolved in isotropic liquids. To address this objective, the liquid structure of a series of dihalomethanes (CH_2X_2 with X = Cl, Br, I) was thoroughly investigated using a combination of computational and experimental NMR approaches. Variable temperature chemical shifts of the dissolved ^{129}Xe probe were measured. Additionally, room temperature spin-lattice relaxation times and diffusion coefficients were recorded. Molecular dynamics (MD) simulations of xenon in a bulk solvent were performed, and several clusters were extracted for density functional theory (DFT) calculations of the xenon shielding response. The combination of ^{129}Xe NMR measurements, molecular dynamics simulations, and quantum mechanical calculations enabled the rationalization of factors determining the NMR parameters of dissolved xenon, describing the interplay between the solvent's microscopic structural organization and its interaction with xenon atoms.

The computational calculations were performed by Valerio Mazzilli, PhD student under the supervision of Dr. Giacomo Saielli from the CNR Institute on Membrane Technology, Padova Unit.

Chapter 3 focuses on the application of ^{129}Xe NMR to the exploration of the porosity of porous liquids (PLs). These neoteric materials combine the flowability of liquids with the presence of permanent pores typical of rigid and organized solid-state structures. Their fluid nature makes traditional characterization techniques designed for porous solids difficult to apply. For example, the cryogenic conditions of N_2 sorption could alter the liquid structure, potentially leading to misleading results. Proving the existence of intrinsic pores as opposed to the transient ones typical of liquids is also challenging. In the field of PLs, ^{129}Xe NMR of dissolved xenon is a potentially powerful technique, as it is capable of probing both the intrinsic pores and the structural organization of liquids. Chapter 3 reports for the first time the application of ^{129}Xe NMR to a new type II PL, obtained using the known molecular paddlewheel Noria as a host, dissolved in the bulky solvent 15-crown-5. Xenon NMR parameters such as chemical shifts, relaxation times, and diffusion coefficients were measured across a series of PLs with varying host concentrations. These results enabled a detailed

description of the porous topology, paving the way for ^{129}Xe NMR as a characterization tool for porous liquids.

The synthetic procedures were performed by Dr. Francesca Alexander, a former PhD student in the group of Prof. Stuart L. James from the School of Chemistry and Chemical Engineering at Queen's University, Belfast.

In Chapter 4, we present the first application of xenon NMR to investigate the structure of type V deep eutectic solvents (DESs) and eutectic mixtures. These novel solvents have attracted significant attention due to their remarkable physical and chemical properties, affordability, environmental friendliness, and tunability. While DESs are applied in fields such as green chemistry, extraction, separation, electrochemistry, gas capture, and drug delivery, there has been less focus on understanding their thermodynamic non-ideality. A deeper understanding of how the structural organization of DESs relates to their physical properties could facilitate their development. To address this, Chapter 4 reports the xenon NMR analysis of menthol:thymol and thymol:camphor type V DESs, along with a series of menthol:carboxylic acid eutectic mixtures. This proof-of-concept study demonstrates how ^{129}Xe NMR can reveal valuable insights into the structural and dynamic properties of DESs, paving the way for developing structure-property relationships that explain their non-ideality.

Lastly, Chapter 5 reports the preparation and the structural characterization of novel electrocatalysts for oxygen reduction reaction in anion exchange membrane fuel cells. The electrocatalysts were produced starting from the two primary components of hemp stems: the hemp bast fibers, currently used in the textile industry due to their sustainability, and the hemp shives, the wooden refuse remaining after the removal of the fibers, which are usually discarded or used for low-value materials. From the hemp-based substrates, biochar was obtained by performing a controlled pyrolysis at different temperatures. This was followed by an activation step, and, subsequently, functionalization with iron phthalocyanine. The obtained electrocatalysts were characterized with various techniques, and their catalytic activity for the oxygen reduction reaction in a basic environment was measured, demonstrating their good

performances. The morphology and the porous structure were thoroughly studied by performing variable temperature ^{129}Xe NMR measurements on the materials obtained after every step of the electrocatalyst preparation. This allowed to explore the morphology of the starting and treated materials, providing information about the changes in morphology after activation and functionalization. The morphological features were also compared with the catalytic activity, demonstrating that homogeneous distributions of pores enhance the electrocatalytic performance due to a homogeneous distribution of the active sites combined with enhanced mass transport and accessibility.

The synthetic procedures and the non-NMR characterizations were performed by Dr. Leire Caizán-Juanarena, a former post-doctoral research fellow in the group of Prof. Carlo Santoro from the Department of Materials Science at the University of Milano-Bicocca, Milan.

1. Introduction to NMR Spectroscopy

Nuclear Magnetic Resonance (NMR) spectroscopy has been established as one of the most potent and valuable spectroscopic techniques. The widely different applications of NMR include but are not limited to, the precise structural elucidation of organic and inorganic compounds, the analysis of the morphology and phase-separation of polymeric and composite materials, the study of diffusion processes in solution and in the gas state, and the imaging of human tissues. Despite the high complexity of the instrumentation and the maintenance costs, NMR has nowadays become an essential technique in fundamental and applied research and many different industry sectors.

The basis of NMR is an intrinsic quantum mechanical property of the atomic nucleus: the spin. Every nucleus with a non-zero spin can be detected with NMR spectroscopy. Notably, the spin is correlated with the number of protons and neutrons in the nucleus. Different isotopes of the same element generally have different nuclear spins, and almost every nucleus of the periodic table has at least one NMR-active isotope, making it possible to analyze widely different materials, from organic molecules and polymers to inorganic and hybrid materials. The most studied nucleus with NMR spectroscopy is by far ^{1}H, thanks to its very high natural abundance and its ubiquity in a plethora of different systems. Other common nuclei include ^{13}C, ^{19}F, ^{29}Si, and ^{31}P, thanks to their high natural abundance and/or their 1/2 nuclear spin. Among the endless applications of NMR spectroscopy lies the possibility to use NMR-active gaseous nuclei as non-destructive probes to study the morphology of porous solid-state materials and the structural organization of simple isotropic liquids and complex nano-segregated liquid systems such as ionic liquids and deep eutectic solvents. One of the best nuclei for this purpose is ^{129}Xe, thanks to its very high sensitivity to the local environment coupled with the inertness typical of noble gases.

This Chapter will give a very brief introduction to the complex quantum mechanical interactions involved in the phenomenon of nuclear magnetic resonance and NMR relaxation, along with some instrumental aspects of the technique. Then, it will address the basic principles of ^{129}Xe NMR, the main technique of this Thesis work, some history of the technique, and some proposed models for its application on different types of materials. This chapter aims to give a brief overview of some

fundamental aspects of NMR spectroscopy and ^{129}Xe NMR. Complete descriptions of the physical phenomena and the instrumental aspects of NMR can be found in the following references and in references therein,[1–5] while ^{129}Xe NMR is illustrated in detail in the following review articles.[6–11]

1.1 NMR interactions

NMR spectroscopy is based on the interactions of nuclear spins with the surrounding environment. From a quantum-mechanical point of view, the total Hamiltonian experienced by any spin system can be expressed by a sum of different Hamiltonians, each representing a single interaction.[12–14]

$$\mathbf{H}_{\mathrm{NMR}} = \sum_{\lambda} \mathbf{H}_{\lambda} \tag{1.1}$$

Where λ represents the individual interactions. The following sections will give a brief description of the interactions involved in nuclear magnetic resonance.

1.1.1 Zeeman interaction

Any nucleus with an odd number of protons and/or neutrons possesses a non-null angular momentum, called nuclear spin. This is described by a nuclear spin vector, $\vec{\mathbf{I}}$, and a nuclear spin quantum number, I, which is a fixed property for each nucleus, and can be either an integer or a half-integer. The nuclear spin is associated with the intrinsic nuclear magnetic moment, $\vec{\boldsymbol{\mu}}$, which assumes the following values

$$\vec{\boldsymbol{\mu}} = \gamma \hbar \vec{\mathbf{I}} \tag{1.2}$$

where γ is the gyromagnetic ratio of the nucleus and $\hbar$ is the reduced Planck constant.

The interaction of a nuclear spin with an external static magnetic field is called Zeeman interaction, and it is described by the following Hamiltonian

$$\mathbf{H}_{\mathbf{Z}} = -\gamma \hbar \vec{\mathbf{I}} \cdot \vec{\mathbf{B}}_0 \tag{1.3}$$

where $\vec{\mathbf{B}}_0$ is the external static magnetic field vector. Normally the coordinates are set so that $\vec{\mathbf{B}}_0$ is always aligned along the *z*-axis, and it has no components on the *xy*-plane. Under the effect of the external magnetic field, the *z* component of the nuclear magnetic moment, aligned in the field direction, assumes the following, discrete values

$$\mu_Z = m\hbar\gamma \tag{1.4}$$

where *m* can take any integer value from -*I* to +*I* (*m* = -*I*, -*I* + 1, …, *I* - 1, *I*). The energy associated with each discrete value of μ_Z is given by

$$E_m = -\mu_Z B_0 = -m\gamma\hbar B_0 \tag{1.5}$$

Here, B_0 is the magnitude of the *z* component of the vector $\vec{\mathbf{B}}_0$.

In the absence of an external magnetic field, the energy levels associated with the different values of the quantum number *m* are degenerate. The effect of the Zeeman Hamiltonian is to create $2I + 1$ non-degenerate energy levels whose separation is proportional to the external magnetic field, as represented schematically in Figure 1.1 for a nucleus with $I = 3/2$.

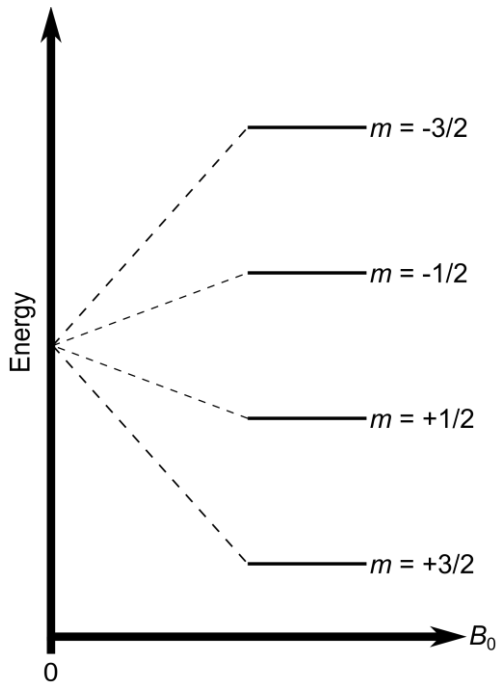

Figure 1.1. Schematic representation of the Zeeman splitting for a spin-3/2 nucleus.

The separation between two consecutive energy levels can be easily calculated with Equation (1.5):

$$\Delta E = \gamma \hbar B_0 = \hbar \omega_0 \tag{1.6}$$

Equation (1.6) indicates that the transitions between the energy levels must be excited with photons of frequency ω_0, which is called Larmor frequency and is on the order of the radio frequencies. The energy separation between the levels and, thus, the Larmor frequency, depend on both the gyromagnetic ratio of the nucleus and the strength of the external magnetic field. Indeed, it has become standard among scientists to indicate the strength of the magnetic fields generated by the NMR magnets with the Larmor frequency of the ^{1}H nucleus. For example, in an 11.75 T magnet, the Larmor frequency of ^{1}H is 500.13 MHz, and scientists would call this a 500 MHz magnet.

When an ensemble of N nuclei is embedded in a magnetic field, the occupation of the different energy levels follows the Boltzmann distribution:

$$\frac{N_{m+1}}{N_m} = \exp\left(-\frac{\Delta E}{kT}\right) \approx 1 - \frac{\Delta E}{kT} = 1 - \frac{\gamma \hbar B_0}{kT} \tag{1.7}$$

where N_{m+1} and N_m are the number of nuclear spins in the states m+1 and m, respectively, $k = 1.3805 \times 10^{-23}$ J K^{-1} is the Boltzmann constant, and T is the absolute temperature in Kelvin. The linear approximation in Equation (1.7) is allowed because NMR is a low-energy spectroscopy in which $\Delta E << kT$. This also means that, generally, the population mismatch in NMR is very limited. However, this mismatch is enough to create a macroscopic and detectable magnetization along the z-axis, which means, parallel to the external magnetic field. The macroscopic magnetization is represented by the total magnetic moment operator, $\vec{\mathbf{M}}$, defined as

$$\vec{\mathbf{M}} = \hbar \sum_{i}^{spins} \gamma_i \vec{\mathbf{I}}_i \tag{1.8}$$

1.1.2 Chemical shift

As illustrated previously, the Zeeman interaction only depends on the intrinsic properties of the nucleus, the nuclear spin and the gyromagnetic ratio, and on the strength of the external magnetic field. This interaction, albeit essential for the nuclear magnetic resonance phenomenon, does not constitute the main interest of NMR scientists. The interactions of interest are those that drive the frequencies needed to excite the spin transitions slightly away from the Larmor frequency. Among those, the most important is undoubtedly the chemical shift interaction.

Since electrons are charged particles with a non-null spin, when they are in the presence of an external magnetic field their motion generates a very small, localized, and anisotropic magnetic field. As a consequence of this phenomenon, nuclear spins experience an effective magnetic field that is strongly dependent on the surrounding local environment.

The interaction of a nuclear spin with the induced magnetic field created by the surrounding electrons is described by the chemical shift Hamiltonian.

$$\mathbf{H_{CS}} = \gamma\hbar\vec{\mathbf{I}} \cdot \hat{\boldsymbol{\sigma}} \cdot \vec{\mathbf{B}}_0 \tag{1.9}$$

where $\hat{\boldsymbol{\sigma}}$ is the chemical shift tensor. This is a rank 2 tensor that takes the form of a 3×3 matrix since the chemical shift is an anisotropic, orientation-dependent parameter.

There are several methods to determine the components of the chemical shift tensor including, but not limited to, solid-state NMR measurements on single crystals or oriented liquid crystalline samples, analysis of solid-state NMR powder pattern spectra, and quantum-chemical calculations.[15] In the case of crystalline and polycrystalline samples. knowledge of the chemical shift tensor allows to precisely elucidate the crystal structure. In solution-state NMR, the fast molecular motions average the chemical shift tensor to its isotropic value. This simplifies both the theoretical treatment and the analysis of solution-state NMR spectra compared to solid-state NMR.

By comparing Equation (1.9) to Equation (1.3), it can be seen that the effect of the chemical shift interaction is to shift the Zeeman Hamiltonian by a quantity equal to the chemical shift tensor (or the shielding constant in the case of solution-state NMR). This translates to a slight shift of the resonant frequency of the photons needed to excite the

spin transitions away from the Larmor frequency. Even though this shift is very small (the orders of magnitude of the chemical shift and Zeeman interactions are 10^3 Hz and 10^8 Hz, respectively), modern high-resolution instruments can measure the differences in the resonant frequency with extremely high precision. Generally, the chemical shift tensor is different for each nucleus. Thus, the chemical shift is the reason why NMR spectroscopy has become a standard technique in many research fields and in companies where structural elucidation and molecular characterization are required.

1.1.3 Dipolar interaction

The dipolar interaction, also known as dipolar coupling, is a direct spin-spin interaction between two different nuclei. For a pair of nuclear spins 1 and 2 separated by a distance r, the dipolar Hamiltonian is the following

$$\mathbf{H_D} = \frac{\mu_0 \gamma_1 \gamma_2 \hbar^2}{4\pi} [(\vec{\mathbf{I}}_1 \cdot \vec{\mathbf{I}}_2) r^{-3} - 3(\vec{\mathbf{I}}_1 \cdot \vec{\mathbf{r}})(\vec{\mathbf{I}}_2 \cdot \vec{\mathbf{r}}) r^{-5}] \tag{1.10}$$

where $\mu_0 = 4\pi \times 10^{-7}$ N A^{-2} is the vacuum magnetic permeability, and γ_1 and γ_2 are the gyromagnetic ratios of nuclei 1 and 2, respectively. The distance vector can also be written in terms of the polar coordinates.

$$\vec{\mathbf{r}} = (r_x, r_y, r_z) = (r\sin\theta\cos\varphi, r\sin\theta\sin\varphi, r\cos\theta) \tag{1.11}$$

where θ and φ are the polar angle and the azimuthal angle, respectively. This form of the distance vector leads to the common expression of the dipolar Hamiltonian in terms of the so-called dipolar alphabet:

$$\mathbf{H_D} = \frac{\mu_0 \gamma_1 \gamma_2 \hbar^2}{4\pi r^3} [A + B + C + D + E + F] \tag{1.12}$$

with

$$A = \hat{I}_{1z}\hat{I}_{2z}(1 - 3\cos^2\theta) \tag{1.13}$$

$$B = -\frac{1}{4}[\hat{I}_1^+\hat{I}_2^- + \hat{I}_1^-\hat{I}_2^+](1 - 3\cos^2\theta) \tag{1.14}$$

$$C = -\frac{3}{2}[\hat{I}_1^+ \hat{I}_{2z} + \hat{I}_{1z}\hat{I}_2^+]\sin\theta\cos\theta e^{-i\varphi} \quad (1.15)$$

$$D = -\frac{3}{2}[\hat{I}_1^- \hat{I}_{2z} + \hat{I}_{1z}\hat{I}_2^-]\sin\theta\cos\theta e^{i\varphi} \quad (1.16)$$

$$E = -\frac{3}{4}\hat{I}_1^+ \hat{I}_2^+ \sin^2\theta\, e^{-2i\varphi} \quad (1.17)$$

$$F = -\frac{3}{4}\hat{I}_1^- \hat{I}_2^- \sin^2\theta e^{2i\varphi} \quad (1.18)$$

where $\hat{I}_{1z}$ and $\hat{I}_{2z}$ are operators representing the z components of the nuclear spin operators for spin 1 and 2, respectively, while $\hat{I}_1^+ = \hat{I}_{1x} + i\hat{I}_{1y}$ and $\hat{I}_1^- = \hat{I}_{1x} - i\hat{I}_{1y}$ are so-called raising and lowering operators for spin 1 (the operators for spin 2 have an analogous expression). The terms C, D, E, and F can generally be neglected in high external magnetic fields since the secular approximation can be applied and these terms do not commute with the Zeeman Hamiltonian. The term B must be considered only if spins 1 and 2 are like, that is in the case of homonuclear dipolar coupling. When treating heteronuclear dipolar coupling, this term can be neglected. On the other hand, the term A must always be considered.

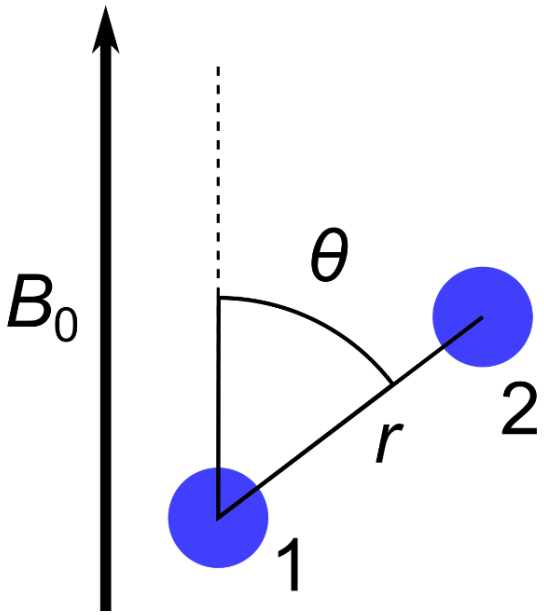

Figure 1.2. Schematic representation of the orientational dependence of the dipolar coupling between two spins 1 and 2.

Notably, both terms A and B have an orientational dependence with respect to the external magnetic field given by the term $3\cos^2\theta - 1$, which is similar to a second-order Legendre polynomial $P_2(\cos\theta)$. The orientational dependence of the dipolar coupling is illustrated schematically in Figure 1.2.

In the case of isotropic liquids, the fast and random molecular tumbling averages the polar angle θ, and thus the dipolar interaction, to zero. On the other hand, in solid-state samples, the effect of the dipolar interaction is to induce a splitting of the energy levels of the coupled spins. By thoroughly analyzing the features of the dipolar interaction, it is possible to obtain valuable structural information, especially in the case of crystalline systems.[16–18]

The magnitude of the dipolar interaction is often expressed in terms of the dipolar coupling constant, D_{12}. When considering an average over all possible orientations, the dipolar coupling constant is given by Equation (1.19).

$$D_{12} = \frac{\mu_0 \gamma_1 \gamma_2 \hbar}{4\pi r^3} \tag{1.19}$$

The dipolar interaction has the same order of magnitude as the chemical shift (about 10^3 Hz) and, thus, it is much smaller than the Zeeman interaction.

1.1.4 *J*-coupling

The *J*-coupling, sometimes also called indirect spin-spin interaction, is a mutual spin pair interaction by which the information on the state of a nuclear spin is transmitted to the other via the bonding electrons of the spin system. The *J*-coupling Hamiltonian between two spins 1 and 2 is

$$\mathbf{H_J} = h\vec{\mathbf{I}}_\mathbf{1} \cdot \hat{\mathbf{J}} \cdot \vec{\mathbf{I}}_\mathbf{2} \tag{1.20}$$

where $\hat{\mathbf{J}}$ is a 3x3 matrix called the scalar coupling tensor.

Like the dipolar coupling, in principle, the *J*-coupling also depends on the molecular orientation. However, its anisotropy is difficult to observe because it is only appreciable in strongly aligned media, and it is often suppressed by the stronger dipolar coupling.[19–21] Unlike the dipolar coupling, the *J*-coupling is not averaged to zero in isotropic liquids. Instead, the fast motion averages out the spatial components of the

interaction, reducing the tensor to a single number called the coupling constant. In this case, the interaction becomes isotropic, and it is called scalar interaction. The terms *J*-coupling and scalar interaction are often used interchangeably. However, formally the scalar coupling is only the isotropic component of the *J*-coupling.

The net effect of the *J*-coupling is to perturb the energy levels of the nucleus. When the perturbing nucleus is in one spin state, the observed nucleus has its energy level slightly lowered, while the energy is slightly increased when the perturbing nucleus is in the other spin state. This energy difference is commonly expressed in terms of frequency. Its value is usually between 1 Hz and 100 Hz, and it does not depend on the intensity of the external magnetic field.

This interaction gives rise to a fine structure even in the spectra of very simple molecules. This severely complicates the interpretation of NMR spectra but, on the other hand, it constitutes a very powerful source of information regarding molecular connectivity and spatial conformation.

1.1.5 Quadrupolar interaction

Nuclei with spin higher than 1/2, called quadrupolar nuclei, have an asymmetric charge distribution which allows them to interact with the surrounding electric field gradient. This is called quadrupolar interaction, and it is the most intense NMR interaction (excluding the Zeeman interaction), having an order of magnitude of 10^6 Hz. This interaction is described by the quadrupolar Hamiltonian.

$$\mathbf{H_Q} = \frac{eQ}{2I(2I - 1)\hbar}\, \vec{\mathbf{I}} \cdot \hat{\mathbf{V}} \cdot \vec{\mathbf{I}} \tag{1.21}$$

where $e = 1.60 \times 10^{-19}$ C is the elementary charge, Q is the electric quadrupolar moment, and $\hat{\mathbf{V}}$ is the electric field gradient tensor.

The quadrupolar interaction severely complicates the NMR spectra of nuclei with spin greater than 1/2, resulting in very broad peaks even for simple systems. These nuclei constitute more than 2/3 of the NMR-active nuclei. In the last few decades, much effort has been devoted to the development of quadrupolar NMR techniques. Additional details about these approaches can be found in the following references and in references therein.[16,22–25]

1.1.6 Interaction with a radiofrequency field

The NMR interactions described so far result from embedding nuclear spins in an external magnetic field, B_0. It has been shown how the energy levels of a nuclear spin lose their degeneracy due to the Zeeman interaction, and how they are further perturbated by the other interactions. The nuclear spins distribute inside the energy levels established by these interactions, following a Boltzmann distribution with a very limited population mismatch (see Section 1.1.1).

In NMR spectroscopy, the excitation to higher energy levels is obtained by applying an oscillating magnetic field with an appropriate frequency in a direction perpendicular to the static magnetic field. The oscillating magnetic field is commonly indicated as B_1, and its frequency is in the radiofrequency range. The interaction between a nuclear spin and a radio-frequency field with angular frequency Ω_{rf} and phase angle ϕ is described by the following time-dependent Hamiltonian.[13]

$$\mathbf{H_{RF}}(t) = - \gamma\hbar B_1\left[\hat{I}_x\cos(\Omega_{rf}\, t - \phi) \; - \hat{I}_y \sin(\Omega_{rf}\, t - \phi)\right] \tag{1.22}$$

When considering an ensemble of spins, this Hamiltonian can be rewritten in terms of the total magnetic moment operator defined in Equation (1.8):

$$\mathbf{H_{RF}}(t) = - \hbar B_1\left[\widehat{M}_x\cos(\Omega_{rf}\, t - \phi) \; - \widehat{M}_y \sin(\Omega_{rf}\, t - \phi)\right] \tag{1.23}$$

The net effect of this Hamiltonian is a rotation of $\widehat{M}_x$ about the z-axis by an angle $(\Omega_{rf}\, t - \phi)$. Recall that in equilibrium conditions the net magnetization is aligned along the z-axis (see Section 1.1.1). This means that there are no components on the xy-plane. The effect of the radiofrequency pulse is to rotate the magnetization toward the xy-plane, converting part of the net magnetization into x and y components. After the radiofrequency pulse is applied, the nuclear spins return to their original, unperturbed state by a process called relaxation: the magnetization returns along the z-axis following a spiral motion (see Section 1.2). The precessing magnetization in the xy-plane induces a detectable signal, called free induction decay or FID. This phenomenon is called nuclear magnetic resonance. The FID is detected as an oscillating voltage in a detection coil surrounding the sample.

Equation (1.23) shows that it is possible to modulate the rotation angle by changing the intensity of the oscillating magnetic field, the angular frequency, the phase angle, or the radiofrequency pulse application time. NMR pulses are commonly indicated with their rotation angles in degrees or in radians (i.e. a 90° or $\pi/2$ pulse). Usually, the phase of the pulse is also indicated as a subscript. For example, $(90°)_x$ represents a pulse that tilts the magnetization by 90°, applied along the $+x$ direction. The most common rotation angles are 90° and 180°. These pulses bring the magnetization from the z-axis on the xy-plane and along $-z$, respectively, following a direction determined by the pulse phase.

The simplest NMR experiment involves the application of a single 90° pulse, followed by the detection of the signal. Complex experiments make use of selected multiple pulses separated by carefully chosen time delays. These pulse sequences allow to excite only the desired transitions, giving rise to a specific form of NMR signal which only contains the required information. To achieve this, it is mandatory to repeat the pulse sequences several times, changing the phase of the pulses properly. This practice, called phase cycling, also eliminates several artifacts that can make NMR spectra uninterpretable.[26,27]

NMR pulse sequences and phase cycles are commonly treated using the product operator formalism. An in-depth discussion of this formalism is beyond the objective of this work. More information can be found in these references and in references therein.[2,28–30]

1.2 Relaxation

After the excitation via a radiofrequency (RF) pulse, the nuclear spin system slowly returns to equilibrium, reestablishing the populations of the energy levels predicted by the Boltzmann distribution, and eliminating any xy-component of the magnetization. This process is called relaxation, and, naturally, it involves transitions between different energy levels. As described previously, NMR transitions are caused by appropriate magnetic fields in the xy-plane. There is an important difference between the transitions caused by RF pulses and those involved in relaxation. When an RF pulse is applied, all the nuclear spins experience the same oscillating magnetic field, B_1 (see Section 1.1.6).

In other words, the RF pulse gives phase coherence to the nuclear spins, generating a detectable transverse magnetization (see Section 1.2.2). On the other hand, the transitions involved in relaxation are caused by transverse magnetic fields that affect only a small portion of the nuclear spins. These fields are generated in the sample itself due to interactions between nuclear spins or between spins and the surrounding environment. Due to molecular motion, these fields are random and time-dependent. The fluctuations of these fields can be expressed in terms of an autocorrelation function to which a characteristic time, called correlation time, is associated. A complete description of the correlation time and its effect on the NMR relaxation falls outside the scope of this work. However, in simple and qualitative terms, it can be said that relaxation processes are most efficient when the molecular motion occurs on time scales comparable to the Larmor frequency or, in other words, when the correlation time is close to the inverse of the Larmor frequency. This is the reason why relaxation strongly depends on molecular mobility. Indeed, NMR relaxometry is widely used to study molecular mobility and all the properties that depend on molecular motion.

As mentioned in Section 1.1.6, during relaxation the magnetization follows a spiral motion to return along the *z*-axis, that is, at the equilibrium condition. At the end of the spiral motion, the *z* component of the magnetization has returned to its original value, and the component in the *xy*-plane, also called the transverse magnetization, has returned to zero. Thus, relaxation is separated into two different processes, each with its own time constant: the spin-lattice or longitudinal relaxation, and the spin-spin or transversal relaxation.

1.2.1 Spin-lattice relaxation

Spin-lattice or longitudinal relaxation is the process by which the *z* component of the magnetization returns to its equilibrium value. The name spin-lattice does not refer to the crystalline lattice of solids. Instead, it refers to the surrounding environment of the nuclear spins with which energy is exchanged.

The motion of the *z* component of the magnetization, M_z, during spin-lattice relaxation, can be described by the following equation.

$$M_z(t) = M_z^0 - \left[M_z^0 - M_z(0)\right] \exp\left(-\frac{t}{T_1}\right) \tag{1.24}$$

M_z^0 is the equilibrium value of z magnetization, and $M_z(0)$ is the z magnetization when $t = 0$. This equation is derived from the Bloch equations originally proposed by Felix Bloch.[31] Equation (1.24) shows that the z magnetization returns to the equilibrium value following an exponential law with a time constant T_1, called spin-lattice or longitudinal relaxation time. This corresponds to the time that the z magnetization needs to recover 1 – 1/e (i.e. approximately 63%) of its equilibrium value.

The spin-lattice relaxation time can be measured using the Inversion Recovery (INVREC) pulse sequence, represented in Figure 1.3.

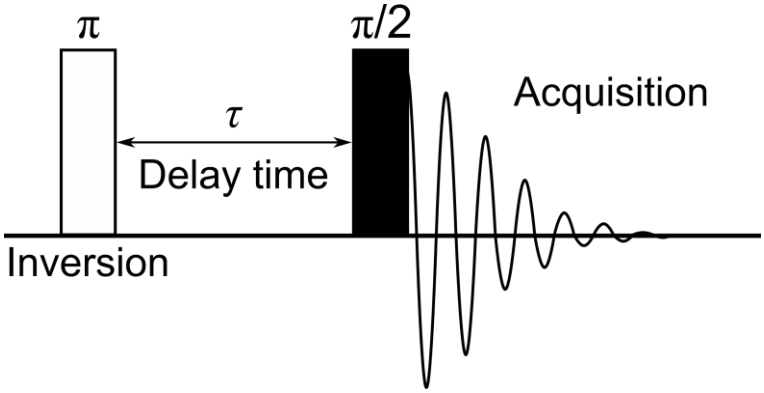

Figure 1.3. Inversion Recovery (INVREC) pulse sequence.

This sequence starts with a π pulse that rotates the equilibrium magnetization along the $-z$ direction. Then, after a delay τ, during which relaxation takes place, the remaining magnetization is flipped onto the xy-plane by a $\pi/2$ readout pulse, where it can be detected by the receiving coils. If the delay τ is short, the magnetization still lays along the $-z$ direction when the readout pulse is applied. On the other hand, if τ is long enough the magnetization returns along the $+z$ direction before the acquisition. Thus, the signals detected with short and long delays have opposite phases: if the former is negative, the latter will be positive. When using this pulse sequence, the motion of the z magnetization can be described by a special case of Equation (1.24) with $M_z(0) = - M_z^0$.

$$M_z(t) = M_z^0 \left[1 - 2 \exp\left(-\frac{t}{T_1}\right)\right] \tag{1.25}$$

The T_1 value is obtained by repeating the pulse sequence with increasing delay times and fitting the obtained intensities with Equation (1.25).

1.2.2 Spin-spin relaxation

As described previously, at equilibrium the individual *xy*-components of the nuclear spins cancel out to zero and the magnetization is aligned along the *z*-axis. The application of a radiofrequency pulse tilts the magnetization towards the *xy*-plane, generating phase coherence which translates into observable transverse magnetization. In other words, the radiofrequency pulse gives a preferential direction to the *xy*-components of the single nuclear spins. When these components are added together, the result is a non-null transverse magnetization component. During spin-spin relaxation, the transverse magnetization decays due to coherence loss. In simple and non-rigorous terms, the transverse magnetizations progressively lose their preferential direction while precessing around the z-axis, returning to the equilibrium conditions where the net transverse magnetization is zero. In contrast to spin-lattice relaxation, this process only involves interactions between spins at the same energy level, and no energy is exchanged with the surrounding environment.

There are two main mechanisms by which the loss of coherence can happen. The first is the interaction with local oscillating magnetic fields that randomly alter the phase of the transverse magnetizations. These transitions are caused by the various mechanisms described in Section 1.2.3. They are also the mechanisms by which spin-lattice relaxation happens. Thus, every mechanism that causes spin-lattice relaxation also causes spin-spin relaxation. The second is the different precession rates of the magnetization vectors which is a result of them having slightly different Larmor frequencies. The differences in the Larmor frequencies are due to the different local magnetic fields experienced by every nuclear spin. However, in this case the local magnetic fields do not need to oscillate over time, but they just need to be different throughout the molecule.

The behavior of the transverse magnetization, M_{xy}, as a function of time is given by the following equation.

$$M_{xy}(t) = M_{xy}(0) \exp\left(-\frac{t}{T_2}\right) \tag{1.26}$$

$M_{xy}(0)$ is the transverse magnetization at $t = 0$. The decay of the transverse magnetization to zero is exponential with a time constant T_2, the spin-spin or longitudinal relaxation time. After T_2, the magnetization has decayed to 1/e of its initial value, which roughly corresponds to 37%.

In principle, the spin-spin relaxation time could be obtained by simply fitting the FID intensities with Equation (1.26). However, the inhomogeneities in the static magnetic fields generated even by modern NMR instruments enhance spin-spin relaxation. The net effect is that the exponential decay of the FID is faster than the decay of an ideal spin-spin relaxation process. The time constant of the FID decay is usually indicated as T_2*, and its relation to T_2 is

$$\frac{1}{T_2^*} = \frac{1}{T_2} + \frac{1}{T_{2,i}} = \frac{1}{T_2} + \gamma \Delta B_0 \tag{1.27}$$

where $T_{2,i}$ is the relaxation contribution attributable to magnetic field inhomogeneities, ΔB_0. Equation (1.27) shows that T_2* is always smaller than T_2. Moreover, the T_2* of a certain resonance is inversely proportional to the full width at half-maximum of the corresponding NMR peak (see Section 1.3.1).

The measurement of the spin-spin relaxation time requires an appropriate pulse sequence capable of eliminating the effects of the magnetic field inhomogeneities. The simplest of these sequences is the Hahn echo pulse sequence, illustrated in Figure 1.4.[32] The sequence consists of a $\pi/2$ pulse, followed by a delay τ and a π pulse. The first pulse generates a transversal magnetization component which then starts precessing around the z axis during the delay τ. Here, the different nuclear spins precess at different rates due to magnetic field inhomogeneities that slightly change their resonant frequencies. At the end of the delay, a π pulse inverts the nuclear spins. This removes the effect of inhomogeneous dephasing and results in a signal showing after another delay time τ, called a spin echo. T_2 is obtained by performing a series of experiments with increasing the delay time and fitting the measured intensities of the spin echoes with Equation (1.26).

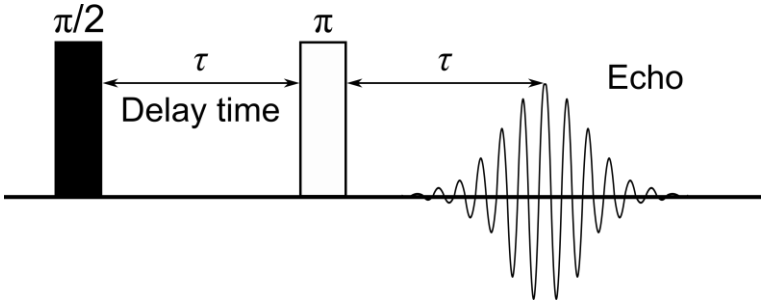

Figure 1.4. Hahn Echo pulse sequence.

Another common method for the measurement of the spin-spin relaxation time is the Carr-Purcell-Meiboom-Gill (CPMG) pulse sequence, illustrated in Figure 1.5.[33] This sequence consists of a Hahn echo followed by a train of equally spaced π pulses. Multiple spin echoes are formed and acquired at a time τ after each π pulse. When measuring T_2, CPMG is faster than Hahn echo because only a single experiment needs to be performed. Moreover, the CPMG sequence is less affected by the translational motions that can occur during the delay time due to the use of multiple π pulses. However, the multiple pulses in the CPMG sequence make it significantly sensitive to instrumental imperfections such as inaccuracies in the flip angles and timing errors.

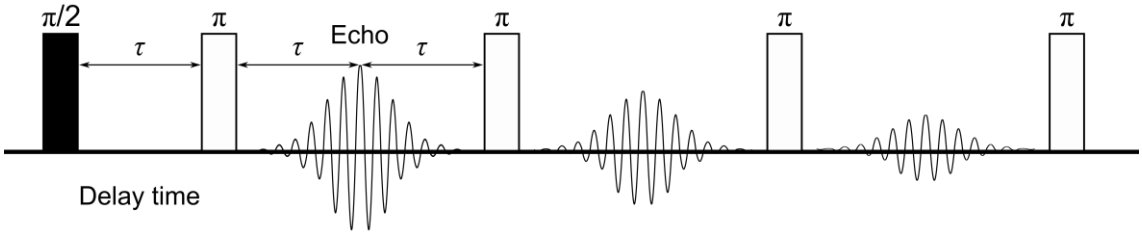

Figure 1.5. Carr-Purcell-Meiboom-Gill (CPMG) pulse sequence.

Both Hahn echo and CPMG can be combined with other pulse sequences to purge the magnetization from inhomogeneous dephasing.

1.2.3 Mechanisms of relaxation

The previous sections described the general concepts of NMR relaxation and the distinction between spin-lattice and spin-spin relaxation, along with some experimental methods to measure T_1 and T_2. This section will briefly describe the various possible

mechanisms of relaxation, that is, the origins of the local random magnetic fields that induce the transitions leading to relaxation.

1.2.3.1 Dipolar relaxation

Dipolar relaxation is by far the most common mechanism for small nuclei with spin 1/2 (^{1}H, ^{13}C, ^{29}Si) immersed in not too large static magnetic fields. Section 1.1.1 describes how every nuclear spin is related to an intrinsic nuclear magnetic moment. This generates a small local magnetic field that can interact with other nuclear spins close in space. As described in Section 1.1.3, this is called dipolar interaction, and its quantum mechanical description is given by the dipolar Hamiltonian. Equation (1.10) shows how this Hamiltonian depends on the vector distance between the two nuclei. As random molecular motions occur, the magnitude and/or the direction of the distance vector change, leading to a change in the magnitude of the dipolar interaction and in the local magnetic fields experienced by the interacting nuclear spins.

Notably, molecular vibrations occur at too high frequencies to have an observable effect on relaxation: their effect is only seen as an average of all the possible internuclear distances assumed during the vibrational motion. On the other hand, molecular reorientations have a great effect on relaxation since they generally occur at a frequency comparable to the NMR time scale (around the Larmor frequency).

The magnitude of the dipolar relaxation is proportional to the square of the dipolar coupling constant defined in Equation (1.19).[2] Moreover, the pair of interacting nuclei can belong to the same molecule (intra-molecular) or different molecules (inter-molecular).

1.2.3.2 Chemical shift anisotropy relaxation

It has been shown in Section 1.1.2 that the local magnetic fields generated by electrons slightly alter the magnetic field experienced by nuclear spins. Equation (1.9) shows that this interaction is orientation-dependent since it is determined by a tensorial quantity, the chemical shift tensor. This means that the magnetic field experienced by a nuclear spin not only depends on the strength of the applied magnetic field but also on the relative orientation of the molecule. Molecular reorientation results in slight changes in the magnetic fields experienced by the nuclear spins. The time scale of these variations

is appropriate to cause relaxation. This mechanism is called chemical shift anisotropy (CSA) relaxation.

When molecules are rapidly reorientating, the chemical shift tensor is averaged to its isotropic component, and the chemical shift anisotropy relaxation is negligible. On the other hand, when molecular motion is restricted, CSA effects may play a significant role on relaxation. CSA relaxation scales with the square of the applied magnetic field, B_0^2. It is directly proportional to the size of the shift anisotropy, which can be roughly estimated from the typical chemical shift range of a nucleus. Thus, CSA relaxation is important for nuclei with broad chemical shift ranges (usually large nuclei) embedded in high magnetic fields.

1.2.3.3 Scalar relaxation

The *J*-coupling or indirect spin-spin interaction described in Section 1.1.4 is a potential source of relaxation. Specifically, to some extent, the indirect spin-spin interaction is modulated by molecular motion. This relaxation mechanism is called scalar relaxation.

In most cases, the instantaneous time variation of the spin-spin interaction is so small that its effect on relaxation can be neglected, especially when compared to the much more significant dipolar relaxation. Thus, scalar relaxation is only important in very specific cases, such as small organic molecules with one or more strongly hindered rotational degrees of freedom. More detailed descriptions of scalar relaxation can be found in the following references and in references therein.[34–37]

1.2.3.4 Electric quadrupolar relaxation

The strong interaction between the electric quadrupole moment of nuclei with spin $I > 1/2$ and the surrounding electric field gradient constitutes a powerful mechanism for relaxation. The interaction described by the quadrupolar Hamiltonian, defined in Equation (1.21), depends on the electric field gradient tensor. This interaction is anisotropic and orientation-dependent, and, similar to the interactions described previously, it becomes time-dependent due to molecular motion. This mechanism is called electric quadrupolar relaxation, and it is the dominating relaxation mechanism for quadrupolar nuclei, except for highly symmetric sites.[38] Spin-1/2 nuclei do not relax

via electric quadrupolar relaxation because they have a symmetric charge distribution and, thus, they do not interact with the surrounding electric field gradient.

1.2.3.5 Paramagnetic relaxation

The hyperfine coupling between nuclear spins and unpaired electrons constitutes an additional relaxation mechanism both in solution and in the solid state. This is called paramagnetic relaxation. Due to their high gyromagnetic ratio, electrons have very high magnetic moments that make them extremely efficient at promoting the relaxation of nearby nuclear spins.

The NMR spectra of paramagnetic compounds usually have large chemical shift ranges and broad peaks owing to the fast relaxation of the nuclear spins. Due to the numerous differences between these NMR spectra and those of typical diamagnetic compounds, the analysis of paramagnetic species is often called paramagnetic NMR.[39]

Similar to dipolar relaxation, paramagnetic relaxation can be both intra-molecular and inter-molecular. Indeed, it is possible to use paramagnetic compounds to enhance the relaxation of nuclei, allowing to perform NMR experiments with short repetition times.[40,41]

1.2.3.6 Spin-rotation relaxation

There is a particular coupling interaction between nuclear spins and the overall magnetic field generated by the rotational motion of a molecule. This coupling connects the nuclear spins to the motional degrees of freedom of a molecule, providing a way to transfer energy from the nuclear spin to the surrounding environment. This constitutes an additional relaxation mechanism called spin-rotation (SR) relaxation.[42] SR relaxation is only detectable for small molecules at high temperatures, usually in the gas state.[43]

1.3 Instrumental aspects of NMR

1.3.1 Fourier Transform and Time Domain NMR

Section 1.1.6 described how the energy provided to nuclear spins via the B_1 field is released as a detectable signal, the free induction decay or FID. As stated previously,

the FID is an oscillating electric voltage, and it is detected in a detection coil, sometimes also called receive coil, surrounding the sample. The FID is effectively a signal as a function of time. In other words, it is a signal in the time domain. This represents a major difference between NMR and many other spectroscopic techniques in which the signal is detected directly in the frequency domain. Moreover, the signal decays over time due to relaxation phenomena, and this can be easily modeled by an exponential decay, as described in Section 1.2.

The oscillations of the FID are directly related to the Larmor frequencies of the observed nuclei as well as the other interactions illustrated in Section 1.1. Specifically, the free induction decay is a superposition of different oscillating functions, each associated with a specific nucleus interacting with its surrounding environment. To separate the different frequencies, the FID is digitized, and Fourier transformed. This transforms the signal from the time domain to the frequency domain. The result is a spectrum with peaks in correspondence with the resonant frequency of each specific nucleus. The interactions described in Section 1.1 generate additional features that complicate the shape of the spectra. For example, *J*-coupling causes the signals to split into two or more peaks due to the different possible spin states of the interacting nuclei.

Since the absolute value of the resonant frequency of each nucleus scales linearly with the strength of the magnetic field, NMR spectra are commonly represented using a relative scale, independent of the magnetic field strength. This scale is called chemical shift, and it is indicated with the Greek letter δ. The chemical shift obtained by quoting the resonant frequency relative to a reference frequency and multiplying the obtained value by 10^6 (the difference in orders of magnitude between the Zeeman and chemical shift interactions):

$$\delta = \frac{\nu - \nu_0}{\nu_0} \times 10^6 \tag{1.28}$$

where ν is the resonant frequency of the nucleus and ν_0 is the reference resonant frequency. In the case of ^{1}H and ^{13}C, the reference frequency is that of the protons and the carbon of the methyl groups in tetramethylsilane, respectively.

Fourier transform allows to perform NMR experiments with pulses that excite all the nuclei simultaneously, as opposed to irradiating the nuclei one at a time with a frequency sweep. This represents an enormous advantage in terms of acquisition time.

There is a particular application of NMR in which the signal is not Fourier transformed, but it is analyzed directly in the time domain. This way, the oscillations associated with the nuclear spins in different environments cannot be separated. In other words, chemical information is lost. However, since relaxation is modulated by molecular mobility (see Section 1.2), this allows to draw information about molecular dynamics and all the processes that modify the mobility of atoms. This technique is called Time Domain NMR (TD-NMR), and it can also be performed with low-field benchtop instruments.[44,45]

1.3.2 Pulsed Field Gradient NMR

It has already been described how the resonant frequency of a nucleus depends on the applied magnetic field, B_0. If an additional space-dependent magnetic field is applied along the z-axis, the resonant frequency of a nucleus will be altered depending on its position. If the space-dependent gradient field is $G(z)$, the resonant frequency will now depend on $B_0 + G(z)$. The application of $G(z)$ effectively allows the encoding of the spatial position of the nuclei.[46] In most of the modern NMR techniques, magnetic field gradients are not applied continuously but for short periods of time: they are effectively pulsed spatial variations of the magnetic field. For this reason, they are commonly called pulsed field gradients (PFG). NMR spectroscopists make use of PFGs to study the translational dynamics of atoms and molecules, such as their diffusion both in bulk and in confined media. Additionally, modern NMR instruments employ PFGs as an alternative to phase cycling to suppress instrumental artifacts and select only the transitions of interest.[47] Last but not least, the use of PFGs is the basis of Magnetic Resonance Imaging (MRI).

PFG NMR can be employed to determine the self-diffusion coefficients of gaseous NMR-active nuclei or molecules in solution. The general approach involves the application of a gradient pulse along the z-axis after the magnetization has been brought onto the xy-plane. This registers the positions of the spins by creating a space-dependent phase shift. The application of a gradient pulse with the opposite sign but the same duration and intensity undoes this encoding, canceling the phase shift and returning the spins to their original position. However, this holds only if the spins remain in the same position during the time between the two gradient pulses, called diffusion time, Δ. If the

spins move during Δ, the reversing of the space-dependent phase shift is not perfect, and the signal is attenuated. The signal loss depends on several parameters: the diffusion time Δ, the gradient pulse intensity, g, and duration, δ, the gyromagnetic ratio of the nucleus, γ, and the diffusion coefficient, D. Assuming free diffusion, the NMR signal decays following a Gaussian behavior described by the generalized Stejskal-Tanner equation

$$I = I_0 \exp(-\gamma^2\delta^2\sigma^2 g^2 \Delta' D) \tag{1.29}$$

where I is the attenuated signal, I_0 is the reference signal, while σ and Δ' are the gradient shape factor and the corrected diffusion time, respectively. These parameters depend on the shape of the pulsed gradients and the applied pulse sequence. Detailed derivation of these parameters for different pulse sequences can be found in the literature.[48,49] Measuring a series of intensities with variable gradient pulse duration, intensity, or diffusion time, and fitting the data to Equation (1.29) returns the NMR self-diffusion coefficient. To avoid relaxation effects caused by the increase in the durations, normally these experiments are performed by varying the gradient pulse intensity while keeping constant their duration as well as the diffusion time.

Diffusion NMR experiments can also be employed to determine the constituents of a mixture depending on their different diffusion coefficients. This can be done by plotting a 2D map with the chemical shift in one dimension and the diffusion coefficient in the other. The map is obtained by a numerical inversion process that involves the estimation of the solutions to a Fredholm Integral Equation of the first kind. More details on this can be found in the literature.[50,51] This type of processing has been called Diffusion Ordered SpectroscopY (DOSY) since it was first reported in 1992.[52] However, DOSY is only the name of one of the possible processing methods, and it should not be confused with the general diffusion NMR experiment.

The most common and basic pulse sequences employed in PFG NMR are illustrated in Figure 1.6. The first one is based on the Hahn echo or spin echo (SE) pulse sequence described in Section 1.2.2. The second one is based on the so-called stimulated echo (STE).[53] In a STE, the refocusing is attained by two $\pi/2$ pulses instead of a single π pulse. The main difference between the two techniques lies in the magnetization during the diffusion time. In the SE sequence, the magnetization is

transversal during Δ, while in the STE the magnetization is stored longitudinally after the second $\pi/2$ pulse. This means that the diffusion times are limited by T_2 and T_1 in the SE and STE pulse sequences, respectively. Thus, the STE pulse sequence is more suitable when longer diffusion times are needed or when the nuclear spins of interest have low T_2.

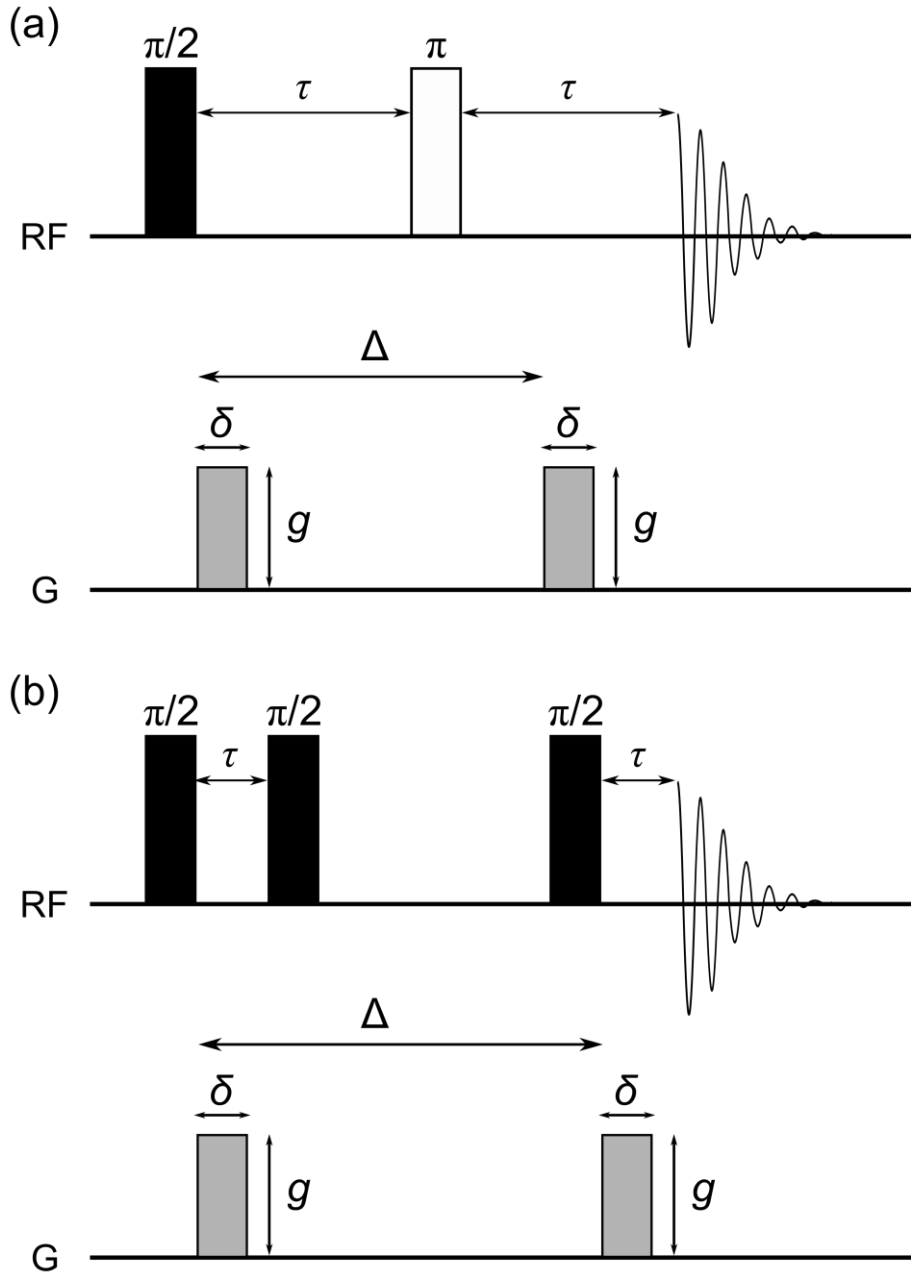

Figure 1.6. The two most common basic sequences used in pulsed field gradient (PFG) nuclear magnetic resonance: (a) pulsed field gradient spin echo (SE), (b) pulsed field gradient stimulated echo (STE). The parameters Δ, δ, and g are defined in the main text, while τ is a representative delay time.

1.4 ^{129}Xe NMR Spectroscopy

The previous sections gave a brief theoretical introduction to the phenomenon of nuclear magnetic resonance, relaxation, and some NMR techniques and pulse sequences. This section will focus on a particular application of NMR which is the main technique of this work: ^{129}Xe NMR spectroscopy.

1.4.1 Basic principles

In its elemental form and under standard conditions, the noble gas xenon (Xe) is colorless, odorless, and denser than air. It is almost completely inert since it can only form compounds under harsh conditions such as high temperatures and high pressures coupled with the presence of specific catalysts. Owing to its chemical inertness and its lipophilic character, some authors view xenon as an "ennobled" alkane.[54] However, despite its limited dimensions compared to molecular species, it has a large electron cloud of 54 electrons. This makes xenon a highly polarizable atom with a high sensitivity to the surrounding environment. Natural xenon has nine different stable isotopes, even though ^{124}Xe and ^{126}Xe contribute minimally to its overall natural abundance. From an NMR point of view, two of these isotopes have interesting properties. The first one is ^{131}Xe, which is one of the most abundant isotopes with a natural abundance of around 21.2%. This is a quadrupolar nucleus with 3/2 nuclear spin. The other one is ^{129}Xe, the second most abundant isotope (26.4% natural abundance) and a spin 1/2 nucleus. These properties make ^{129}Xe the most suitable xenon isotope for NMR spectroscopy.

Xenon can be detected with NMR in its very few stable compounds for structural elucidation. However, most importantly ^{129}Xe can also be employed for gas phase NMR spectroscopy. ^{129}Xe is an exceptional NMR probe for non-destructive and highly sensitive morphological and structural characterization of solid and liquid state materials. The chemical shift of gaseous ^{129}Xe is determined by the physical interactions with the surrounding environment, using unconfined free xenon gas as a chemical shift reference. The interaction of xenon with the surrounding environment alters its highly polarizable electron cloud, and any change is reflected in its chemical shift that covers a broad range of almost 7000 ppm.

The first experimental works on ^{129}Xe NMR were published by Ito and Fraissard in the 1980s.[55,56] They discovered that the chemical shift of xenon adsorbed in different types of zeolites is determined by the xenon pressure, the presence of cations, and, most importantly, the size of the cavities. In the 1990s, Jameson and co-workers published a series of theoretical papers on the chemical shift of xenon in zeolites and its dependence on temperature and gas pressure.[57–61] Since these pioneering works, ^{129}Xe NMR spectroscopy has become a powerful tool to study the morphology of many different porous systems including but not limited to mesoporous silica,[62–66] clays,[67] porous organic materials,[68–70] polymers,[71–76] carbonaceous materials,[77–82] and metal-organic frameworks.[83–86] This led to the development of several models that correlate the xenon chemical shift to the pore size and, in some cases, to the thermodynamic parameters of xenon adsorption (see Section 1.4.3.2). However, these models are mostly empirical or semi-empirical and their applicability is limited to very specific classes of materials. In addition to that, xenon NMR has been used to study not only pore size distributions but also pore connectivity, pore blocking, and pore hierarchy.

However, ^{129}Xe NMR is not limited to solid-state materials. Williamson and Jokisaari studied the NMR properties of xenon gas dissolved in a variety of simple isotropic liquids.[87–89] The basic principle is the same as the NMR of xenon inside solid materials: when xenon is dissolved in a liquid, its surrounding environment alters the chemical shift compared to the reference free gas. These works paved the way for the modern studies on the nanostructural organization of simple liquids and liquid mixtures,[90–93] and complex nanosegregated ionic liquids.[94–99]

1.4.2 ^{129}Xe chemical shift

1.4.2.1 Porous materials

The chemical shift of xenon adsorbed in a porous material is commonly expressed as a sum of different contributions.[11]

$$\delta = \delta_0 + \delta_{\text{Xe-Xe}}(\rho_{\text{Xe}}) + \delta_{\text{S}} + \delta_{\text{SAS}} + \delta_{\text{E}} + \delta_{\text{M}} \tag{1.30}$$

δ_0 is the chemical shift of gaseous xenon at zero pressure which is commonly used as a reference and set to 0 ppm. This value can be determined by measuring the

chemical shift of gaseous xenon at different pressures and extrapolating to zero. As shown by Jameson et al., the temperature dependence of δ_0 is negligible in the standard operating range of ^{129}Xe NMR.[100]

The second term represents the contribution of the xenon-xenon interactions, and it depends on the xenon gas density, ρ_{Xe}. Since xenon has a van der Waals radius of around 0.22 nm, this term is particularly important in microporous materials (pore dimensions < 2 nm), while it can be neglected in mesoporous materials (pore dimensions between 2 nm and 50 nm), unless experiments are performed at high xenon pressures.

δ_S is the chemical shift resulting from the interaction of xenon atoms with the surface. In the simplest case, xenon atoms close to the surface are rapidly exchanging between the adsorbed and the free state. δ_S can be expressed as an average of the adsorbed and free xenon chemical shifts weighted by the respective molar fractions.

$$\delta_S = x_{ads}\delta_{ads} + x_{free}\delta_{free} \tag{1.30}$$

where δ_{ads} and δ_{free} are the chemical shifts of adsorbed and free xenon, and x_{ads} and x_{free} are the respective molar fractions. Since δ_S is determined by the dynamics of xenon gas, it is strongly temperature dependent. The mobility of xenon atoms is increased with increasing temperature and, in turn, their residence time on the surface is reduced. Thus, x_{ads} decreases with temperature and, since $\delta_{ads} > \delta_{free}$ (δ_{free} is 0 ppm at low xenon pressure), δ_S also decreases with temperature. δ_S is the main term of interest in the analysis of porous materials and free volume. Many of the developed models that relate the free volume with the xenon chemical shift focus on δ_S (see Section 1.4.3).

δ_{SAS} is related to the interaction of xenon with strong adsorption sites (SAS) such as highly charged cations. This interaction can be recognized by analyzing the pressure dependence of the xenon chemical shift. In the absence of SAS, the xenon chemical shift decreases with decreasing xenon pressure. However, in the presence of SAS, the xenon chemical shift shows a steep hyperbolic increase at very low xenon pressures.[101] This is because most of the xenon atoms interact with strong adsorption sites which have a large contribution to the chemical shift.

δ_E and δ_M are contributions given by the presence of electric fields and paramagnetic species. These large contributions are important even if xenon is not directly adsorbed onto the respective sites.

At low xenon gas pressures, the xenon-xenon interaction term in Equation (1.30) becomes negligible. The terms δ_{SAS}, δ_E, and δ_M can also be omitted in the absence of strong adsorption sites, electric fields, and paramagnetic species, respectively. Under these assumptions, Equation (1.30) is greatly simplified. This allows to easily determine the xenon-surface interaction term, δ_S.

1.4.2.2 Liquids and mixtures

Similar to the case of porous materials, the chemical shift of xenon dissolved in a liquid can be expressed as the sum of different terms.[7,90]

$$\delta = \delta_0 + \delta_b + \delta_m \tag{1.31}$$

δ_0 is the same chemical shift reference as that in Equation (1.30). δ_b is a contribution derived from the magnetic susceptibility of the solvent. This is due to secondary magnetic fields generated by the motion of electrons in the sample. This term can be calculated with the following equation where χ_v is the volume susceptibility of the solvent.

$$\delta_b = \frac{4\pi}{3}\chi_v \tag{1.32}$$

The term δ_m is called medium shift, and it depends only on xenon-solvent interactions. δ_m can also be expressed as a sum of different contributions:

$$\delta_m = \delta_a + \delta_w + \delta_{e2} \tag{1.33}$$

δ_a is induced by the magnetic anisotropy of the solvent, while δ_{e2} is due to the interaction between the permanent dipole of the solvent and the induced dipole in the xenon atoms. The remaining term, δ_w, has this designation because historically it has been thought that the chemical shift of xenon was dependent on the xenon-solvent van der Waals dispersive forces. However, several papers demonstrated that the chemical shift is determined by a repulsive interaction between the electronic clouds of xenon and

the solvent molecule, commonly referred to as steric hindrance.[93,102–104] This interaction is related to the repulsive part of the intermolecular Lennard-Jones potential, as opposed to the attractive van der Waals forces that are related to the attractive part.

1.4.3 Proposed chemical shift models for porous materials

1.4.3.1 Zeolites

The first model that relates the xenon chemical shift to the pore size was proposed by Demarquay and Fraissard for zeolites.[105] From combined computational and experimental studies on ferrierite and A, L, Y, and Z-type zeolites they determined a relationship between δ_S and the mean free path of xenon, Γ, in the absence of paramagnetic species and strong adsorption sites.

$$\delta_S = \delta_{ads}\left(\frac{a}{a+\Gamma}\right) \tag{1.34}$$

where δ_{ads} is the chemical shift of xenon adsorbed on the pore walls and a is a coefficient that depends on the material. These parameters were determined by fitting a series of experimental chemical shifts to Equation (1.34), obtaining δ_{ads} = 243 ppm and a = 2.054 Å:

$$\delta_S = 243\left(\frac{2.054}{2.054+\Gamma}\right) \tag{1.35}$$

The mean free path can be used to calculate the pore diameter in the special cases of cylindrical (D_c) and spherical (D_s) pores:

$$D_c = \Gamma + D_{Xe} \tag{1.36}$$

$$D_s = 2\Gamma + D_{Xe} \tag{1.37}$$

where D_{Xe} = 4.4 Å is the van der Waals diameter of xenon. The shape of the pores can be determined by analyzing the pressure dependence of the chemical shift. In spherical pores, the Xe-Xe collisions have an isotropic distribution, and the chemical shift increases linearly with pressure. In anisotropic cylindrical pores, the chemical shift-pressure dependence is nonlinear, with a concavity at chemical shift values.

1.4.3.2 Mesoporous silica

In the 1990s, Terskikh and co-workers started applying ^{129}Xe NMR on different mesoporous silicas. They obtained very similar ^{129}Xe chemical shift values to those reported by Fraissard et al. for microporous zeolites, i.e. around 100 ppm. However, nitrogen sorption and mercury porosimetry ruled out the presence of micropores and returned an average pore size in the range of 20-400 Å. To explain these unexpected results, the authors proposed an alternative model that relates the xenon chemical shift to the morphological parameters of mesoporous silica, assuming that there are no strong adsorption sites and paramagnetic ions.[62]

The basic assumption is that mesopores are big enough that xenon atoms in the center of the pore behave as free xenon gas. The chemical shift is then determined by a dynamic equilibrium between free and adsorbed xenon. Assuming that the ideal gas law is valid for xenon inside the pores and that the adsorption of xenon follows Henry's law, the chemical shift is given by

$$\delta = \frac{\delta_S}{1 + \frac{V_g}{KSRT}} \tag{1.38}$$

R is the gas constant, T is the temperature, K is Henry's constant, and V_g/S is the volume-to-surface ratio of the mesopores. This equation correlates the xenon chemical shift to the volume-to-surface ratio, provided that the Henry's constant is known. The parameters of the porous structure can also be expressed with the mean pore size, D, given by

$$D = \frac{\eta V_g}{S} \tag{1.39}$$

where η is a shape factor that depends on pore geometry. Assuming that the pores are non-intersecting, $\eta = 4$ for cylindrical pores, $\eta = 2.8$ for spherical pores, and $\eta = 2$ for slit-like pores. In the case of intersecting pores, η takes lower values. Equation (1.38) expressed in terms of the mean pore size becomes

$$\delta = \frac{\delta_S}{1 + \frac{D}{K\eta RT}} \tag{1.40}$$

Since K depends on temperature, Equations (1.38) and (1.40) are only applicable in isothermal conditions. The temperature dependence of K is given by the following equation.

$$\mathrm{K} = \frac{K_0}{\sqrt{T}} \exp\left(\frac{\Delta_{\mathrm{ads}}H}{RT}\right) \tag{1.41}$$

where K_0 is a temperature-independent pre-exponential factor, and $\Delta_{\mathrm{ads}}H$ is the enthalpy of xenon adsorption. Inserting Equation (1.41) into Equation (1.38) gives

$$\delta = \frac{\delta_{\mathrm{S}}}{1 + \frac{V_{\mathrm{g}}}{K_0 SR\sqrt{T}} \exp\left(-\frac{\Delta_{\mathrm{ads}}H}{RT}\right)} \tag{1.42}$$

Equation (1.42) describes the dependence of the xenon chemical shift on the morphological parameters of mesoporous silica and the thermodynamics of xenon adsorption. Fitting variable temperature xenon chemical shifts to this equation gives the enthalpy of adsorption of xenon on silica. Even though this model was generally proposed for mesoporous silica, it has been applied successfully to a wide variety of porous materials.[68,69,106–109]

1.4.3.3 Porous carbon materials

The porous structures of carbon-based materials are generally heterogeneous and disordered. Moreover, these materials generally contain paramagnetic impurities. For these reasons, obtaining quantitative information about the pore size from xenon chemical shifts is difficult. Fraissard et al. proposed an empirical model for a series of activated microporous carbons with different sizes.[110] They observed that the xenon-xenon interaction term, $\delta_{\mathrm{Xe\text{-}Xe}}$, expressed in ppm cm^3 mmol^{-1} (converting from ppm amagat^{-1}, 1 amagat = 0.045 cm^3 mmol^{-1}), is linearly correlated with the mean pore size, D:

$$\delta_{\mathrm{Xe\text{-}Xe}} = \eta + \kappa D \tag{1.43}$$

with η = 5.1 ppm cm^3 mmol^{-1} and κ = 7 ppm cm^3 mmol^{-1} nm^{-1}.

The term of interest here is $\delta_{Xe\text{-}Xe}$. Indeed, the authors observed no correlation between δ_S and the size of the pores.

In a later work, the authors followed a similar approach for a series of mesoporous carbons.[111] Under the assumption that all the xenon atoms are located on the surface of the materials, they observed that the xenon chemical shift obeyed the following relationship

$$\delta(\gamma) = \delta_S + \delta_{Xe\text{-}Xe}^{Surf.}\gamma \tag{1.44}$$

where γ is the surface density, and the second term, derived from the slope of $\delta(\gamma)$, is the contribution to the chemical shift given by the binary xenon-xenon collisions only on the surface of the material. The authors found that this term monotonically decreases with increasing the mean pore size, following the relationship

$$\delta_{Xe\text{-}Xe}^{Surf.} = \frac{\vartheta}{1 + \xi D} \tag{1.45}$$

with $\vartheta = 70$ ppm m^2 μmol^{-1} and $\xi = 0.5$ nm^{-1}.

1.5 Conclusions

This chapter started with an introduction to the phenomenon of nuclear magnetic resonance. A brief description of the quantum mechanical interactions involved in nuclear magnetic resonance was provided along with simple forms of the corresponding Hamiltonians. Section 1.2 gave an overview of relaxation phenomena and associated mechanisms, with some methods to measure the NMR relaxation times. This introduction on NMR is not meant to be exhaustive by any means: it is just an overview of how the different interactions can affect the NMR properties such as chemical shift and relaxation. Formal and complete descriptions of the phenomena involved in NMR can be found in many papers and textbooks such as those referenced throughout the chapter.

Section 1.3 gave a brief description of some instrumental aspects of NMR, such as the use of Fourier transform, time-domain NMR, and pulsed-field gradient NMR. Lastly, Section 1.4 introduced ^{129}Xe NMR spectroscopy, with a description of the basic

principles, the factors affecting the ^{129}Xe chemical shift, and the proposed models that relate the xenon NMR parameters to the morphological features of different classes of materials.

1.6 Bibliography

[1] A. E. Derome, *Modern NMR Techniques for Chemistry Research*, Pergamon Pr, **1987**.

[2] J. Keeler, *Understanding NMR Spectroscopy*, Wiley, **2006**.

[3] M. H. Levitt, *Spin Dynamics: Basics of Nuclear Magnetic Resonance*, Wiley, **2008**.

[4] H. Günther, *NMR Spectroscopy: Basic Principles, Concepts and Applications in Chemistry*, Wiley, **2013**.

[5] G. A. Webb, Ed. , *Modern Magnetic Resonance*, Springer, **2018**.

[6] P. J. Barrie, J. Klinowski, *Prog. Nucl. Magn. Reson. Spectrosc.* **1992**, *24*, 91–108.

[7] J. Jokisaari, *Prog. Nucl. Magn. Reson. Spectrosc.* **1994**, *26*, 1–26.

[8] D. Raftery, in *Annu. Reports NMR Spectrosc.*, **2006**, pp. 205–270.

[9] E. Weiland, M. A. Springuel-Huet, A. Nossov, A. Gédéon, *Microporous Mesoporous Mater.* **2016**, *225*, 41–65.

[10] D. Wisser, M. Hartmann, *Adv. Mater. Interfaces* **2020**, *8*, DOI 10.1002/admi.202001266.

[11] M. Boventi, M. Mauri, R. Simonutti, *Appl. Sci.* **2022**, *12*, 3152.

[12] S. A. Smith, W. E. Palke, J. T. Gerig, *Concepts Magn. Reson.* **1992**, *4*, 107–144.

[13] S. A. Smith, W. E. Palke, J. T. Gerig, *Concepts Magn. Reson.* **1992**, *4*, 181–204.

[14] S. A. Smith, W. E. Palke, J. T. Gerig, *Concepts Magn. Reson.* **1993**, *5*, 151–177.

[15] T. Vosegaard, *Prog. Nucl. Magn. Reson. Spectrosc.* **2021**, *123*, 51–72.

[16] A. Drechsler, F. Separovic, *IUBMB Life* **2003**, *55*, 515–523.

[17] W. T. Franks, B. J. Wylie, H. L. F. Schmidt, A. J. Nieuwkoop, R. M. Mayrhofer, G. J. Shah, D. T. Graesser, C. M. Rienstra, *Proc. Natl. Acad. Sci. U. S. A.* **2008**, *105*, 4621–4626.

[18] P. Schanda, M. Huber, J. Boisbouvier, B. H. Meier, M. Ernst, *Angew. Chemie* -

Int. Ed. **2011**, *50*, 11005–11009.

[19] J. Lounila, J. Jokisaari, *Prog. Nucl. Magn. Reson. Spectrosc.* **1982**, *15*, 249–290.

[20] J. Vaara, J. Jokisaari, R. E. Wasylishen, D. L. Bryce, *Prog. Nucl. Magn. Reson. Spectrosc.* **2002**, *41*, 233–304.

[21] J. Jokisaari, J. Vaara, *Phys. Chem. Chem. Phys.* **2013**, *15*, 11427–11430.

[22] R. E. Wasylishen, S. E. Ashbrook, S. Wimperis, *NMR of Quadrupolar Nuclei in Solid Materials*, Wiley, **2012**.

[23] S. E. Ashbrook, *Phys. Chem. Chem. Phys.* **2009**, *11*, 6892–6905.

[24] T. Bräuniger, M. Jansen, *Zeitschrift fur Anorg. und Allg. Chemie* **2013**, *639*, 857–879.

[25] K. Chen, *Int. J. Mol. Sci.* **2020**, *21*, 1–22.

[26] A. D. Bain, *J. Magn. Reson.* **1984**, *56*, 418–427.

[27] G. Bodenhausen, H. Kogler, R. R. Ernst, *J. Magn. Reson.* **1984**, *58*, 370–388.

[28] O. W. Sørensen, G. W. Eich, M. H. Levitt, G. Bodenhausen, R. R. Ernst, *Prog. Nucl. Magn. Reson. Spectrosc.* **1984**, *16*, 163–192.

[29] J. Shriver, *Concepts Magn. Reson.* **1992**, *4*, 1–33.

[30] Y. Zhang, F. Han, A. Jerschow, *eMagRes* **2013**, *2*, 229–235.

[31] F. Bloch, *Phys. Rev.* **1946**, *70*, 460–474.

[32] E. L. Hahn, *Phys. Rev.* **1950**, *80*, 580–594.

[33] S. Meiboom, D. Gill, *Rev. Sci. Instrum.* **1958**, *29*, 688–691.

[34] S. Sýkora, *Stan's Libr.* **2009**, *III*, DOI 10.3247/SL3Nmr09.004.

[35] I. Kuprov, D. M. Hodgson, J. Kloesges, C. I. Pearson, B. Odell, T. D. W. Claridge, *Angew. Chemie* **2015**, *127*, 3768–3772.

[36] T. D. Panduwawala, L. Josa-Culleré, I. Kuprov, B. Odell, M. G. Moloney, T. D. W. Claridge, *J. Org. Chem.* **2016**, *81*, 4142–4148.

[37] S. J. Elliott, C. Bengs, L. J. Brown, J. T. Hill-Cousins, D. J. O'Leary, G. Pileio, M. H. Levitt, *J. Chem. Phys.* **2019**, *150*, DOI 10.1063/1.5074199.

[38] I. P. Gerothanassis, C. G. Tsanaktsidis, *Concepts Magn. Reson.* **1996**, *8*, 63–74.

[39] A. J. Pell, G. Pintacuda, C. P. Grey, *Prog. Nucl. Magn. Reson. Spectrosc.* **2019**, *111*, 1–271.

[40] R. Sharp, L. Lohr, J. Miller, *Prog. Nucl. Magn. Reson. Spectrosc.* **2001**, *38*, 115–158.

[41] S. Cai, C. Seu, Z. Kovacs, A. D. Sherry, Y. Chen, *J. Am. Chem. Soc.* **2006**, *128*, 13474–13478.

[42] R. E. D. McClung, *eMagRes* **2007**, *2007*, 1–5.

[43] P. M. Singer, D. Asthagiri, W. G. Chapman, G. J. Hirasaki, *J. Chem. Phys.* **2018**, *148*, DOI 10.1063/1.5027097.

[44] D. Besghini, M. Mauri, R. Simonutti, *Appl. Sci.* **2019**, *9*, 1801.

[45] V. Litvinov, Y. Men, *Polymer (Guildf).* **2022**, *256*, 125205.

[46] G. Pagès, V. Gilard, R. Martino, M. Malet-Martino, *Analyst* **2017**, *142*, 3771–3796.

[47] J. -M Zhu, I. C. P. Smith, *Concepts Magn. Reson.* **1995**, *7*, 281–291.

[48] D. Sinnaeve, *Concepts Magn. Reson. Part A Bridg. Educ. Res.* **2012**, *40 A*, 39–65.

[49] P. W. Kuchel, G. Pagès, K. Nagashima, S. Velan, V. Vijayaragavan, V. Nagarajan, K. H. Chuang, *Concepts Magn. Reson. Part A* **2012**, *40A*, 205–214.

[50] M. Nilsson, *J. Magn. Reson.* **2009**, *200*, 296–302.

[51] E. J. Fordham, L. Venkataramanan, J. Mitchell, A. Valori, *Diffus. Fundam.* **2017**, *29*, 1–8.

[52] K. F. Morris, C. S. Johnson Jr., *J. Am. Chem. Soc.* **1992**, *114*, 3139–3141.

[53] J. Frahm, K. D. Merboldt, W. Hänicke, A. Haase, *J. Magn. Reson.* **1985**, *64*, 81–93.

[54] E. J. M. Filipe, L. M. B. Dias, J. C. G. Calado, C. McCabe, G. Jackson, *Phys. Chem. Chem. Phys.* **2002**, *4*, 1618–1621.

[55] T. Ito, J. Fraissard, in *Fifth Int. Conf. Zeolites*, **1980**, pp. 510–515.

[56] T. Ito, J. Fraissard, *J. Chem. Phys.* **1982**, *76*, 5225–5229.

[57] C. J. Jameson, A. C. De Dios, *J. Chem. Phys.* **1992**, *97*, 417–434.

[58] C. J. Jameson, A. K. Jameson, H. M. Lim, B. I. Baello, *J. Chem. Phys.* **1994**, *100*, 5977–5987.

[59] C. J. Jameson, A. K. Jameson, H. M. Lim, B. I. Baello, *J. Chem. Phys.* **1994**, *100*, 5965–5976.

[60] C. J. Jameson, H. M. Lim, *J. Chem. Phys.* **1995**, *103*, 3885–3894.

[61] C. J. Jameson, A. K. Jameson, R. E. Gerald, H. M. Lim, *J. Phys. Chem. B* **1997**, *101*, 8418–8437.

[62] V. V. Terskikh, I. L. Mudrakovskii, V. M. Mastikhin, *J. Chem. Soc. Faraday Trans.* **1993**, *89*, 4239–4243.

[63] I. L. Moudrakovski, V. V. Terskikh, C. I. Ratcliffe, J. A. Ripmeester, L. Q. Wang, Y. Shin, G. J. Exarhos, *J. Phys. Chem. B* **2002**, *106*, 5938–5946.

[64] S. J. Huang, S. Huh, P. S. Lo, S. H. Liu, V. S. Y. Lin, S. Bin Liu, *Phys. Chem. Chem. Phys.* **2005**, *7*, 3080–3087.

[65] N. Mnasri, C. Charnay, L. C. De Ménorval, Y. Moussaoui, E. Elaloui, J. Zajac, *Microporous Mesoporous Mater.* **2014**, *196*, 305–313.

[66] D. Schneider, A. G. Attallah, S. Wassersleben, M. Wenzel, J. Matysik, R. Krause-Rehberg, D. Enke, *Microporous Mesoporous Mater.* **2020**, *307*, 110515.

[67] C. D. Keenan, M. M. Herling, R. Siegel, N. Petzold, C. R. Bowers, E. A. Rössler, J. Breu, J. Senker, *Langmuir* **2013**, *29*, 643–652.

[68] I. L. Moudrakovski, L. Q. Wang, T. Baumann, J. H. Satcher, G. J. Exarhos, C. I. Ratcliffe, J. A. Ripmeester, *J. Am. Chem. Soc.* **2004**, *126*, 5052–5053.

[69] I. L. Moudrakovski, C. I. Ratcliffe, J. A. Ripmeester, L. Q. Wang, G. J. Exarhos, T. F. Baumann, J. H. Satcher, *J. Phys. Chem. B* **2005**, *109*, 11215–11222.

[70] R. Anedda, D. V. Soldatov, I. L. Moudrakovski, M. Casu, J. A. Ripmeester, *Chem. Mater.* **2008**, *20*, 2908–2920.

[71] T. R. Stengle, K. L. Williamson, *Macromolecules* **1987**, *20*, 1428–1430.

[72] T. T. P. Cheung, P. J. Chu, *J. Phys. Chem.* **1992**, *96*, 9551–9554.

[73] J. H. Walton, J. B. Miller, C. M. Roland, *J. Polym. Sci. Part B Polym. Phys.* **1992**, *30*, 527–532.

[74] R. Simonutti, S. Bracco, A. Comotti, M. Mauri, P. Sozzani, *Chem. Mater.* **2006**, *18*, 4651–4657.

[75] J. Weber, J. Schmidt, A. Thomas, W. Böhlmann, *Langmuir* **2010**, *26*, 15650–15656.

[76] H. Yoshimizu, S. Ohta, T. Asano, T. Suzuki, Y. Tsujita, *Polym. J.* **2012**, *44*, 821–826.

[77] C. F. M. Clewett, T. Pietraß, *J. Phys. Chem. B* **2005**, *109*, 17907–17912.

[78] K. V. Romanenko, A. Fonseca, S. Dumonteil, J. B. Nagy, J. B. D'Espinose De Lacaillerie, O. B. Lapina, J. Fraissard, *Solid State Nucl. Magn. Reson.* **2005**, *28*, 135–141.

[79] Y. J. Lee, K. D. Park, S. J. Huang, S. Bin Liu, H. J. Lee, *J. Nanosci. Nanotechnol.* **2007**, *7*, 3932–3937.

[80] K. V. Romanenko, O. B. Lapina, X. Py, J. Fraissard, *Russ. J. Gen. Chem.* **2008**, *78*, 2171–2181.

[81] T. Onfroy, F. Guenneau, M. A. Springuel-Huet, A. Gédéon, *Carbon N. Y.* **2009**, *47*, 2352–2357.

[82] M. Oschatz, H. C. Hoffmann, J. Pallmann, J. Schaber, L. Borchardt, W. Nickel, I. Senkovska, S. Rico-Francés, J. Silvestre-Albero, S. Kaskel, E. Brunner, *Chem. Mater.* **2014**, *26*, 3280–3288.

[83] M. A. Springuel-Huet, A. Nossov, Z. Adem, F. Guenneau, C. Volkringer, T. Loiseau, G. Férey, A. Gédéon, *J. Am. Chem. Soc.* **2010**, *132*, 11599–11607.

[84] H. C. Hoffmann, B. Assfour, F. Epperlein, N. Klein, S. Paasch, I. Senkovska, S. Kaskel, G. Seifert, E. Brunner, *J. Am. Chem. Soc.* **2011**, *133*, 8681–8690.

[85] Y. X. Ma, Z. J. Li, L. Wei, S. Y. Ding, Y. B. Zhang, W. Wang, *J. Am. Chem. Soc.* **2017**, *139*, 4995–4998.

[86] R. Giovine, C. Volkringer, M. A. Springuel-Huet, A. Nossov, F. Blanc, J. Trébosc, T. Loiseau, J. P. Amoureux, O. Lafon, F. Pourpoint, *J. Phys. Chem. C* **2017**, *121*, 19262–19268.

[87] K. W. Miller, N. V. Reo, A. J. M. Schoot Uiterkamp, D. P. Stengle, T. R. Stengle, K. L. Williamson, *Proc. Natl. Acad. Sci. U. S. A.* **1981**, *78*, 4946–4949.

[88] P. Diehl, J. Jokisaari, *J. Magn. Reson.* **1990**, *88*, 660–665.

[89] K. Oikarinen, J. Jokisaari, *Appl. Magn. Reson.* **1995**, *8*, 587–595.

[90] P. Morgado, R. Bonifacio, F. G. Martins, E. J. M. Filipe, *J. Phys. Chem. B* **2013**, *117*, 9014–9024.

[91] P. Peuravaara, J. Karjalainen, J. Zhu, J. Mareš, P. Lantto, J. Vaara, *Sci. Rep.* **2018**, *8*, 1–11.

[92] P. Morgado, J. Barras, E. J. M. Filipe, *Phys. Chem. Chem. Phys.* **2020**, *22*, 14736–14747.

[93] M. Boventi, V. Mazzilli, R. Simonutti, F. Castiglione, G. Saielli, *J. Mol. Liq.* **2023**, *382*, 122011.

[94] F. Castiglione, R. Simonutti, M. Mauri, A. Mele, *J. Phys. Chem. Lett.* **2013**, *4*, 1608–1612.

[95] P. Morgado, K. Shimizu, J. M. S. S. Esperanc, M. Reis, P. N. Rebelo, J. N. C. Lopes, E. J. M. Filipe, *J. Phys. Chem. Lett.* **2013**, *4*, 2758–2762.

[96] G. Saielli, A. Bagno, F. Castiglione, R. Simonutti, M. Mauri, A. Mele, *J. Phys. Chem. B* **2014**, *118*, 13963–13968.

[97] N. J. Brooks, F. Castiglione, C. M. Doherty, A. Dolan, A. J. Hill, P. A. Hunt, R. P. Matthews, M. Mauri, A. Mele, R. Simonutti, I. J. Villar-Garcia, C. C. Weber, T. Welton, *Chem. Sci.* **2017**, *8*, 6359–6374.

[98] F. Castiglione, G. Saielli, M. Mauri, R. Simonutti, A. Mele, *J. Phys. Chem. B* **2020**, *124*, 6617–6627.

[99] G. Saielli, F. Castiglione, M. Mauri, R. Simonutti, A. Mele, *ChemPhysChem* **2021**, *22*, 1880–1890.

[100] C. J. Jameson, A. K. Jameson, S. M. Cohen, *J. Chem. Phys.* **1973**, *59*, 4540–4546.

[101] T. Ito, J. Fraissard, *J. Chem. Soc. Faraday Trans. 1 Phys. Chem. Condens. Phases* **1987**, *83*, 451–462.

[102] C. J. Jameson, D. N. Sears, A. C. De Dios, *J. Chem. Phys.* **2003**, *118*, 2575–2580.

[103] C. J. Jameson, D. N. Sears, S. Murad, *J. Chem. Phys.* **2004**, *121*, 9581–9592.

[104] M. Hanni, P. Lantto, J. Vaara, *Phys. Chem. Chem. Phys.* **2009**, *11*, 2485–2496.

[105] J. Demarquay, J. Fraissard, *Chem. Phys. Lett.* **1987**, *136*, 314–318.

[106] L. Q. Wang, D. Wang, J. Liu, G. J. Exarhos, S. Pawsey, I. Moudrakovski, *J. Phys. Chem. C* **2009**, *113*, 6577–6583.

[107] S. Pawsey, K. K. Kalebaila, I. Moudrakovski, J. A. Ripmeester, S. L. Brock, *J. Phys. Chem. C* **2010**, *114*, 13187–13195.

[108] L. Q. Wang, D. Wang, J. Liu, G. J. Exarhos, *J. Phys. Chem. C* **2012**, *116*, 22–29.

[109] Y. Mao, N. K. Karan, M. Song, R. Hopson, P. R. Guduru, L. Q. Wang, *Energy and Fuels* **2017**, *31*, 5622–5628.

[110] K. V. Romanenko, X. Py, J. B. D. E. De Lacaillerie, O. B. Lapina, J. Fraissard, *J. Phys. Chem. B* **2006**, *110*, 3055–3060.

[111] K. V. Romanenko, J. B. d. E. de Lacaillerie, O. Lapina, J. Fraissard, *Microporous Mesoporous Mater.* **2007**, *105*, 118–123.

2. Probing the structure of halomethanes with xenon

Parts of this Chapter have been published in

M. Boventi, V. Mazzilli, R. Simonutti, F. Castiglione, G. Saielli, *J. Mol. Liq.* **2023**, *382*, 122011.

The computational calculations were performed by Valerio Mazzilli, PhD student under the supervision of Dr. Giacomo Saielli from the CNR Institute on Membrane Technology, Padova Unit.

2.1 Introduction

According to some authors, xenon can be considered as an "ennobled" alkane thanks to its chemical inertness and its lipophilicity.[1] However, despite its general lipophilic character, xenon has a significant solubility not only in apolar solvents but also in polar media such as water and blood.[2–4] These features coupled with the high sensitivity to the surrounding environment have led to the use of xenon as a non-invasive NMR probe not only in the gaseous phase but also in solution. Dissolved xenon atoms can be viewed as surrounded by dynamic cages of solvent molecules that influence the NMR parameters such as chemical shift and spin-lattice relaxation time, providing a way to study the molecular organization of liquids. Indeed, this technique has been applied to a wide variety of liquids,[5–8] mixtures,[9–11] and supramolecular complexes.[12,13]

The reported chemical shifts of xenon dissolved in simple isotropic liquids and binary mixtures cover a very wide range from 85 ppm for hexafluorobenzene to 335 ppm for methylene iodide.[14,15] Different empirical models have been proposed to relate these values to the bulk solvent properties, such as the refractive index,[14,16] or the

group contribution model.[6,9,17] However, a complete description of the chemical shift of dissolved xenon was only given some years later by Jameson and co-workers.[18] The physical phenomenon behind the chemical shift, also called shielding, especially in computational chemistry, is the contact interaction between the electron clouds of xenon and the solvent molecules. This interaction depends on the organization of the solvent molecules surrounding the xenon atoms. Specifically, as reported by Jameson et al.,[18] the chemical shift of xenon dissolved in liquids depends on three factors: (1) the electronic structure of the solvent molecules, (2) the free volume available to xenon, and (3) the range of free volumes sampled over time.

Factor (1) determines the potential energy involved in the contact interaction which, in turn, strongly influences the deshielding effect. The free volume, that is the average size of the dynamic cages surrounding xenon atoms, depends on the solvent density and the organization of the solvent molecules. The chemical shift of dissolved xenon is inversely proportional to the free volume, following the same behavior as that of gaseous xenon adsorbed in porous structures. Thus, the voids explored by xenon can be treated like the cavities in solid-state materials. The importance of factor (3) lies in the fact that, as demonstrated in the literature,[19,20] the dependence of the xenon chemical shift with the distance of neighbor atoms is nonlinear. Thus, if during the NMR experiment xenon experiences very small free volumes, even if rarely, the average observed chemical shift will be strongly increased.

The xenon chemical shift is also temperature-dependent. Temperature has a strong influence on the density of the solvents and, thus, on the average free volume experienced by xenon. Generally, increasing the temperature increases the free volume, decreasing the chemical shift. For many systems, the dissolved xenon chemical shift follows a linear trend with temperature, with a dependence between about -0.2 ppm/K and -0.4 ppm/K.[7,8,11,21] Notably, Jameson and co-workers predicted an anomalous temperature dependence in the case of xenon dissolved in solvent molecules associated with specific interactions, i.e. hydrogen bonds.[18] This prediction was confirmed experimentally several years later by Vaara and co-workers who reported a non-linear temperature dependence for Xe dissolved in water.[22] Molecular dynamics simulations attributed this phenomenon to the temperature-decreasing local density of water

molecules around dissolved xenon atoms, coupled with a temperature-increasing term corresponding to the energy of xenon-water collisions.

In 2013, Morgado and co-workers conducted a thorough study on the liquid organization of several linear alkanes, branched alkanes, and cycloalkanes, combining experimental ^{129}Xe NMR chemical shifts with molecular dynamics simulations.[8] They rationalized the results in terms of the chemistry and organization of the chemical groups surrounding dissolved xenon atoms. They determined that xenon atoms are not distributed randomly in the liquid, but they are preferentially located in cavities in which their coordination sphere contains as many -CH_3 groups as possible, such as near the terminal groups of linear *n*-alkanes. Following a similar approach, some years later the authors demonstrated the formation of hydrogen-rich nanodomains in both hexane/perfluorohexane mixtures and perfluoroalkylalkane molecules.[11,21]

The surrounding environment of dissolved xenon not only influences the chemical shift but also other NMR parameters, such as relaxation times. The first works on the relaxation of ^{129}Xe dissolved in liquids were published by Jokisaari and Reisse during the 1990s.[23–26] The main focus of these papers was the study of the spin-lattice relaxation time of xenon dissolved in hydrogenated and deuterated benzene and cyclohexane. Together, these works indicate that (1) the dominant relaxation mechanism for xenon dissolved in hydrogenated solvents is the ^{129}Xe-^{1}H dipole-dipole interaction, at least in the temperature range of 298-323 K, and (2) at higher temperatures or in deuterated solvents the spin-rotation mechanism may play an important role. These results were later confirmed by Leigh and co-workers for xenon dissolved in water.[27] In the subsequent years, only a few papers on the relaxation of dissolved xenon were published, mostly regarding the possible applications of xenon in sensing and imaging. For example, several papers demonstrated that the T_1 of ^{129}Xe dissolved in blood depends on the degree of oxygenation, paving the way for the application of this technique in imaging and in the study of transport processes.[3,28–30] In 2016, Pines and co-workers demonstrated the possibility of using xenon-binding agents for relaxation-based sensing applications in the liquid state. They synthesized a specific binding agent with a cryptophane cage, a tetraxetan chelator for metals, a biotin moiety for binding, and a glutamate residue for solubilization.[31] This sensor responded

to the binding to avidin by reducing the spin-spin relaxation time of caged xenon by a factor of 4.

Lastly, pulsed field gradient NMR can be applied to study the self-diffusion process of xenon in a liquid medium. Comparing the experimental with the theoretical diffusion coefficient of xenon, determined, for example, with the simple Stokes-Einstein relationship or with more complex non-Fickian diffusion models, allows to determine the eventual presence of segregated nanodomains and/or molecular aggregates.

All these works show the great potential of investigating the structural organization of liquids using ^{129}Xe as a very sensitive and inert NMR probe. Experimental NMR parameters can be combined with computational chemistry to describe the microscopic structure of liquids with a high level of detail and, if needed, to obtain information about the solvation of xenon inside the liquid medium. In this Chapter, we applied the combined experimental/computational approach to a series of yet unexplored dihalomethane molecules (CH_2X_2 with X = Cl, Br, I). This work arises from the desire to explain the reported great differences in the chemical shifts of xenon dissolved in these liquids.[10,14] The reported data lacked a complete rationalization in terms of the complex interplay between the microscopic structure of the molecules and their interaction with xenon atoms, leaving a gap in the fundamental knowledge of the NMR of ^{129}Xe dissolved in liquids. This is especially true if we consider that these works were published before the complete theoretical explanations of Jameson and co-workers in 2004.[18] We measured the chemical shift at variable temperatures between 238 K and 348 K, in temperature ranges in which the compounds were in the liquid state. Moreover, we also measured the spin-lattice relaxation times and the xenon diffusion coefficients to investigate the dynamic properties of xenon and the eventual formation of molecular aggregates. Molecular dynamics (MD) simulations were also performed in similar temperature ranges, and from the results a series of clusters were extracted at regular intervals and used for the density functional theory (DFT) calculations of xenon shielding in the different solvents. The combination of the two approaches gives a complete overview of the structural organization of these molecules in the liquid state.

2.2 Experimental section

2.2.1 Materials

Dichloromethane (DCM), dibromomethane (DBM), and diiodomethane (DIM) with 99% purity were purchased from Sigma-Aldrich. All reagents were used as received without further purification.

2.2.2 Sample preparation

A small volume of liquid (0.2-0.4 mL) was placed into an NMR tube (Norell® Select Series, 5 mm outer diameter and 3.46 mm inner diameter) and immediately connected to a Schlenk line. The liquid was degassed under vacuum (6.0×10^{-2} torr) through multiple freeze-pump-thaw cycles until no gas bubbles were visible. Great care was taken to prevent the evaporation of the volatile liquids during this process. Xenon gas was quantitated by inserting it into a section of the manifold with a known volume and recording the pressure. The gas was then brought into contact with the sample and frozen inside the tube using liquid nitrogen. The tube was subsequently flame-sealed, ensuring that the sealing area was clear of any liquid droplets that could decompose and contaminate the sample. Samples for diffusion NMR experiments were prepared using the same method, with the addition of a thin capillary tube containing DMSO-d_6 (between 80 and 100 μL), inserted inside the NMR tube for deuterium lock. For all samples, the nominal xenon pressure was maintained between 2 and 4 bar.

2.2.3 NMR spectroscopy

^{129}Xe chemical shift and T_1 measurements were performed on a Bruker Avance 500 spectrometer operating at a Larmor frequency of 500.13 MHz for ^{1}H, corresponding to 139.09 MHz for ^{129}Xe. The instrument was equipped with a 5 mm double resonance inverse broadband probe (BBI). Spectra were acquired with a number of scans between 4 and 256 to obtain a good signal-to-noise ratio. The long relaxation delay was in the range of 200-300 s. The signal of free xenon gas loaded in an NMR tube was set to 0 ppm and used as an external chemical shift reference. The magnetic field drift was checked daily using a secondary external standard of xenon dissolved in benzene whose chemical shift was measured at 188.1 ppm at 298 K, in accordance with previous results

reported in the literature.[32] This allowed to reduce the experimental time needed to record the signal of the external reference. Spectra were collected at intervals of every 10 K across different temperature ranges, determined by the melting and boiling points of the samples: 238-308 K for dichloromethane, 248-318 K for dibromomethane, and 288-348 K for diiodomethane. Spin-lattice relaxation times were measured at 298 K using the Inversion Recovery pulse sequence (t1ir in the standard Bruker pulse sequence libraries). For each measurement, 10 delay increments were recorded with 8-32 scans for each increment and a relaxation delay in the range of 500-1600 s, depending on the sample, to ensure the complete relaxation of the xenon nuclei. Spin-lattice relaxation times were obtained by fitting the intensities with a mono-exponential function (see Section 1.2.1). The temperature was controlled using a BVT3000 variable temperature unit with an uncertainty of 0.1 K. Low-temperature experiments were performed by connecting a liquid nitrogen evaporator to the NMR probe. The evaporator was controlled with the same variable temperature unit.

Diffusion NMR experiments were conducted on a Bruker Avance Neo 500 spectrometer with a direct observe BBFO (broadband including fluorine) iProbe. The ^{129}Xe diffusion experiments utilized a stimulated-echo pulse sequence with a gradient pulse duration δ = 6 ms, and a diffusion time Δ = 50-80 ms, depending on the sample. For all experiments, a relaxation delay of 450-900 s, 16 scans, and 16 gradient linear steps were employed. ^{1}H diffusion experiments were also performed using the same pulse sequence and the following acquisition parameters: δ = 4.4 ms, Δ = 20-44 ms, 8 scans, and 24 gradient linear steps. The temperature was maintained at 298 K and controlled via airflow.

2.2.4 MD simulations

Classical all-atom Molecular Dynamics simulations were performed using the GROMACS software.[33,34] Six simulation boxes were prepared: three containing 1000 molecules each of CH_2Cl_2, CH_2Br_2, and CH_2I_2 (pure systems), and three containing a single Xe atom along with 1000 molecules of the same three solvents. These boxes were constructed with PACKMOL,[35] energy minimized, and equilibrated at the chosen temperature for 5 ns in the NPT ensemble at 1 atm using the Berendsen barostat with isotropic pressure coupling and periodic boundary conditions.[36] Long-range

electrostatic interactions were treated using the particle mesh Ewald method.[37] After equilibration, at each temperature a 10 ns production run was conducted in the constant-temperature, constant-pressure (NPT) ensemble using the Parrinello-Rahman barostat.[38,39] The leap-frog integrator with a timestep of 1 fs was employed, and bonds involving hydrogen atoms were constrained to their equilibrium geometries using the LINCS algorithm.[40]

The force field (FF) parameters used were derived from LigParGen,[41,42] and are based on the OPLS-AA force field.[43] The charge (q), Lennard-Jones radius (σ), and self-interaction energy (ε) parameters for all atoms in the simulations are listed in Table 2.1.

Table 2.1. Non-bonded interaction parameters for all the atoms in the simulated systems.

Molecule	Site	σ [nm]	ε [kJ/mol]	q [e]
CH_2Cl_2	Cl	0.3400	1.25520	-0.130
	C	0.3500	0.27614	-0.028
	H	0.2500	0.12552	0.144
CH_2Br_2	Br	0.3470	1.96648	-0.160
	C	0.3500	0.27614	-0.081
	H	0.2500	0.12552	0.161
CH_2I_2	I	0.3550	2.42672	-0.075
	C	0.3500	0.27614	-0.166
	H	0.2500	0.12552	0.158
	Xe	0.3948	1.89405	0.000

Average properties such as Radial Distribution Functions (RDF) and Mean Square Displacement (MSD) were calculated from the production run using GROMACS utilities. Diffusion coefficients were determined by fitting the MSD data linearly.

Clusters consisting of a Xe atom and its first solvation shell of dihalomethanes were extracted every 100 ps, yielding 100 clusters per production trajectory, using the MDAnalysis software.[44,45] The solvation shell was defined based on the radial

distribution functions, including any solvent molecule with at least one atom within 6.5 Å of the Xe atom. On average, the clusters contained around 18 ± 1 dihalomethane molecules at lower temperatures and 14 ± 1 molecules at higher temperatures. These clusters were then used for quantum mechanical (QM) calculations to determine the Xe shielding constant. The focus on the first solvation shell balances accuracy and computational cost, as the chemical shift is mainly influenced by close-contact interactions between Xe and the solvent.

2.2.5 QM calculations

Relativistic Density Functional Theory (DFT) calculations of the shielding constant of Xe, σ, in the clusters described above were performed using the ADF software.[46] The chemical shift, δ, can be determined as σ_{ref} - σ, where σ_{ref} is the shielding constant of xenon gas (an isolated Xe atom), calculated at the same level of theory. We initially tested the effect of the basis sets on a model cluster composed of a Xe atom and solvent molecules at both the ZORA scalar and spin-orbit levels. For the Xe@CH_2I_2 system, the spin-orbit contribution was around 10 ppm, depending on the basis set. Therefore, all calculations on the clusters extracted from the production trajectories were conducted at the ZORA spin-orbit level. The basis set chosen was QZ4P for Xe and TZ2P for the solvent molecules (all-electron for C and H, and frozen core 2p, 3p, and 4p for chlorine, bromine, and iodine, respectively), which represents a balance between accuracy and computational cost. Since there is no covalent bond between xenon and dihalomethane molecules, the requirements for the solvent basis set are expected to be less stringent. This is confirmed by the data in Table 2.2, which shows the preliminary calculation of chemical shift values obtained with different levels of theory and coupling methods.

The GGA BLYP functional was used for all calculations to maintain consistency with previous works, where very good results were achieved using a similar protocol to calculate the NMR properties of xenon in ionic liquids.[47] While it is well known that hybrid functionals provide more accurate predictions of NMR properties, they do so at a higher computational cost. Specifically, for ^{129}Xe in organic environments, the BHandHLYP hybrid functional has been shown to produce results close to the CCSD(T) values for a model Xe-benzene dimer.[48] Thus, we also tested the BHandHLYP functional for our systems. For the limited cases examined, the shielding

values showed improvement, with differences from BLYP being in the direction and magnitude needed for an almost quantitative agreement with experimental results. However, the computational cost was significantly higher compared to BLYP. This high computational demand renders the BHandHLYP protocol impractical for our study, where the total number of clusters needed to obtain final averages is on the order of 10^3.

Lastly, for model dimers consisting of a xenon atom and a dihalomethane molecule, the interaction energy as a function of distance was calculated at the ZORA-SO-BLYP-G3/QZ4P level for all atoms, where BLYP-G3 includes the Grimme correction to account for dispersive interactions.[49]

Table 2.2. Chemical shift of ^{129}Xe in randomly selected clusters of dihalomethane molecules, extracted from the production trajectories, as a function of the basis set and of the level of theory employed.

	DZ				**TZP**				**TZ2P**			
	Scalar		**Spin-orbit**		**Scalar**		**Spin-orbit**		**Scalar**		**Spin-orbit**	
	All-electron	Frozen core	All-electron	Frozen core	All-electron	Frozen core	All-electron	Frozen core	All-electron	Frozen core	All-electron	Frozen core
DCM	193.41	194.73	197.37	193.41	204.48	206.06	208.14	209.83	204.89	206.49	208.55	210.26
DBM	242.7	242.37	243.66	238.15	258.24	258.32	258.79	259.6	259.3	259.47	259.91	260.58
DIM	394.77	390.28	383.94	382.24	400.22	396.86	389.23	389.13	422.22	419.48	410.14	410.26

2.3 Results and discussion

2.3.1 ^{129}Xe NMR Spectroscopy

The ^{129}Xe NMR spectra of all the samples showed a single, intense, and sharp peak, typical of xenon dissolved in isotropic liquid samples. The representative spectra of xenon dissolved in dichloromethane (DCM, CH_2Cl_2), dibromomethane (DBM, CH_2Br_2), and diiodomethane (DIM, CH_2I_2) acquired at 298 K are shown in Figure 2.1.

The experimental chemical shifts cover a wide range of more than 130 ppm, from 189.9 ppm for xenon loaded in dichloromethane to 324.0 ppm in the case of diiodomethane, while dibromomethane sits in between the two at 244.4 ppm. We have

already discussed how the chemical shift of dissolved xenon depends on the electronic structure of the solvent and on the free volume probed by xenon nuclei. Since the three molecules are structurally very similar, we can expect the free volume to have a minor impact on the chemical shift, especially when compared with the differences in the electronic structure given by the presence of different halogen atoms. Thus, we can qualitatively give a first interpretation of the results in terms of a xenon-halogen interaction that produces a shielding response in the order Cl < Br < I.

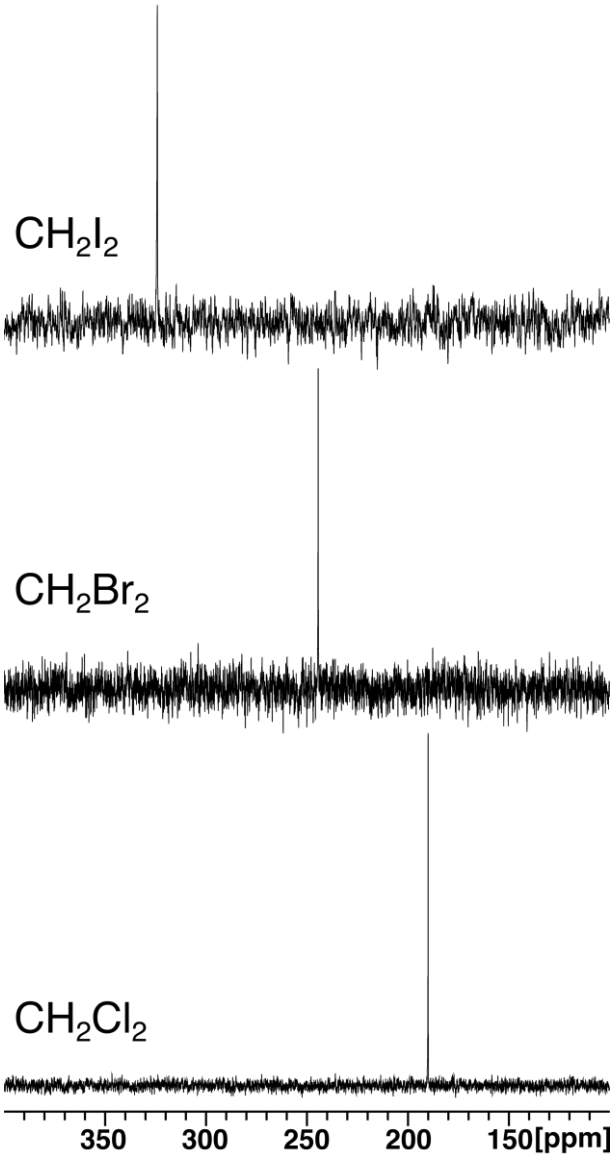

Figure 2.1. ^{129}Xe NMR spectra of xenon dissolved in dichloromethane, dibromomethane, and diiodomethane acquired at 298 K.

To further investigate the chemical shift differences, we performed variable temperature xenon NMR measurements in temperature ranges in which the molecules are in the liquid state. The results are reported in Table 2.3 and represented in the left panel of Figure 2.2.

Table 2.3. Variable temperature ^{129}Xe chemical shifts of xenon dissolved in dichloromethane (DCM), dibromomethane (DBM), and diiodomethane (DIM).

T [K]	$\delta_{Xe@DCM}$ [ppm]	$\delta_{Xe@DBM}$ [ppm]	$\delta_{Xe@DIM}$ [ppm]
238	214.8	-	-
248	210.8	270.2	-
258	206.9	265.3	-
268	202.8	260.1	-
278	198.7	254.8	-
288	194.2	249.4	328.2
298	189.9	244.4	324.0
308	185.7	238.9	319.4
318	-	233.7	314.8
328	-	-	310.3
338	-	-	305.7
348	-	-	301.1

The error on the chemical shift is ±0.1 ppm.

It can be seen that the chemical shifts decrease linearly with temperature. By fitting the data to a linear function, we determined the chemical shift temperature dependencies as -0.42 ppm/K for DCM, -0.52 ppm/K for DBM, and -0.46 ppm/K for DIM, with an estimated relative uncertainty of ±5%. These values are significantly higher than those reported by Morgado and co-workers for several *n*-alkanes, branched alkanes, and cycloalkanes, which are approximately between -0.2 ppm/K and -0.3 ppm/K.[50] As demonstrated by the authors, the chemical shift of xenon dissolved in these systems is mainly determined by the interaction of xenon with hydrogen atoms,

with a smaller influence of the Xe-C interaction. In the case of dihalomethanes, the significantly higher temperature dependencies may suggest that the chemical shift depends on different interactions, such as the xenon-halogen interaction.

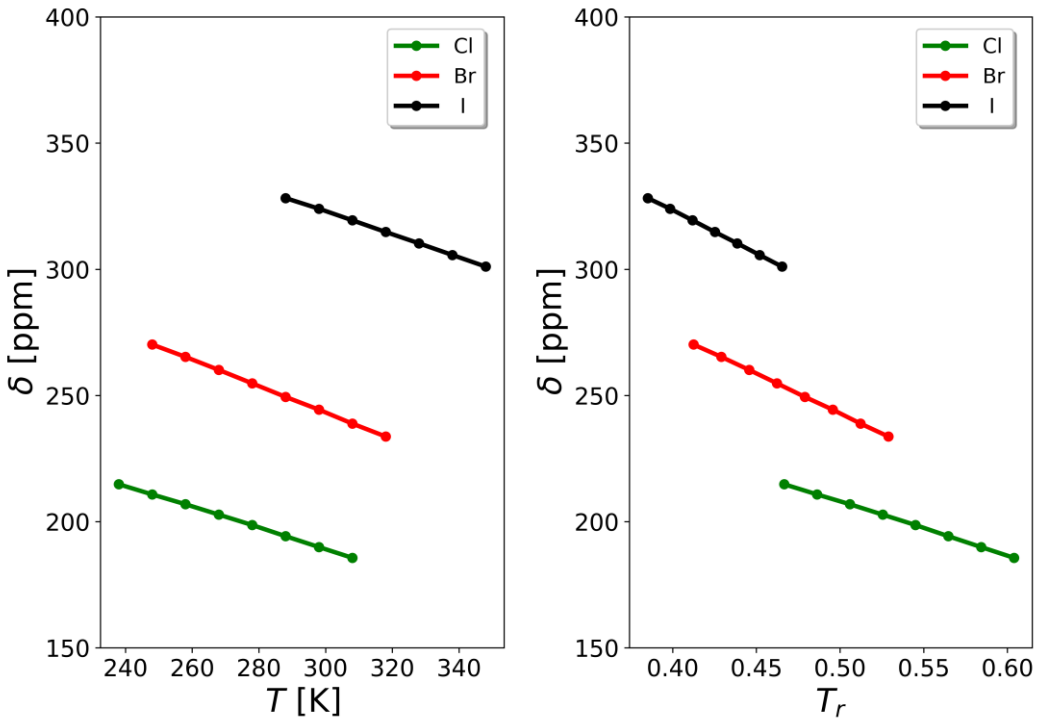

Figure 2.2. Plot of the chemical shift of ^{129}Xe dissolved in dichloromethane (green), dibromomethane (red), and diiodomethane (black). The data are represented as a function of temperature (left panel) and as a function of the reduced temperature (right panel). The lines are only a guide to the eye.

While the left panel of Figure 2.2 shows notable differences in the chemical shifts of the haloalkanes, it is important to consider that at the same temperature, different chemical species may exist under varying thermodynamic conditions. This makes direct comparison of their chemical shifts at different temperatures challenging. To ensure a fair comparison under identical thermodynamic conditions, the chemical shift of dissolved xenon is also plotted as a function of reduced temperature ($T_r = T/T_c$, where T_c is the critical temperature) in the right panel of Figure 2.2. The behavior of the chemical shift as a function of the reduced temperature is consistent with the behavior as a function of temperature. This confirms that, even under the same thermodynamic

conditions, the chemical shift of dissolved xenon is strongly dependent on the type of halogen atom in the CH_2X_2 molecule.

To gain a deeper insight into the observed chemical shift differences and their connection to the structural organization of the samples, we use pulsed field gradient NMR to determine the diffusion coefficients of xenon dissolved in dihalomethanes D(Xe) and the diffusion coefficients of the protons of dihalomethanes $D(^1H)$. The measurements were carried out at 298 K, and the results are summarized in Table 2.4.

Table 2.4. Experimental (Expt.) and simulated diffusion coefficients of xenon dissolved in dihalomethanes, D(Xe), protons of dihalomethanes, $D(^1H)$, and dihalomethane molecules, D(molecule). Experimental values were obtained from pulsed field gradient NMR measurements at 298 K. Simulations were carried out at 300 K.

Sample	***D*(Xe) [m²/s] Expt.**	***D*(^{1}H) [m²/s] Expt.**	***D*(Xe) [m²/s] Original OPLS FF**	***D*(molecule) [m²/s] Original OPLS FF**	***D*(Xe) [m²/s] Modified OPLS FF**	***D*(molecule) [m²/s] Modified OPLS FF**
DCM	3.96×10^{-9}	3.17×10^{-9}	3.90×10^{-9}	3.70×10^{-9}	-	-
DBM	1.96×10^{-9}	1.42×10^{-9}	2.56×10^{-9}	1.44×10^{-9}	3.09×10^{-9}	1.30×10^{-9}
DIM	8.50×10^{-10}	4.77×10^{-10}	0.72×10^{-9}	0.97×10^{-9}	1.18×10^{-9}	0.84×10^{-9}

The error on the experimental diffusion coefficients is ±5%.

We found that the diffusion coefficient of xenon in dichloromethane is slightly higher than in water (2.2×10^{-9} m²/s),[51] while the diffusion coefficient of xenon in dibromomethane is very close to this value. In contrast, xenon diffuses much more slowly in diiodomethane. This trend is also observed in the diffusion of the dihalomethane molecules themselves, as reflected in the $D(^1H)$ values.

These findings can be understood in terms of the viscosities of the pure liquids. Typically, a higher viscosity leads to slower diffusion for both the solvent molecules and any dissolved species. The reported viscosities of CH_2Cl_2 and CH_2Br_2 at 298 K are 0.413 cP and 0.980 cP, respectively,[52] while for CH_2I_2, the viscosity is 2.76 cP at 293 K.[53] The measured diffusion coefficients decrease as the viscosity of the liquids increases. Specifically, the viscosity of CH_2Cl_2 is nearly an order of magnitude lower than that of CH_2I_2, and the corresponding diffusion coefficients for both ^{1}H and Xe follow the inverse trend almost quantitatively. In addition to that, the viscosity of

CH_2Br_2 closely matches that of water (0.89 cP at 298 K), and the diffusion coefficients of dissolved xenon in these species are similar. The expected strict correlation between viscosity and diffusion coefficients rules out the presence of molecular aggregates, confirming that these liquids are completely isotropic and unperturbed by the presence of xenon. These diffusion measurements also provide valuable experimental validation of the molecular dynamics (MD) simulations, particularly regarding the simulated solvent density and dynamic behavior. As shown in Table 2.4, the experimental diffusion coefficients align well with the simulation results, both for solvent molecules and xenon atoms.

^{129}Xe spin-lattice relaxation time is an additional useful NMR parameter to probe the structural organization of the dynamic cages surrounding xenon atoms. For this reason, we measured the spin-lattice relaxation times of xenon dissolved in the three dihalomethanes at 298 K using the Inversion Recovery pulse sequence (see Section 1.2.1). The T_1 values were determined by a non-linear fit of the measured intensities to a single exponential function. The exponential fit of the normalized intensity as a function of the delay time measured for xenon dissolved in diiodomethane at 298 K is shown in Figure 2.3 as a representative curve. The point corresponding to a delay time of 40 s has been excluded from the fit since this delay was close to the inversion point and, thus, the intensity of the peak was close to zero, resulting in a very low signal-to-noise ratio.

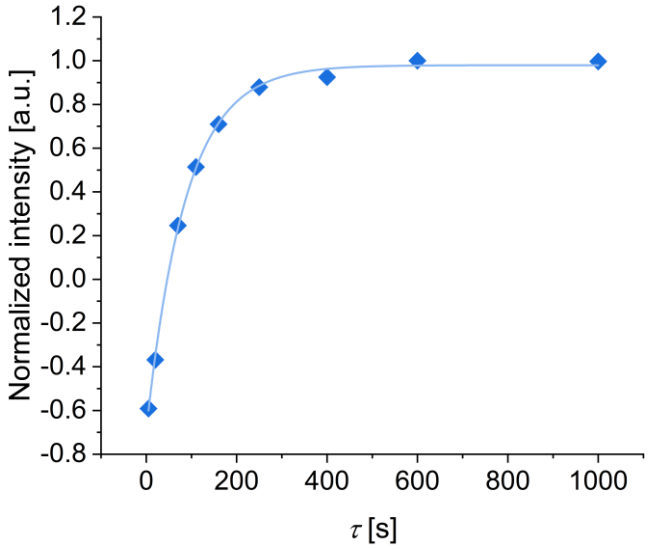

Figure 2.3. ^{129}Xe Inversion Recovery measurement of xenon dissolved in diiodomethane at 298 K. The line is a linear fit to a single exponential function.

The measured spin-lattice relaxation times are 293 s for Xe@DCM, 113 s for Xe@DBM, and 87 s for Xe@DIM. These values behave similarly to the diffusion coefficients which decrease abruptly from dichloromethane to diiodomethane (Table 2.4). Xenon dissolved in alkanes and benzene has a spin-lattice relaxation time approximately in the range of 170-270 s.[24,26,54] As discussed in Section 2.1, the preponderant relaxation mechanism for xenon in liquids is the ^{129}Xe-^{1}H dipolar interaction.[25,26] Indeed, it has been shown that the T_1 of xenon dissolved in alkanes decreases with increasing the number of protons, from 217 s for xenon in hexane to 171 s for decane. In our case, the measured T_1 values seem to depend on the nature of the halogen atoms, with values decreasing by almost four times from Xe in DCM to Xe in DIM. However, it is very unlikely that the xenon-halogen dipolar interaction plays any role in xenon relaxation. The dipolar interaction depends on the product of the gyromagnetic ratios of the interacting nuclei (see Section 1.1.3). The most abundant NMR active nuclei for chlorine and iodine are ^{35}Cl (75.8% natural abundance) and ^{127}I (about 100% natural abundance), with gyromagnetic ratios of 4.18 MHz/T and 8.58 MHz/T, respectively. Bromine has two NMR-active isotopes, each with a natural abundance close to 50%: ^{79}Br and ^{81}Br. Their gyromagnetic ratios are 10.70 MHz/T and 11.54 MHz/T, respectively. Comparing these values with those of ^{1}H, which has a natural abundance of 99.99% and a gyromagnetic ratio of 42.58 MHz/T, it becomes evident that the ^{129}Xe-^{1}H dipolar interaction is much more intense than the dipolar interactions between xenon and NMR-active halogen nuclei. Thus, most likely the dominating relaxation mechanism remains the xenon-hydrogen dipolar interaction, and no xenon-halogen interaction is involved in the process. Instead, the differences in the relaxation times could be determined by the different rotational dynamics of the dihalomethanes, which in turn can be related to their viscosities. The influence of the rotational dynamics of the solvent on the spin-lattice relaxation of xenon has been demonstrated in the case of benzene.[25] We did not conduct in-depth studies on the relationship between rotational dynamics and spin-lattice relaxation time of dissolved xenon because it was not the main focus of this work. Nevertheless, this topic is still unexplored, and it could be the object of future works of the research group.

2.3.2 MD simulations and QM calculations

Before conducting detailed calculations on the chemical shift of dissolved xenon, we analyze the properties of the simulated bulk phase of the dihalomethane molecules. Figure 2.4 shows a comparison between the simulated and experimental densities at different temperatures, while the simulated self-diffusion coefficients of the molecules are reported in Table 2.4.

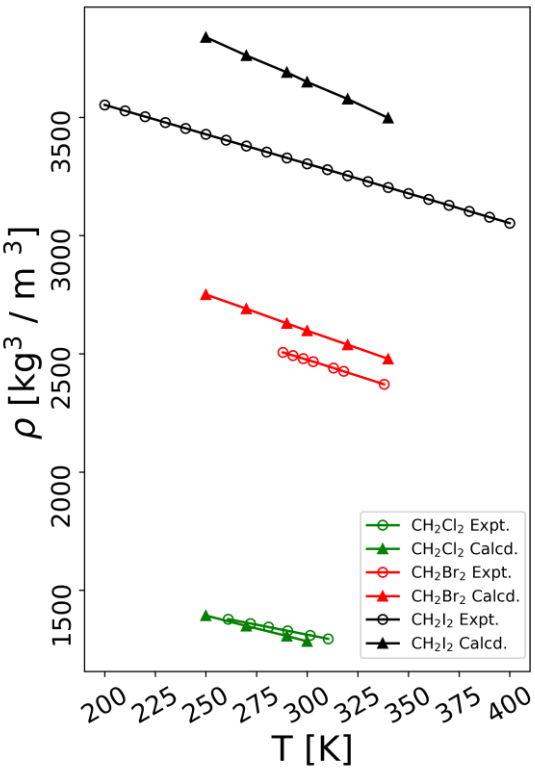

Figure 2.4. Experimental (empty circles) and simulated (full triangles) densities of the dihalomethanes at different temperatures. The experimental values are taken from the literature.[55–57]

The simulations reproduce the density of CH_2Cl_2 accurately over a wide range of temperatures, with a peak discrepancy of 2% between the two values at 300 K. The density of dibromomethane is instead slightly overestimated: at 300 K, the simulated value is 2.598 g/mL, while the experimental value at 303 K is 2.467 g/mL, leading to an overestimation of about 5%. These discrepancies are more pronounced in the case of diiodomethane, most likely due to the high atomic weight of iodine: the relative error

between the simulated density at 300 K, 3.586 g/mL, and the experimental value, 3.30 g/mL, is about 8.7%. As shown in Table 2.4, the self-diffusion properties of the molecules are well reproduced: the simulated and experimental diffusion coefficients decrease noticeably as the solvent molecular weight and density increase.

Despite the overestimation of the densities, the simulations of the bulk phases of the solvents are overall sufficient, especially considering that obtaining simulated densities very close to the experimental values is nontrivial. To evaluate the impact that the overestimated density may have on the calculation of the chemical shift of dissolved xenon, before adjusting the Lennard-Jones parameters to better match the bulk phase density, we proceeded with calculating the ^{129}Xe chemical shift to have a comparison with the experimental data.

We examine the dihalomethane systems with a xenon atom dissolved in the simulation box. Figure 2.5 shows the radial distribution functions (RDF) for the distances between xenon and the X and H atoms in CH_2X_2 (X = Cl, Br, I) at 300 K.

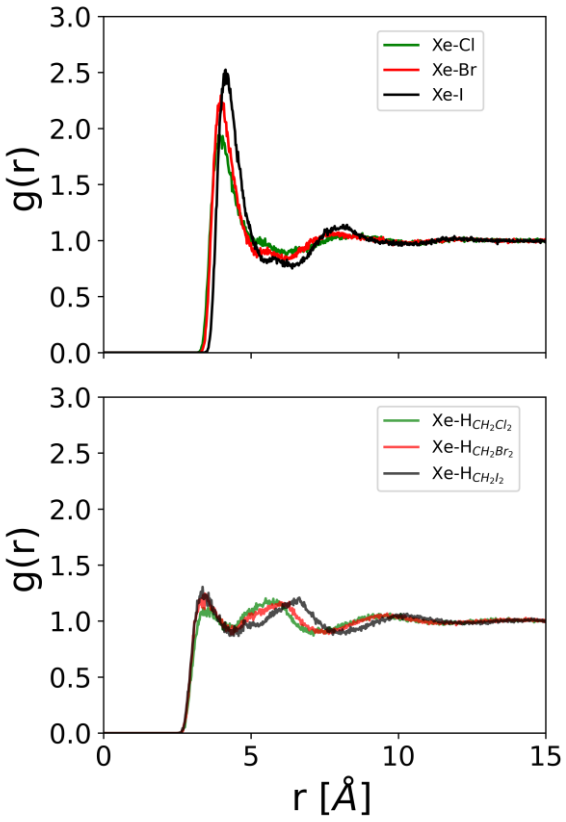

Figure 2.5. Radial Distribution Functions (RDF), $g(r)$, of the distance between xenon and halogen (top) and hydrogen (bottom) atoms of the dihalomethane molecules at T = 300 K.

The results reveal a strong interaction between xenon and the halogen atoms of the solvent, intensifying as the atomic weight of the halogen increases. In contrast to that, the correlation between xenon and the hydrogen atoms is significantly weaker across all three dihalomethanes. As a result, the solvation shell structure of xenon is primarily governed by xenon-halogen interactions. Furthermore, the calculated diffusion coefficient for xenon at 300 K aligns well with the experimental data at 298 K (see Table 2.4), reinforcing the reliability of the chosen force field for accurately capturing structural and dynamic properties in the bulk phase.

We can now analyze the ^{129}Xe NMR parameters obtained from the simulations. As an example, Figure 2.6 shows a cluster extracted from the MD simulations of CH_2Br_2 at 300 K, used for the subsequent DFT calculations. Clearly, most of the closest contacts in the xenon coordination sphere are between xenon and halogen atoms. Moreover, the average number of dihalomethane molecules that had at least one atom within 6.5 Å of the xenon atom was independent of the type of dihalomethane molecule, being 18 ± 1 at lower temperatures and 14 ± 1 at higher temperatures. This demonstrates that the average size of the dynamic cage containing xenon does not depend on the nature of the halogen atoms. In other words, the free volume experienced by xenon is, on average, similar in all the systems.

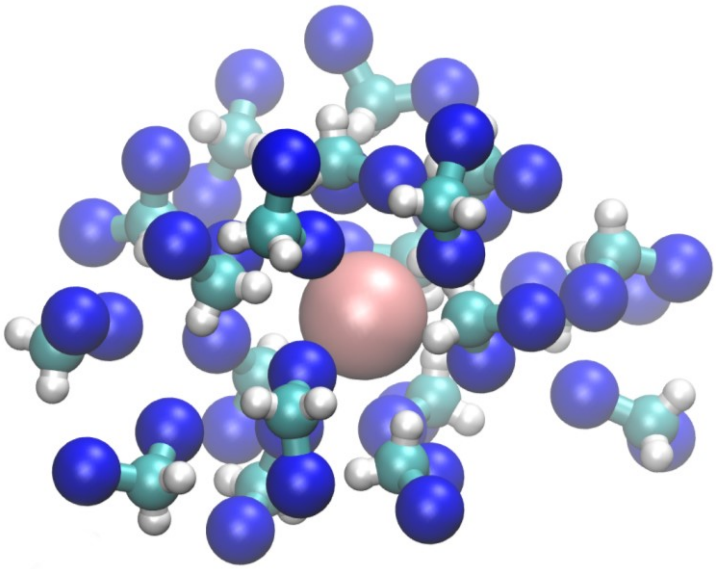

Figure 2.6. Cluster extracted from the trajectory of the Xe@CH_2Br_2 system at T = 300 K. Colors are as follows: Xe, pink; Br, blue; C, cyan; H, white. Close contacts between xenon and bromine are visible.

Figure 2.7 shows the instantaneous and average ^{129}Xe chemical shift values. Although the instantaneous values are strongly oscillating, as already observed in previous works,[47] the average values converge at around 5 ns. The final average values of the three systems calculated at different temperatures are shown in the left panel of Figure 2.8.

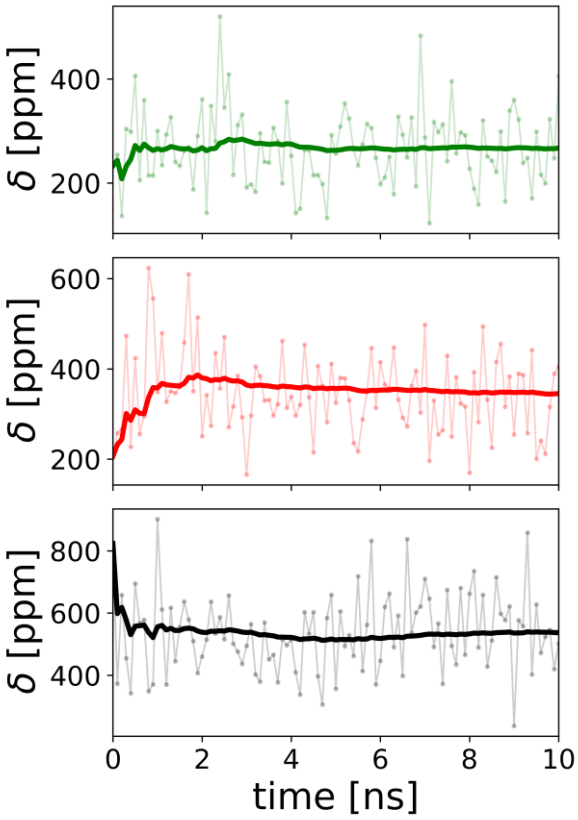

Figure 2.7. Instantaneous (points) and average (lines) values of the ^{129}Xe chemical shift calculated from the clusters extracted from the trajectories at T = 300 K. Xe@CH_2Cl_2, top, green; Xe@CH_2Br_2, middle, red; Xe@CH_2I_2, bottom, black.

While the qualitative trends are accurate, a notable discrepancy compared to the experimental values remains. Part of this difference may be attributed to the fact that the two methods used to calculate the shielding constant lie on different levels of theory. Specifically, the reference shielding value is obtained using a purely quantum chemical approach for a xenon atom in a vacuum, whereas the shielding constant for xenon in solution is derived from averaging over clusters generated by classical MD simulations.

This difference in methodology may introduce systematic deviations in the resulting shielding constants.

To address this issue, we rescaled all the calculated shielding constants so that the calculated and experimental values for Xe in CH_2Cl_2 align perfectly. To achieve this, we determined the average offset between the calculated and experimental xenon chemical shifts at the temperatures studied (250 K, 270 K, and 300 K), which revealed an overestimation of 84.26 ppm (see Figure 2.8, right panel). While the corrected chemical shift for Xe in CH_2Br_2 is reasonably close to the experimental data, the shift for Xe in CH_2I_2 remains significantly overestimated.

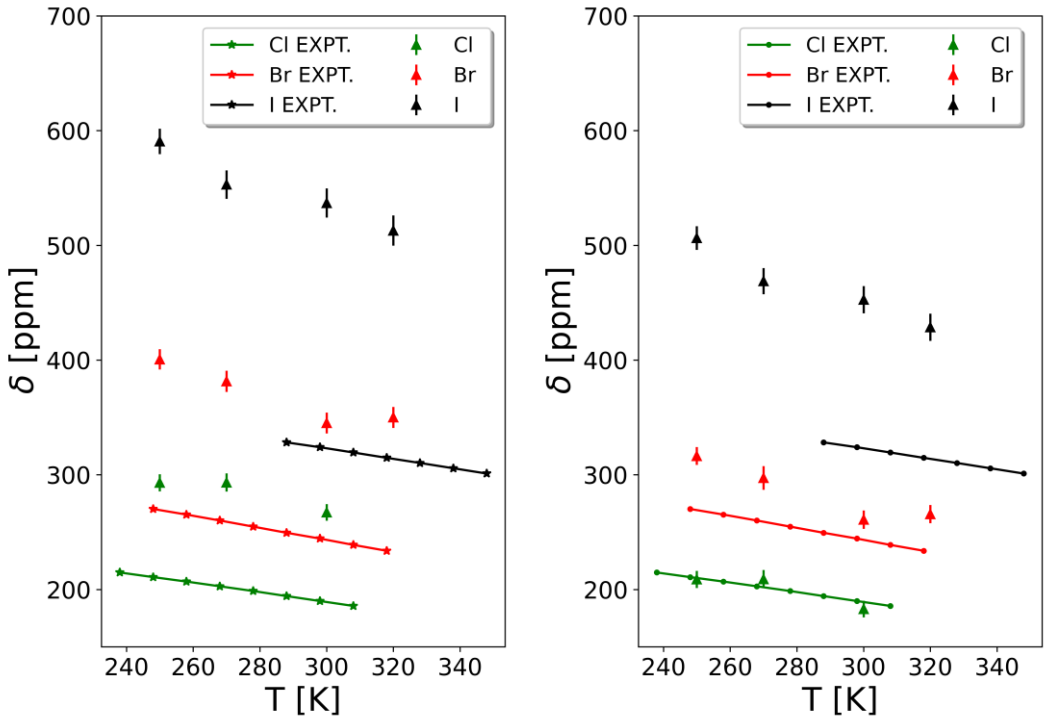

Figure 2.8. Comparison between calculated and experimental values of the ^{129}Xe chemical shift of xenon dissolved in dihalomethanes. Triangular markers represent the calculated values, while the vertical bars represent the error on the average, ranging from 7 to 12 ppm. Full dots represent experimental values and the lines are simply a guide to the eye. (Left panel) Unscaled calculated ^{129}Xe chemical shifts; (right panel) ^{129}Xe chemical shifts scaled down by 84.26 ppm.

Thus, we decided to verify if the large discrepancies between the calculated chemical shifts for diiodomethane, and, to a lesser extent, dibromomethane, were due to the error in the simulated bulk densities of these solvents. Specifically, we decided to

change the Lennard-Jones radius to a value that reproduces the experimental density more accurately. We ran a series of simulations at 300 K varying the Lennard-Jones radius in steps of 0.01 Å between 3.48 Å and 3.58 Å for Br, and between 3.57 Å and 3.80 Å for I. Simulations were 10 ns long, and the average densities were calculated over the last 5 ns. These calculations revealed that the radius giving the correct density at 300 K was 3.5764 Å for Br in CH_2Br_2 and 3.7914 Å for I in CH_2I_2. Both the radii are significantly higher than those used in the initial set of simulations (see Table 2.1). Moreover, the simulated self-diffusion coefficients of the dihalomethane molecules were in good agreement with the experimental values (see Table 2.4)

Using the new set of parameters, we ran again all the simulations for DBM and DIM. The results are shown in Figure 2.9.

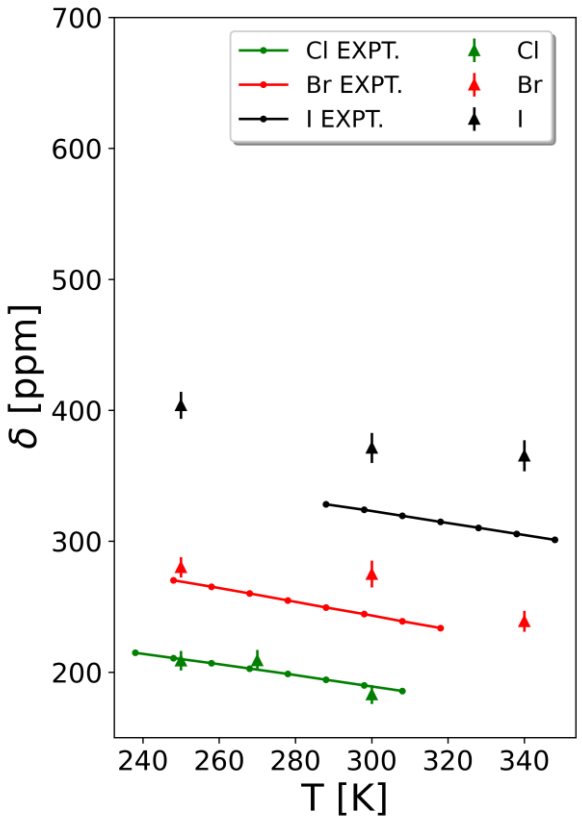

Figure 2.9. Comparison between calculated and experimental values of the chemical shift of xenon dissolved in dihalomethanes. Triangular markers represent the calculated values, while the vertical bars represent the error on the average, ranging from 7 to 12 ppm. Full dots represent experimental values and the lines are simply a guide to the eye. The chemical shifts of ^{129}Xe in CH_2Br_2 and CH_2I_2 are calculated using the correct Lennard-Jones radii. All the chemical shifts are also scaled down by 84.26 ppm.

It can clearly be seen that the calculated chemical shifts for xenon dissolved in CH_2Br_2 and in CH_2I_2 reproduce the experimental data much more accurately compared to the values obtained with the original set of simulations. Overall, this indicates that the computed densities have a very significant impact on the outcome of the simulations. Future computer simulations of the NMR parameters of chemical species dissolved in liquids will have to carefully evaluate the correct simulated bulk phase density, which can be quite demanding in terms of computational cost.

Lastly, we decided to investigate how the precise orientation of the solvent molecules in the solvation shell of xenon atoms affects the chemical shift. We calculated the chemical shift of model dimers composed of a xenon atom and a dihalomethane molecule with different orientations, considering three different cases: (1) xenon atom approached from the CX_2 side, (2) xenon atom approached from the CH_2 side, and (3) C-X bond collinear with the X-Xe distance vector. The results are shown in Figure 2.10. These results cannot be compared to the experimental results quantitatively since the dimer approximation is too simple. However, these calculations are qualitatively informative on the structural organization of the cage of solvent molecules surrounding xenon atoms.

An interesting result is that the interaction energies are slightly higher, in absolute value, when xenon is approached from the CH_2 side compared to the CX_2 side, especially in the case of dichloromethane. This non-trivial result can be attributed to a strong polarization of the bonds in the dihalomethane molecule due to the high electronegativity of halogen atoms, which generates stronger dipole-induced dipole interactions with xenon thanks to the closer distance when facing hydrogen atoms. Indeed, the equilibrium distance in Xe···H_2-C is essentially the same for all three solvents, while in Xe···X_2-C it is overall higher and dependent on the halogen atom. The chemical shifts for these two geometries have opposite trends: for Xe···H_2-C, $\delta(Xe@CH_2Cl_2) > \delta(Xe@CH_2Br_2) > \delta(Xe@CH_2I_2)$, while, for Xe···$X_2$-C, the opposite trend is observed, $\delta(Xe@CH_2I_2) > \delta(Xe@CH_2Br_2) > \delta(Xe@CH_2Cl_2)$. The latter reproduces correctly the experimental trend, indirectly confirming that xenon is preferentially interacting with halogen atoms in solution, as observed from the representative cluster shown in Figure 2.6. The last case in which Xe is collinear to the X-C bond was tested because it could potentially explain the high deshielding of ^{129}Xe

in diiodomethane. However, the calculated chemical shift values follow the trend $\delta(Xe@CH_2Br_2) > \delta(Xe@CH_2I_2) > \delta(Xe@CH_2Cl_2)$, clearly showing that this geometry is not able to reproduce the experimental data accurately.

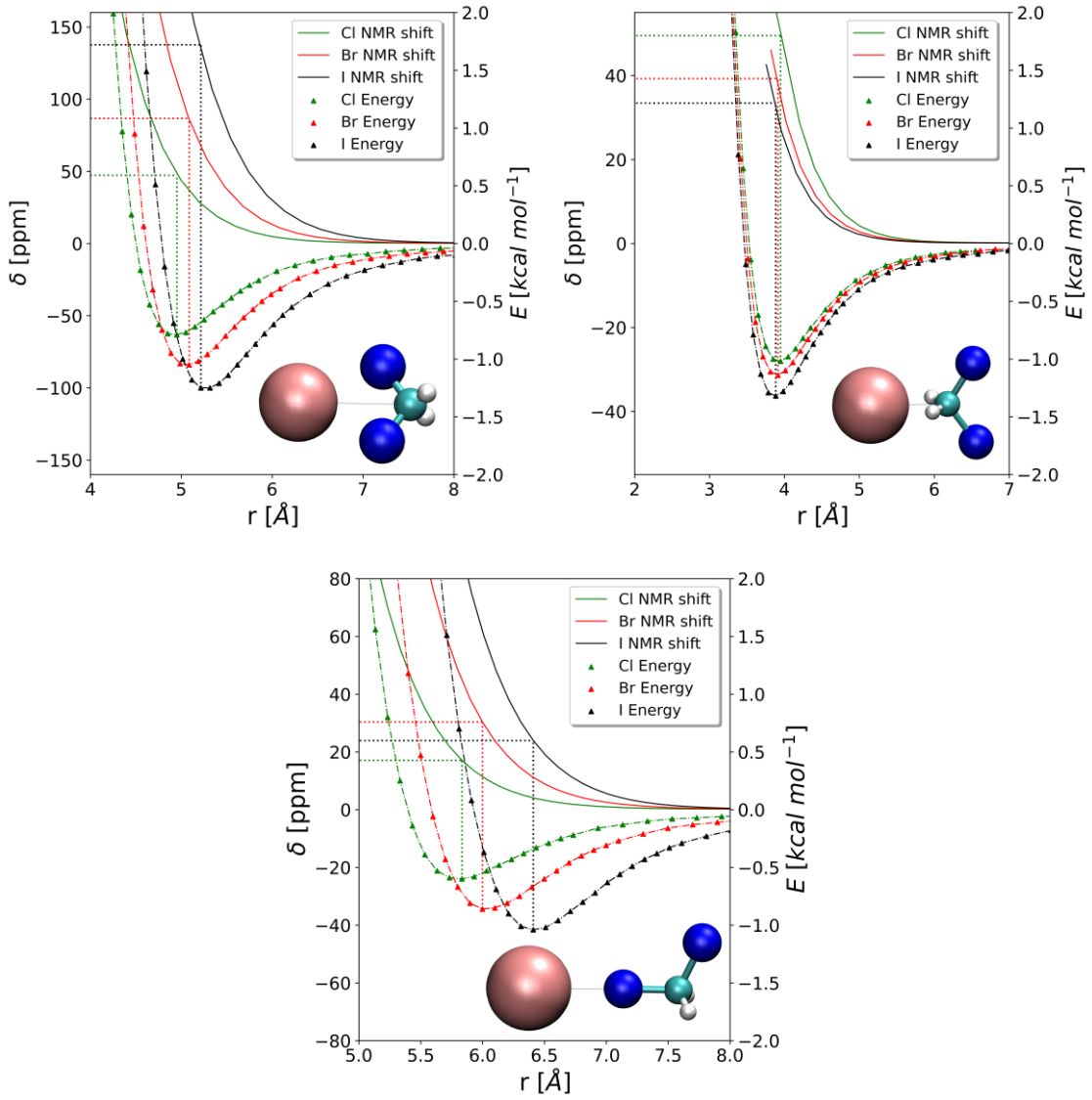

Figure 2.10. Calculated interaction energies and ^{129}Xe chemical shifts for model dimers composed of a xenon atom and a dihalomethane molecule with different orientations: (top left) xenon atom approached from the CX_2 side, (top right) xenon atom approached from the CH_2 side, and (bottom) C-X bond collinear with the X-Xe distance vector. Colors are as follows: Xe, pink; X, blue; C, cyan; H, white.

2.4 Conclusions

In conclusion, we investigated the liquid structure of dihalomethanes (CH_2X_2, X = Cl, Br, I) employing a combined approach based on experimental ^{129}Xe NMR measurements, molecular dynamics simulations, and quantum mechanics calculations.

Experimentally, we used xenon as a chemically inert NMR probe to test both the structural and the dynamic parameters of the solvents. The chemical shifts of dissolved xenon increase significantly in the order $CH_2Cl_2 < CH_2Br_2 < CH_2I_2$ in a wide range of temperatures. This holds even when the chemical shifts are plotted against the reduced temperature, effectively comparing the solvents in the same thermodynamic states. On the other hand, the diffusion coefficients of dissolved xenon and its spin-lattice relaxation times follow an opposite trend, decreasing substantially in the order $CH_2I_2 < CH_2Br_2 < CH_2Cl_2$. These trends derive from two different features of the solvent: its structural organization and its dynamic properties. The chemical shift depends on the electronic structure of the dynamic cages hosting xenon atoms, while the increasing viscosity can account for the significant decrease of the diffusion coefficients with an almost quantitative agreement. Rationalizing the behavior of the spin-lattice relaxation time is non-trivial. It is unlikely that this parameter is influenced by the weak xenon-halogen dipolar interaction, especially when compared to the much stronger ^{129}Xe-^{1}H dipolar interactions which represent the dominating relaxation mechanism for xenon dissolved in liquids. Thus, the differences in the relaxation times could be explained in terms of the different rotational dynamics of the solvents, which in turn are correlated to the viscosities. We did not conduct in-depth studies on this since it was not the focus of this work, but this certainly represents an interesting and unexplored research topic.

Classical molecular dynamics simulations reveal that the number of molecules in the first coordination sphere of xenon is independent of the halogen atom, indicating that the overall free volume experienced by xenon is similar in all the systems. However, the simulations show that xenon atoms in the dynamic cages are preferentially interacting with the halogen atoms, as opposed to carbon and hydrogen, as clearly highlighted by the radial distribution functions. Density functional theory calculations on clusters extracted from the trajectories accurately reproduce the experimental chemical shifts dependencies on temperature and on the nature of the halogen atoms. Moreover, after correcting the Lennard-Jones parameters of Br and I to

accurately reproduce the density of CH_2Br_2 and CH_2I_2, there is good agreement between the experimental and simulated chemical shifts, especially considering the difficulty in simulating correctly the bulk phase of heavier solvents. This demonstrates the utmost importance of density in computer simulations concerning the NMR parameters of dissolved species and, in a broader sense, solvation properties in general.

DFT calculations on model Xe-CH_2X_2 dimers confirm that the xenon-halogen interaction is the main responsible for the chemical shift dependence. These calculations also reveal the dependence of the chemical shift on the orientation of the molecules, showing that the experimental trends are reproduced accurately when xenon is approached from the X_2C side.

This work, besides giving interesting and detailed information on the structure and dynamics of Xe@CH_2X_2 systems, adds to the body of knowledge concerning the physical phenomena determining the NMR parameters of dissolved ^{129}Xe, and solvation and solution behavior in general, particularly for apolar solutes in organic media. We also highlighted the power of a combined experimental and computational NMR approach in studies where "geometry" is the central focus in a broad sense. For example, in Natural Products research, it is well-known that calculating ^{1}H and ^{13}C shifts of some presumed structures using DFT methods can be a crucial tool for structural elucidation, especially when the true structure of an unknown substance cannot be determined by the analysis of experimental NMR spectra.[58,59] By comparing the calculated and the experimental chemical shifts, the correct structure among a high number of candidates can be determined.

In this study, we employed a similar approach but focused not on the geometry of a covalent molecule, but on the far more complex average structure of a solvation shell surrounding a solute. This method incorporates molecular dynamics (MD) simulations to account for dynamics, and DFT calculations to consider quantum effects. We believe this approach will increasingly prove to be a powerful tool for indirectly probing the intricate structural characteristics of novel materials.

2.5 Bibliography

[1] E. J. M. Filipe, L. M. B. Dias, J. C. G. Calado, C. McCabe, G. Jackson, *Phys.*

Chem. Chem. Phys. **2002**, *4*, 1618–1621.

[2] Y. Tomonaga, M. S. Brennwald, D. M. Livingstone, G. Tomonaga, R. Kipfer, *PLoS One* **2014**, *9*, 1–8.

[3] G. Norquay, G. Leung, N. J. Stewart, G. M. Tozer, J. Wolber, J. M. Wild, *Magn. Reson. Med.* **2015**, *74*, 303–311.

[4] G. Norquay, G. Leung, N. J. Stewart, J. Wolber, J. M. Wild, *Magn. Reson. Med.* **2017**, *77*, 1399–1408.

[5] T. R. Stengle, S. M. Hosseini, K. L. Williamson, *J. Solution Chem.* **1986**, *15*, 777–790.

[6] Y. H. Lim, N. Nugara, A. D. King, *Appl. Magn. Reson.* **1995**, *8*, 521–534.

[7] J. Saunavaara, J. Jokisaari, *J. Magn. Reson.* **2006**, *180*, 58–62.

[8] P. Morgado, R. Bonifacio, F. G. Martins, E. J. M. Filipe, *J. Phys. Chem. B* **2013**, *117*, 9014–9024.

[9] Y. H. Lim, A. D. King, *J. Phys. Chem.* **1993**, *97*, 12173–12177.

[10] Y. H. Lim, A. R. Calhoun, A. D. King, *Appl. Magn. Reson.* **1997**, *12*, 555–574.

[11] P. Morgado, L. F. G. Martins, E. J. M. Filipe, *Phys. Chem. Chem. Phys.* **2019**, *21*, 3742–3751.

[12] K. M. Enikeev, R. K. Mazitov, A. V. Il'yasov, E. N. Pyatova, *Bull. Acad. Sci. USSR Div. Chem. Sci.* **1988**, *37*, 1281.

[13] K. Bartik, M. Luhmer, S. J. Heyes, R. Ottinger, J. Reisse, *J. Magn. Reson. Ser. B* **1995**, *109*, 164–168.

[14] K. W. Miller, N. V. Reo, A. J. M. Schoot Uiterkamp, D. P. Stengle, T. R. Stengle, K. L. Williamson, *Proc. Natl. Acad. Sci. U. S. A.* **1981**, *78*, 4946–4949.

[15] P. Diehl, R. Ugolini, N. Suryaprakash, J. Jokisaari, *Magn. Reson. Chem.* **1991**, *29*, 1163–1164.

[16] T. R. Stengle, N. V. Reo, K. L. Williamson, *J. Phys. Chem.* **1981**, *85*, 3772–3775.

[17] M. Luhmer, K. Bartik, *J. Phys. Chem. A* **1997**, *101*, 5278–5283.

[18] C. J. Jameson, D. N. Sears, S. Murad, *J. Chem. Phys.* **2004**, *121*, 9581–9592.

[19] A. C. De Dios, C. J. Jameson, *J. Chem. Phys.* **1997**, *107*, 4253–4270.

[20] C. J. Jameson, D. N. Sears, A. C. De Dios, *J. Chem. Phys.* **2003**, *118*, 2575–2580.

[21] P. Morgado, J. Barras, E. J. M. Filipe, *Phys. Chem. Chem. Phys.* **2020**, *22*, 14736–14747.

[22] P. Peuravaara, J. Karjalainen, J. Zhu, J. Mareš, P. Lantto, J. Vaara, *Sci. Rep.* **2018**, *8*, 1–11.

[23] P. Diehl, J. Jokisaari, *J. Magn. Reson.* **1990**, *88*, 660–665.

[24] A. Moschos, J. Reisse, *J. Magn. Reson.* **1991**, *95*, 603–606.

[25] M. Luhmer, A. Moschos, J. Reisse, *J. Magn. Reson. Ser. A* **1995**, *113*, 164–168.

[26] K. Oikarinen, J. Jokisaari, *Appl. Magn. Reson.* **1995**, *8*, 587–595.

[27] I. E. Dimitrov, R. Reddy, J. S. Leigh, *J. Magn. Reson.* **2000**, *145*, 302–306.

[28] M. S. Albert, D. F. Kacher, D. Balamore, A. K. Venkatesh, F. A. Jolesz, *J. Magn. Reson.* **1999**, *140*, 264–273.

[29] M. S. Albert, D. Balamore, D. F. Kacher, A. K. Venkatesh, F. A. Jolesz, *NMR Biomed.* **2000**, *13*, 407–414.

[30] J. Wolber, A. Cherubini, M. O. Leach, A. Bifone, *NMR Biomed.* **2000**, *13*, 234–237.

[31] M. D. Gomes, P. Dao, K. Jeong, C. C. Slack, C. C. Vassiliou, J. A. Finbloom, M. B. Francis, D. E. Wemmer, A. Pines, *J. Am. Chem. Soc.* **2016**, *138*, 9747–9750.

[32] M. S. Syamala, R. J. Cross, M. Saunders, *J. Am. Chem. Soc.* **2002**, *124*, 6216–6219.

[33] H. J. C. Berendsen, D. van der Spoel, R. van Drunen, *Comput. Phys. Commun.* **1995**, *91*, 43–56.

[34] M. J. Abraham, T. Murtola, R. Schulz, S. Páll, J. C. Smith, B. Hess, E. Lindahl, *SoftwareX* **2015**, *1–2*, 19–25.

[35] L. Martínez, R. Andrade, E. G. Birgin, J. M. Martínez, *J. Comput. Chem.* **2009**, *30*, 2157–2164.

[36] H. J. C. Berendsen, J. P. M. Postma, W. F. van Gunsteren, A. DiNola, J. R. Haak, *J. Chem. Phys.* **1984**, *81*, 3684–3690.

[37] T. Darden, D. York, L. Pedersen, *J. Chem. Phys.* **1993**, *98*, 10089–10092.

[38] M. Parrinello, A. Rahman, *J. Appl. Phys.* **1981**, *52*, 7182–7190.

[39] S. Nosé, M. L. Klein, *Mol. Phys.* **1983**, *50*, 1055–1076.

[40] B. Hess, H. Bekker, H. J. C. Berendsen, J. G. E. M. Fraaije, *J. Comput. Chem.* **1997**, *18*, 1463–1472.

[41] W. L. Jorgensen, J. Tirado-Rives, *Proc. Natl. Acad. Sci.* **2005**, *102*, 6665–6670.

[42] L. S. Dodda, I. de Vaca, J. Tirado-Rives, W. L. Jorgensen, *Nucleic Acids Res.* **2017**, *45*, W331–W336.

[43] W. L. Jorgensen, D. S. Maxwell, J. Tirado-Rives, *J. Am. Chem. Soc.* **1996**, *118*, 11225–11236.

[44] N. Michaud-Agrawal, E. J. Denning, T. B. Woolf, O. Beckstein, *J. Comput. Chem.* **2011**, *32*, 2319–2327.

[45] R. J. Gowers, M. Linke, J. Barnoud, T. J. E. Reddy, M. N. Melo, S. L. Seyler, J. Domański, D. L. Dotson, S. Buchoux, I. M. Kenney, O. Beckstein, in *{P}roceedings 15th {P}ython {S}cience {C}onference* (Eds.: S. Benthall, S. Rostrup), **2016**, pp. 98–105.

[46] G. te Velde, F. M. Bickelhaupt, E. J. Baerends, C. F. Guerra, S. J. A. van Gisbergen, J. G. Snijders, T. Ziegler, *J. Comput. Chem.* **2001**, *22*, 931–967.

[47] G. Saielli, A. Bagno, F. Castiglione, R. Simonutti, M. Mauri, A. Mele, *J. Phys. Chem. B* **2014**, *118*, 13963–13968.

[48] M. Straka, P. Lantto, J. Vaara, *J. Phys. Chem. A* **2008**, *112*, 2658–2668.

[49] S. Grimme, J. Antony, S. Ehrlich, H. Krieg, *J. Chem. Phys.* **2010**, *132*, 154104.

[50] M. Boventi, V. Mazzilli, R. Simonutti, F. Castiglione, G. Saielli, *J. Mol. Liq.* **2023**, *382*, 122011.

[51] J. Wolber, S. J. Doran, M. O. Leach, A. Bifone, *Chem. Phys. Lett.* **1998**, *296*, 391–396.

[52] W. M. Haynes, *CRC Handbook of Chemistry and Physics, 95th Edition*, CRC Press, **2014**.

[53] C. L. Yaws, *Handbook of Viscosity*, **1995**.

[54] F. Castiglione, G. Saielli, M. Mauri, R. Simonutti, A. Mele, *J. Phys. Chem. B* **2020**, *124*, 6617–6627.

[55] V. Griffing, M. A. Cargyle, L. Corvese, D. Eby, *J. Phys. Chem.* **1954**, *58*, 1054–1056.

[56] S. Valkai, J. Liszi, I. Szalai, *J. Chem. Thermodyn.* **1998**, *30*, 825–832.

[57] A. Reddy, H. Nagar, B. Satyavathi, V. Aniya, *J. Mol. Liq.* **2020**, *306*, 112917.

[58] A. Bagno, G. Saielli, *Theor. Chem. Acc.* **2007**, *117*, 603–619.

[59] V. A. Semenov, L. B. Krivdin, *Russ. Chem. Rev.* **2022**, *91*, DOI 10.1070/rcr5027.

3. Exploring cavities in type II porous liquids with ^{129}Xe NMR

Parts of this Chapter have been published in

M. Boventi, M. Mauri, F. Alexander, S. L. James, R. Simonutti, F. Castiglione, *J. Mol. Liq.* **2023**, *370*, 121038.

The synthetic procedures were performed by Dr. Francesca Alexander, a former PhD student in the group of Prof. Stuart L. James from the School of Chemistry and Chemical Engineering at Queen's University, Belfast.

3.1 Introduction

Porous materials are central species in a huge variety of applications including, but not limited to, separation, energy storage, ion exchange, drug delivery, catalysis, and thermal and acoustic insulation.[1–7] The unique morphological properties of these materials can be fine-tuned via different rational synthetic strategies, making it possible to control the dimensions, shape, and connectivity of the pores along with the chemistry of their walls.[8,9] Moreover, the synthetic procedures can be tailored to obtain hierarchical structures with interconnected multimodal porosities, sometimes coupled with spatial organization over different length scales.[10] For these reasons, porous materials are nowadays living in a "golden age", with plentiful research works focused on their synthesis, characterization, and application.

Porosity has traditionally been associated solely with solid-state materials: their rigid and organized structure was thought to be essential to generating permanent free volume. Many of the most common porous materials, including for example zeolites, porous-aromatic frameworks (PAFs), covalent organic frameworks (COFs), hydrogen-

bonded organic frameworks (HOFs), and metal-organic frameworks (MOFs), are crystalline solids in which the existence of free volume is intertwined with structural rigidity. These features are opposite with respect to the structural organization of liquids, where the freedom and the constant motion of the molecular constituents allow them to fill the space with high efficiency. Naturally, not even liquids are able to fill the space completely without leaving even the smallest trace of free volume. It has been demonstrated that the high thermal motion leads to the formation of irregular and transient voids between the liquid molecules whose sizes are, on average, much smaller than the typical molecular dimensions.[11] The formation of these void spaces has been the subject of several theoretical studies with the aim of finding relationships between free volume and other physicochemical properties. For example, the scaled particle theory states that the solubility of a certain solute in a liquid is determined by the work needed to generate cavities of appropriate size.[12,13] This in turn also influences the transport properties of liquids. However, this extrinsic porosity of liquids is completely different from the well-defined, organized, and permanent free volume of porous crystalline materials.

In 2007, James and co-workers published a paper that conceptualized the possibility of creating porous liquids (PLs), that is, liquids with intrinsic and permanent porosity.[14] The authors proposed different approaches to create well-defined and permanent pores in the liquid state, such as the dissolution of macrocyclic molecules with structural cavities or the dispersion of porous framework materials in sterically hindered solvents, unable to occupy the pores. This neoteric class of materials remained purely theoretical for about a decade until three different examples of porous liquids were reported.

In 2014, a paper published by Del Pópolo et al. explored the possibility of functionalizing organic cages based on aromatic imines with alkyl chains to significantly reduce their melting points even up to about 40 °C, obtaining liquid materials very close to room temperature.[15] The authors reported a valid synthetic protocol for several alkyl chains with different lengths, obtaining a series of functionalized organic cages with melting points that decreased with the length of the chains. Molecular dynamics simulations revealed that long linear chains could enter the organic cages, compromising the permanent porosity of the liquids. On the other hand,

in the case of short alkyl side chains, the less conformational freedom made this process significantly more difficult, guaranteeing that around 30% of the cages were empty at any time. However, since liquids with short alkyl chains had high melting points, the authors could not conduct measurements of experimental parameters able to demonstrate the existence of permanent porosity, such as gas diffusion and solubility, and their analysis was limited to a computational approach.

In 2015, Dai and co-workers reported an alternative method to engineer permanent porosity into liquids.[16] Liquid materials were obtained by functionalizing solid hollow silica spheres with organosilane molecules containing ammonium groups and subsequently attaching sulfonated polyethylene glycol (PEG) chains via ionic bonds. Nitrogen sorption, transmission electron microscopy, and small-angle X-ray scattering measurements demonstrated the existence of permanent mesopores with diameters around 10 nm. The mesoporous liquid was also incorporated into a polymeric membrane to determine its effect on the gas permeability. The authors found that when the porous liquid was incorporated into the membrane, its permeability to CO_2 increased significantly compared to when PEG or other non-porous liquids were incorporated.

Lastly, another example of a porous liquid based on aromatic imine organic cages was reported by James et al. in 2015.[17] Solid macrocyclic organic cages were successfully prepared following a procedure similar to that proposed in the first example.[15] However, the synthetic protocol was adapted to obtain imine organic cages with six crown ether moieties on the outside. This peculiar design choice was made to enhance the solubility of the cages in 15-crown-5, a sterically hindered and bulky molecule. As predicted by molecular dynamics simulations, when the organic cages were dissolved in 15-crown-5 at 44% by weight, their cavities remained empty due to the high steric hindrance of the solvent molecules which made them incapable of occupying the cavities of the macrocyclic host. The existence of permanent pores in these solutions was confirmed experimentally by positron annihilation lifetime spectroscopy (PALS) measurements that, together with molecular modelling, indicated the presence of empty pores with diameters of about 0.5 nm. Moreover, the experimental solubility of methane in the porous liquid was 8 times higher than in pure 15-crown-5. In the same work, the authors proposed another PL based on similar macrocyclic hosts. The synthetic protocol was modified to obtain aromatic imine

organic cages with either dimethyl or cyclohexyl substituents randomly scrambled on the outside, instead of the bulky crown ether moieties. When dissolved in hexachloropropene, these hosts formed porous liquids with enhanced methane solubility compared to the pure solvent. Moreover, the authors demonstrated that xenon gas dissolved in the porous liquid was released when chloroform was added to the mixture, while the addition of the large 1-*t*-butyl-3,5-dimethylbenzene had no visible effect. This was attributed to the substitution of Xe atoms in the cavities with the small $CHCl_3$ molecules, whereas the benzene derivative could not be hosted in the cages due to the high steric hindrance.

Since these pioneering works, several different strategies to engineer intrinsic permanent porosity into liquids were proposed, along with examples of porous liquids with vastly different physicochemical properties.[18–29] Owing to this diversity, porous liquids are nowadays divided into four different categories. Type I PLs are pure and discrete molecular hosts in the liquid state. These molecules have cavities with shape and dimensions that prevent self-filling, guaranteeing the presence of intrinsic and well-defined pores.[15,24] Type II PLs are formed by dissolving porous host molecules in solvents that cannot enter the host cavities.[29–33] Type III porous liquids are constituted by porous framework materials dispersed in size-excluded solvents.[18,23,26,34] Lastly, the recently proposed type IV PLs are meltable porous framework materials that retain their intrinsic porosity in the liquid state.[27,28,35,36] The structure of the four types of porous liquids is represented schematically in Figure 3.1.[37]

Among the four categories, type I and type IV porous liquids (PLs) are the least common, primarily due to the significant challenges in their design and synthesis. So far, only a limited number of examples of type I PLs have been reported, mostly involving the functionalization of porous molecular hosts in order to reduce their melting points below room temperature.[15,16,25,38,39] Type IV PLs have the strict requirement of having to melt below their decomposition temperatures. As an example, frameworks based on metal nodes connected by imidazolate linkers have been found to satisfy this condition.[35] On the other hand, type II and type III PLs are generally easier to synthesize, more versatile, and more stable. As a result, numerous type II and III porous liquids have been developed in recent years, each exhibiting distinct chemical and physical properties.[18,20,21,23,25,26,31,32,40,41]

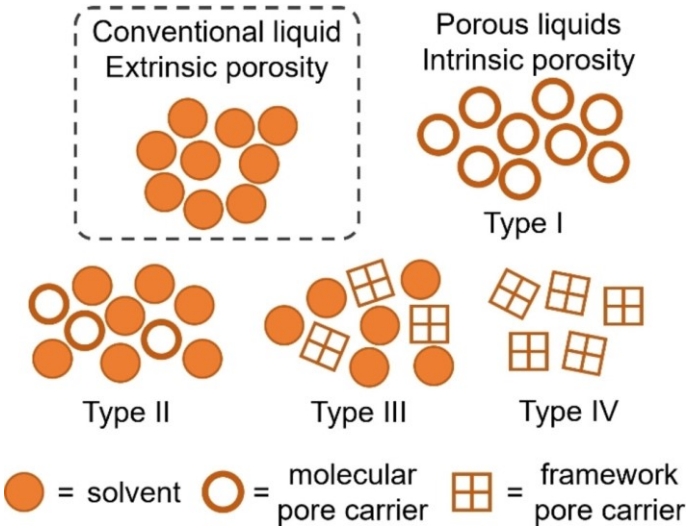

Figure 3.1. Schematic representation of conventional liquids and the four types of porous liquids. Reproduced from open access reference.[37]

The challenges associated with porous liquids lie not only in their preparation and in assuring their long-term stability but also in their characterization. The fluid nature of porous liquids complicates the use of traditional characterization techniques designed for porous solids. For example, nitrogen adsorption techniques are difficult to apply to these materials since the cryogenic conditions employed for the measurements may affect the liquid structure, potentially returning misleading results. Moreover, unequivocally proving the presence of an intrinsic porous structure and distinguishing it from the transient extrinsic pores formed in liquids is an arduous task for most characterization techniques. For these reasons, experimental techniques such as gas solubility measurements, nitrogen adsorption, positron annihilation lifetime spectroscopy, and electron microscopy must be applied carefully to ensure that the structure of porous liquids is unaltered. The development of novel characterization techniques to study the porous topology and, possibly, the structural organization of PLs constitutes an interesting research line for years to come.[42]

The reported applications of porous liquids take advantage of the combination of permanent porosity and flowability. These materials can find use in catalysis, membranes, chiral separation processes, and as electrolytes or heat transfer fluids.[42,43] However, the most important applications of porous liquids are related to gas sorption.

Several studies highlight the possibility of using these materials for gas capture,[25,32,44] storage,[21] and separation.[26,33,45] Similarly to conventional porous solid materials, the porous topology of PLs can be finely tuned via a rational structural design to enhance their selectivity towards specific gas molecules, allowing to selectively capture only targeted species and greatly improving the gas separation performances.[23,27,41,46] Indeed, the sorption and separation capabilities of PLs are highly dependent on the shape, dimensions, and chemistry of the permanent cages, as well as the mechanism of gas sorption and confinement. In this view, a detailed understanding of the sorption and solvation properties of dissolved species will significantly help in the design and optimization of porous liquids for gas sorption applications.

Given all these premises, the non-invasive and non-destructive ^{129}Xe NMR technique can be a very powerful tool in the field of porous liquids. Indeed, this technique has been applied in the past not only to pure liquids and mixtures, as described thoroughly in Chapter 2, but also to solutions of supramolecular hosts in organic solvents,[47–50] with the aim of studying their structure and the accessibility of their inner cavities. ^{129}Xe NMR is potentially able to probe simultaneously both the porous topology of PLs and their structural organization. The only requirement is that the intrinsic cavities are bigger than xenon atoms, which is almost always the case since Xe has a van der Waals diameter of about 4.4 Å.

A couple of examples of the use of ^{129}Xe NMR to characterize porous liquids have already been reported in the literature. Cooper et al. employed this technique to characterize the permanent pores in solutions of imine organic cages with random cyclohexyl/dimethyl substituents on the outside,[46] similar to those reported in 2015.[17] They observed significant chemical shift differences between xenon dissolved in the pure solvent, hexachloropropene, and in 20% w/v solutions of the macrocyclic hosts. Some years later, an analogous approach to porous liquids based on the same core organic cages but with different scrambled substituents was reported.[41]

This Chapter aims to strengthen the knowledge of the use of ^{129}Xe NMR in the study of porous liquids and to show how this technique can overcome some of the most challenging aspects in the characterization of these novel materials. We employed ^{129}Xe NMR to study the porous topology of a series of neoteric type II porous liquids based on Noria-OEt, a derivative of the well-known paddlewheel-like Noria molecule, whose

structure is represented in Figure 3.2. The successful preparation of these porous liquids was reported by James and co-workers in 2021.[51] Noria-OEt was synthesized by adapting the standard synthetic procedure of Noria, that is, the condensation reaction between resorcinol and 1,5-pentanedial.[52] Substituting resorcinol with 3-ethoxyphenol allows obtaining the Noria-OEt derivative instead of Noria.[53,54] This molecule which has 12 ethyl substituents scrambled over the 24 oxygen atoms on the outside of the paddlewheel-like structure (see Figure 3.2). This enhances the solubility of the macrocyclic host in the crown ether 15-crown-5, which was chosen as the bulky solvent for the formation of chemically and thermally stable type II PLs. The existence of permanent pores was demonstrated with molecular dynamics simulations and methane solubility measurements. Here, we decided to give a complete overview of the structural organization of these materials using ^{129}Xe NMR. This technique is particularly suitable for these novel porous liquids since, as reported in the literature, the cavity of solid Noria is both shape and size-selective for a single xenon atom.[55]

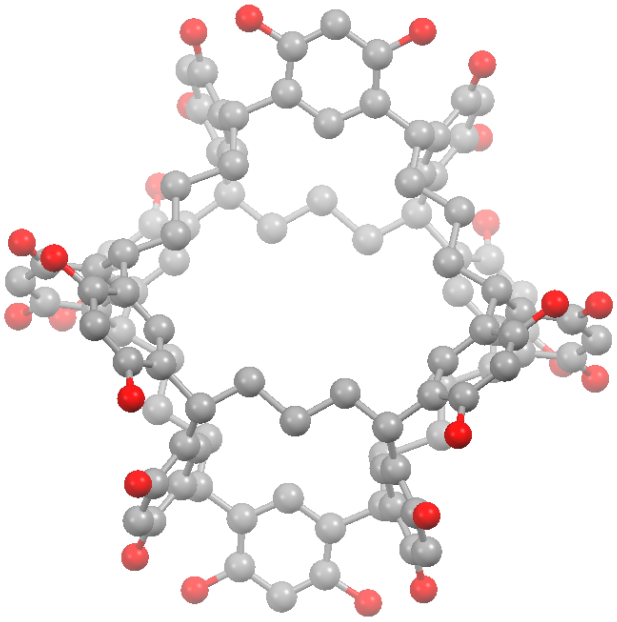

Figure 3.2. Structure of the Noria molecule with carbon atoms in grey and oxygen atoms in red. Hydrogens are omitted for clarity.

3.2 Experimental section

3.2.1 Synthesis of Noria-OEt and preparation of type II PLs

Noria-OEt was synthesized as described previously by the condensation reaction of 3-ethoxyphenol and 1,5-pentanedial under acidic conditions.[51] Compared to the non-functionalized Noria molecule, represented in Figure 3.2, Noria-OEt has 12 ethyl groups randomly distributed among the 24 different possible oxygen sites. This enhances the solubility of the paddlewheel-like structure in the bulky, size-excluded 15-crown-5 up to 80 mg/mL.

A series of type II porous liquids was prepared by dissolving Noria-OEt in dry 15-crown-5 at different concentrations and sonicating at room temperature until clear amber solutions were formed. The concentrations of the obtained type II porous liquids are shown in Table 3.1. Notably, the 80 mg/mL porous liquid was also prepared, but its high viscosity caused extreme peak broadening in the ^{129}Xe NMR spectra. For this reason, the sample was not further analyzed, and the associated results were not reported.

Table 3.1. Characteristics of the Noria-OEt-15-crown-5 type II porous liquids. The concentration of cages was calculated considering a molar mass of 2042.48 g/mol for Noria-OEt.

$C_{\text{Noria-OEt}}$ [mg/mL]	$C_{\text{Noria-OEt}}$ [mM]	Molar ratio Noria-OEt:15-crown-5
11	5.43	1:930
28	13.7	1:369
40	19.6	1:258
50	24.5	1:206
60	29.4	1:172
70	34.3	1:147

3.2.2 Sample preparation

About 0.3 mL of the clear amber type II porous liquid was inserted into a medium-wall NMR tube (Norell® Select Series with 5 mm outer diameter and 3.46 mm inner

diameter), along with a short capillary tube containing 80-100 μL of DMSO-d_6. The tube was connected to a Schlenk line, and the liquid was degassed under a dynamic vacuum (6.0×10^{-2} torr) with freeze-pump-thaw, taking great care to avoid the evaporation of 15-crown-5. Several cycles were performed until no gas bubbles were observed inside the sample. Xenon gas was inserted into a portion of the Schlenk line with known volume, and its amount was determined by measuring the pressure with an inline pressure gauge. From this portion, the gas was transferred into the NMR tube and trapped inside by freezing with liquid nitrogen. Then, the NMR tube was flame-sealed while keeping the xenon gas frozen. The sealed tubes were left to equilibrate for at least 24 hours prior to the measurements. Two additional reference samples were prepared, one containing 15-crown-5 and the other with solid Noria-OEt. The first one was prepared following the same procedures of type II porous liquids. The solid Noria-OEt sample was prepared similarly but the sample was degassed by leaving the tube under vacuum for six hours. For all the samples, the nominal xenon pressure was in the range of 3-4 bar.

3.2.3 NMR Spectroscopy

One-dimensional ^{129}Xe NMR and spin-lattice relaxation time (T_1) measurements were carried out using a Bruker Avance 500 spectrometer operating at a Larmor frequency of 500.13 MHz for ^{1}H and 139.09 MHz for ^{129}Xe, equipped with a double resonance broadband observe (BBO) probe. The recycle delay for one-dimensional spectra was set to 150 s, and the number of scans was in the range of 8-512 to obtain good signal-to-noise ratios. Spectra were acquired at 298 K for all samples. The samples containing pure 15-crown-5 and Noria-OEt type II porous liquids at concentrations of 11 mg/mL and 60 mg/mL were also analyzed every 10 K in a temperature range between 268 K and 318 K. ^{129}Xe chemical shifts were referenced by setting the signal of xenon dissolved in benzene at 298 K to 188.1 ppm.[56] T_1 measurements were performed at 300 K using the Inversion Recovery pulse sequence, indicated as t1ir in the Bruker pulse sequence libraries. 12 delay increments were recorded with 8-32 scans each and a long relaxation delay in the range of 200-400 s to ensure the complete relaxation of xenon nuclei. The temperature was controlled within 0.1 K with a Bruker BVT3000 variable temperature unit using airflow. For low-temperature experiments, a liquid nitrogen

evaporator was connected to the NMR probe and controlled with the same variable temperature unit.

Diffusion NMR experiments were performed on a Bruker Avance Neo 500 spectrometer equipped with a direct observe broadband including fluorine (BBFO) iProbe. The resonant frequencies of ^{1}H and ^{129}Xe were 500.13 MHz and 139.09 MHz, respectively. A stimulated-echo pulse sequence with gradient pulse duration, δ, between 5-6 ms and a diffusion delay, Δ, between 200-600 ms was employed. The gradient pulse strength was incremented from 2% to 95% of the maximum strength in a linear ramp with 16-22 steps. For each increment, 8-16 scans were accumulated, and the relaxation delay was set to 50 s. The temperature was set to 298 K and controlled with airflow using a BVT3000 variable temperature unit.

3.3 Results and discussion

3.3.1 ^{129}Xe NMR at 298 K

The stacked ^{129}Xe NMR spectra for all the samples acquired at 298 K are shown in Figure 3.3, while the chemical shifts of the peaks are reported in Table 3.2.

The spectrum of xenon dissolved in pure 15-crown-5, shown in Figure 3.3a, shows a single sharp resonance at 202.97 ppm. This chemical shift value is significantly higher compared to that of xenon dissolved in several common organic solvents,[57] linear and branched alkanes,[58,59] and even nitrogen- or oxygen-substituted aliphatic compounds.[60] This suggests the presence of a strong interaction between xenon and crown ether molecules. Such an interaction may arise from the formation of complexes between xenon and crown ether molecules, similar to those formed by alkali metal cations with crown ethers. Indeed, a strong deshielding effect on ^{129}Xe dissolved in crown ether solutions has already been reported by Reisse and co-workers.[61] They observed significant chemical shift differences between xenon dissolved in crown ether- and linear ether-chloroform solutions. These differences were explained by the formation of a loosely bound xenon-crown ether complex. Specifically, they classified 12-crown-4 and 15-crown-5 as host molecules for xenon, demonstrating that, thanks to the compatible size of their internal cavities, they can form xenon-ether complexes

through selective interactions. Moreover, the formation of a stable solid-state complex between xenon and 15-crown-5 has been recently reported.[62] This further demonstrates that crown ethers can form 1:1 complexes with Xe.

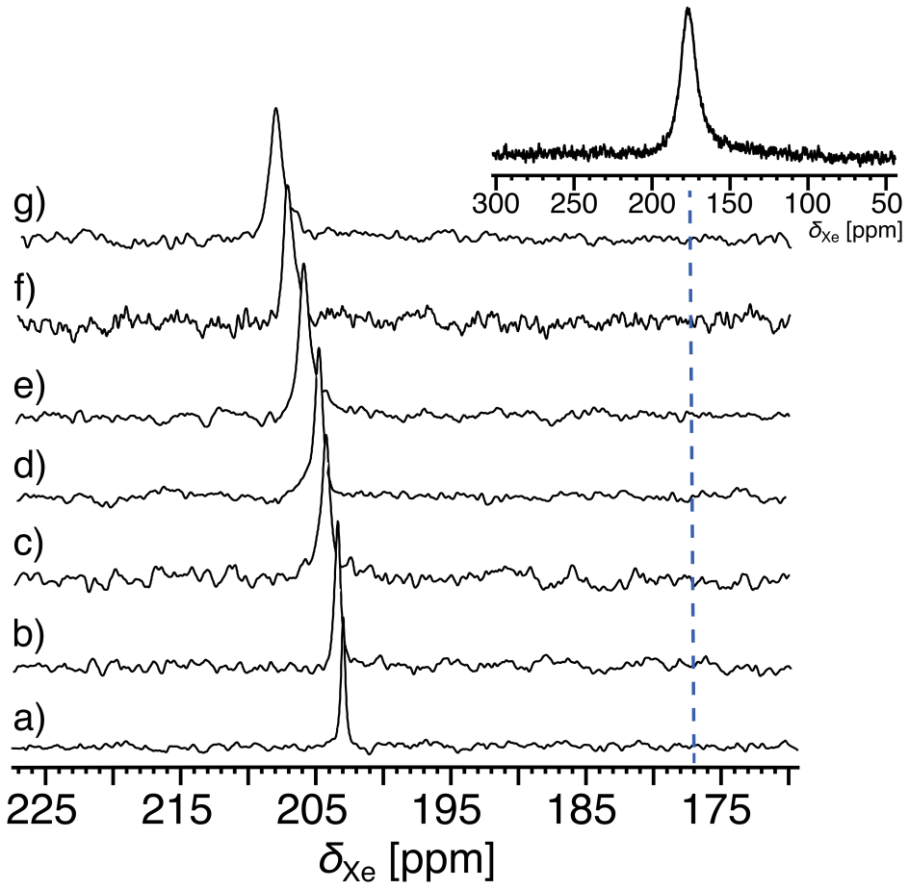

Figure 3.3. ^{129}Xe NMR spectra acquired at 298 K of xenon dissolved in type II porous liquids with increasing Noria-OEt concentration: a) pure 15-crown-5, b) 11 mg/mL, c) 28 mg/mL, d) 40 mg/mL, e) 50 mg/mL, f) 60 mg/mL, g) 70 mg/mL. The inset shows the spectrum of xenon loaded into solid Noria-OEt.

The room temperature spectra of xenon loaded into type II porous liquids with varying Noria-OEt concentrations are displayed in Figure 3.3b-g. Each spectrum shows a single, intense peak, similar to those of xenon dissolved in conventional liquids. As can be seen in Table 3.2, the xenon chemical shift is sensitive to changes in Noria-OEt concentration: increasing the concentration from 11 mg/mL (Figure 3.3b) to 70 mg/mL (Figure 3.3g) results in a chemical shift increase of approximately 3 ppm. Interestingly, the signal of xenon in pure 15-crown-5 follows the same trend, showing the lowest chemical shift among all the liquids. This behavior is clearly visible in Figure 3.4,

where the chemical shift of dissolved xenon is represented as a function of Noria-OEt concentration.

Table 3.2. Chemical shifts of xenon in type II porous liquids, pure 15-crown-5, and solid Noria-OEt measured at 298 K.

$C_{\text{Noria-OEt}}$ [mg/mL]	δ_{Xe} [ppm]
/*	177
0**	202.97
11	203.26
28	204.24
40	204.56
50	205.73
60	206.16
70	206.56

**Solid Noria-OEt. **Pure 15-crown-5.*

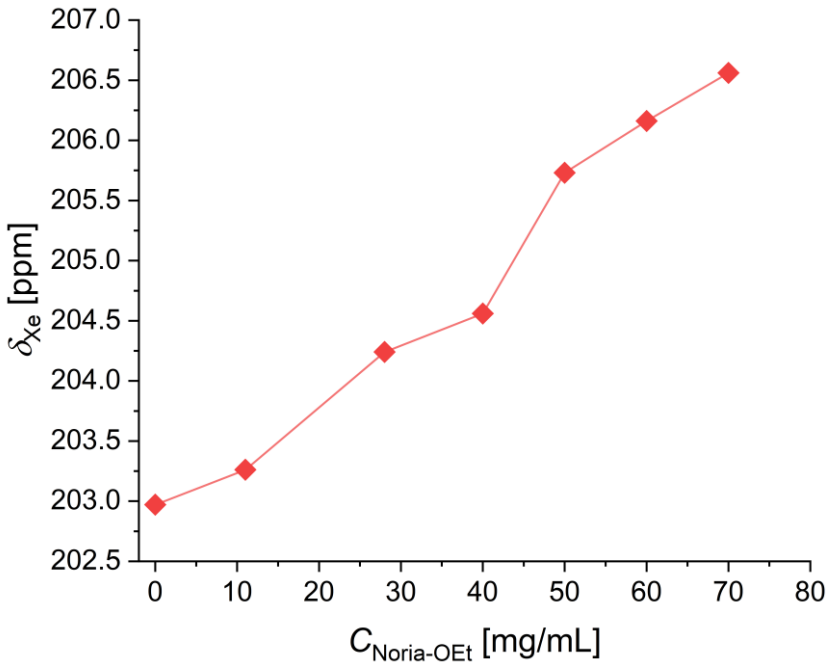

Figure 3.4. ^{129}Xe chemical shift of xenon dissolved into type II porous liquids at 298 K as a function of the Noria-OEt concentration. Zero concentration refers to pure 15-crown-5. The lines are only a guide to the eye.

To interpret the Xe@PL signal, it's important to note that ^{129}Xe NMR is a dynamic technique. When xenon atoms move quickly between different environments on the NMR timescale, the observed chemical shift is an average of the chemical shifts in the different sites, weighted by the respective xenon molar fractions. Separate signals only appear if the xenon exchange between different sites is slow on the NMR timescale. Since Noria is known to selectively interact with xenon,[55] we can infer that, at 298 K, xenon interacts with both Noria-OEt and 15-crown-5 on the NMR timescale, producing an averaged or exchange signal. Similar behavior has already been observed for xenon in solutions of α-cyclodextrin, where the NMR signals resulted from an average of xenon atoms probing the inside and the outside of the cavity.[47]

To better understand the origin of the xenon signals in the porous liquids, we acquired a spectrum of xenon in solid crystalline Noria-OEt at 298 K. The result, shown in the inset of Figure 3.3, reveals a single broad resonance centered around 177 ppm. This high chemical shift falls within the typical range for xenon confined in microporous solids.[63–65] To obtain a rough estimate of the size of these pores, we applied the model originally proposed by Demarquay and Fraissard (see Section 1.4.3.1).[66] Indeed, even if this model was originally proposed only for microporous zeolites, it has been successfully applied to obtain estimates of the pore dimensions of a wide variety of microporous solids.[67–70] According to the model, when strong adsorption sites (such as highly charged cations) and paramagnetic species are absent, and Xe-Xe interactions are negligible, the chemical shift of confined xenon is related to its mean free path, Γ, by the following relationship.

$$\delta_{Xe} = 243\left(\frac{2.054}{2.054+\Gamma}\right) \tag{3.1}$$

In the two limiting cases of spherical and cylindrical pores, the mean free path can be used to calculate the pore diameter with the following equations, where D_c and D_s are the diameters of cylindrical and spherical pores, respectively, and $D_{Xe} = 4.4$ Å is the van der Waals diameter of xenon.

$$D_c = \Gamma + D_{Xe} \tag{3.2}$$

$$D_s = 2\Gamma + D_{Xe} \tag{3.3}$$

By inserting the value δ_{Xe} = 177 ppm in Equation (3.1), a mean free path of 0.77 Å is obtained, which leads to very similar cylindrical and spherical pore diameters of 5.2 Å and 5.9 Å, respectively. These dimensions are in good agreement with previous reports on the crystal structure of non-ethylated Noria which indicate that the central cavity has a diameter in the range of 5-7 Å. Despite the approximations derived from the model, these results indicate that the cavities of Noria and Noria-OEt have roughly the same dimensions, demonstrating that the 12 ethyl groups scrambled on the possible 24 oxygen sites have a very small effect on the size of the cavity.

The broadness of the xenon signal can be attributed to xenon diffusing through solid particles with varying orientations relative to the external magnetic field, as well as the presence of multiple species with very similar cavity sizes. Indeed, James and co-workers have shown that the typical synthesis of Noria produces a mixture of various oligomers, primarily Noria itself and a structural isomer, the resorcinarene trimer (R3), which have slightly different central cavity sizes. It is therefore highly likely that the synthesis of Noria-OEt also yields the ethylated resorcinarene trimer (R3-OEt) along with other oligomers, similar to the standard synthesis of Noria.[51] Additionally, even considering just the Noria-OEt molecule, there are 64 potential geometric isomers due to the various possible distributions of the 12 ethyl groups on the outer oxygen atoms. All these species are expected to have cavities with only slightly different sizes. The broad signal of ^{129}Xe inside bulk Noria-OEt, spanning approximately from 160 ppm to 190 ppm, suggests that xenon is not confined to a single microporous species but instead explores a somewhat wider range of micropores, estimated to range roughly from 5 to 7 Å based on the previous equations.

The comparison of the xenon chemical shifts in solid Noria-OEt, pure 15-crown-5, and type II porous liquids reveals key insight into the structural characteristics of the latter. Interestingly, the chemical shift of xenon in solid Noria-OEt, around 177 ppm, is much lower than that of the reference 15-crown-5 sample at 202.97 ppm. According to a simple two-site model for the type II PLs, where xenon is assumed to interact with both Noria-OEt and 15-crown-5 molecules on the NMR timescale, the chemical shift would reflect an average of the chemical shifts of xenon in the two species, weighted by the respective molar fractions (see Section 1.4.2.1). In this scenario, the Xe@PL chemical shift would be expected to fall between the two limiting values of 177 ppm and 202.97

ppm and to decrease with higher host concentration, as the Xe@Noria-OEt molar fraction increases with Noria-OEt concentration. However, the observed chemical shifts of xenon dissolved in type II porous liquids exceed those of pure 15-crown-5 and rise with increasing host concentration, contradicting the predictions of a two-site model. This suggests that this model is overly simplistic for the system, and it does not accurately represent its structure.

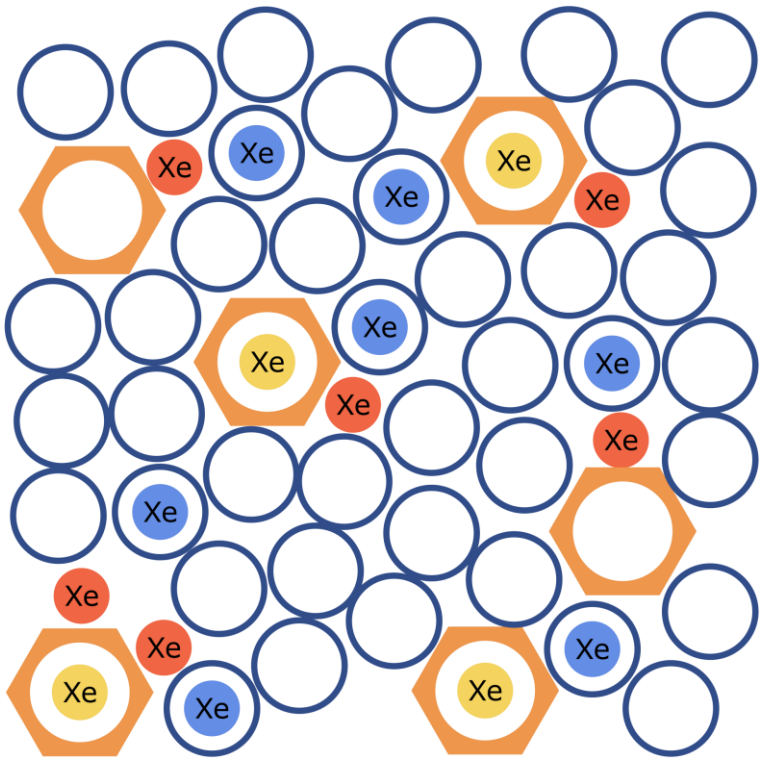

Figure 3.5. Sketch of the three-site model for xenon dissolved in type II porous liquids. Orange polygons represent Noria-OEt molecules, while blue circles represent 15-crown-5.

The experimental data can be explained in the framework of a three-site model sketched in Figure 3.5.[47,71,72] Specifically, in addition to occupying the cavities of the host and the solvent, xenon can also reside near the outer surface of Noria-OEt molecules, where it interacts with their structural indentations. The presence of structural indentations in type II porous liquids with Noria-OEt and 15-crown-5 has been demonstrated by James et al. in their original work.[51] By performing molecular dynamics (MD) simulations on the porous liquid with $C_{\text{Noria-OEt}}$ = 50 mg/mL, corresponding to a host:solvent molar ratio of 1:206 (see Table 3.1), they were able to

calculate the host-solvent radial distribution functions. These showed two distinct maxima, corresponding to two solvation shells, at 0.72 nm and 1.08 nm from the center of the Noria-OEt molecule. The maximum at 0.72 nm corresponds to the six lateral indentations of the Noria-OEt molecular paddlewheel, which are also visible in the structure of the non-ethylated analog shown in Figure 3.2. On the other hand, the maximum at 1.08 nm represents the solvation shell located on the outer effective radius of the molecule.

All these results indicate that the observed ^{129}Xe chemical shifts result from an average of the chemical shifts of xenon exploring three different sites, weighted by the respective molar fractions: xenon in the inner cavity of Noria-OEt, xenon in the structural indentations of Noria-OEt, and xenon in the inner cavity of 15-crown-5. Notably, the measured chemical shifts are very close to that of pure 15-crown-5 because the molar fraction of xenon in this species is predominant, as expected due to the molar ratios indicated in Table 3.1. While the chemical shifts of xenon in the host and solvent inner cavities were determined indirectly, we could not measure experimentally the chemical shift of xenon in the six outer cavities of Noria-OEt. It is clear from the structure that these cavities are rich in oxygen atoms, as opposed to the hydrophobic central cavity exposed only to carbon and hydrogen atoms. Due to the close contact interactions between xenon and oxygen, we can expect the chemical shift of xenon in the structural indentations to be significantly higher than that of xenon in the inner cavity. Indeed, the reported chemical shifts of xenon dissolved in oxygen-substituted aliphatic compounds are consistently higher compared to xenon dissolved in non-substituted analogs.[57,58,60] We note, however, that this is only a tentative explanation and that more insight into the chemical shift of xenon in the six outer cavities could be gained by performing in-depth molecular dynamics simulations and density functional theory calculations, following a similar approach to that presented in Chapter 2.

3.3.2 Variable temperature ^{129}Xe NMR

To further investigate the porous topology of these systems, we performed variable temperature ^{129}Xe NMR experiments on 15-crown-5 and type II porous liquids with Noria-OEt concentrations equal to 11 mg/mL and 60 mg/mL, in the range between 268 K and 318 K. We chose these two porous liquids to have the highest possible difference

in the host concentration while maintaining a good signal-to-noise ratio even at high temperature. Indeed, the high viscosity of the 70 mg/mL sample caused a significant peak broadening, and a high number of scans was required to obtain a good signal-to-noise ratio, especially above room temperature.

All the spectra showed single peaks similar to those observed at room temperature, indicating that it is not possible to reach a temperature at which the signals of xenon in the three different sites are separated before freezing the porous liquids. The variable temperature ^{129}Xe chemical shifts are shown in Figure 3.6. Note that we could not represent the data as a function of the reduced temperature, which is a better representation to compare samples in the same thermodynamic state (see Section 2.3.1),[59,73] because the critical temperature of the porous liquids was not known.

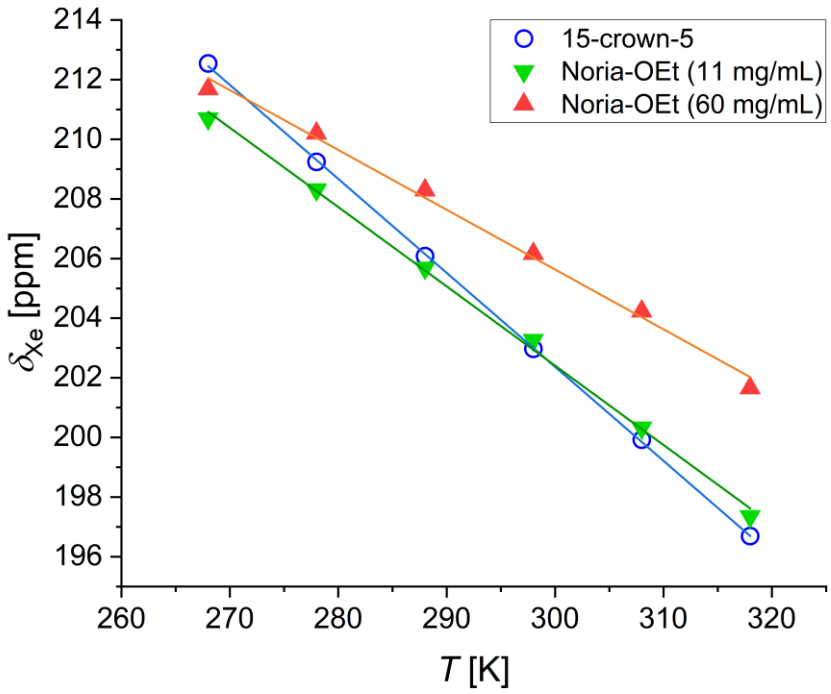

Figure 3.6. ^{129}Xe chemical shifts of xenon dissolved in pure 15-crown-5 and selected Noria-OEt type II porous liquids as a function of temperature. The lines are fits to linear functions.

For all three samples, the chemical shift clearly shows a linear dependence on temperature in the whole analyzed temperature range. For 15-crown-5, fitting the data to a linear function returns a temperature dependence of -0.32 ppm/K, with an estimated relative uncertainty of ±5%. This value is similar to the typical chemical shift-

temperature dependence for xenon dissolved in organic solvents which is around -0.3 ppm/K.[59,74] Interestingly, in the case of porous liquids, not only the chemical shift is responsive to the host concentration, as already discussed, but also its temperature dependence. Specifically, increasing the Noria-OEt concentration causes the chemical shift of dissolved xenon to be less sensitive to temperature: -0.25 ppm/K for 11 mg/mL and -0.18 ppm/K for 60 mg/mL. This behavior can be explained by the molecular dynamics calculations from Jameson and co-workers,[74] which show that, in the absence of specific interactions, the primary factor influencing the chemical shift variation with temperature is the change in the volume of the dynamic cage available to the xenon atom. Larger changes in free volume result in more significant chemical shift variations with temperature, as seen in pure 15-crown-5, a highly flexible molecule with a slope of -0.32 ppm/K. In contrast, for the porous liquids, there are two additional sites, inside the central cavity and in the six surface indentations, that experience minimal dimensional changes as the temperature varies due to the high rigidity of the Noria-OEt molecule.

3.3.3 Xenon relaxation and diffusion

Due to the high sensitivity of the spin-lattice relaxation time (T_1) of xenon to its surrounding environment, this NMR parameter can constitute an additional source of information on the structure of simple isotropic liquids or even complex ionic liquids.[75,76] As demonstrated by the pioneering works on the spin-lattice relaxation of xenon dissolved in liquids, the primary contributor to this process in the temperature range of 298-323 K is the ^{129}Xe-^{1}H dipolar coupling. Since the cavity of Noria-OEt is densely populated with hydrogen atoms, as can be seen in Figure 3.2, we decided to measure the spin-lattice relaxation times of xenon dissolved in the porous liquids to gain more insight into their structural organization and their porous topology.

The T_1 relaxation times for xenon dissolved in type II PLs, measured at 300 K, are represented in Figure 3.7 as a function of the Noria-OEt concentration. These values were obtained by fitting the data from the Inversion Recovery pulse sequence to a single exponential function, confirming that xenon experiences a single average environment on the NMR timescale. The determined spin-lattice relaxation times are significantly lower than those of xenon dissolved in various alkanes and in benzene, which

approximately lie in the range of 170-270 s.[75,77,78] Notably, the T_1 values vary with host concentration, decreasing from 32 s for pure 15-crown-5 to 22.1 s for the PL with 60 mg/mL Noria-OEt. Unlike the chemical shift, the relaxation times decrease with increasing host concentration. As discussed in Section 1.2.3.1, dipolar relaxation is generated by the modulation of the dipolar interaction given by molecular motion. Assuming that molecular motion is similar across all samples with different Noria-OEt concentrations, the results indicate that the overall strength of the dipolar coupling between xenon and hydrogen increases as the Noria-OEt concentration rises. This suggests that xenon interacts strongly with the hydrogen atoms of Noria-OEt, which is consistent with the proximity of many H atoms to the central cavity of the host molecule, represented in Figure 3.2. Thus, these results constitute additional evidence of the existence of significant interactions between xenon and Noria-OEt.

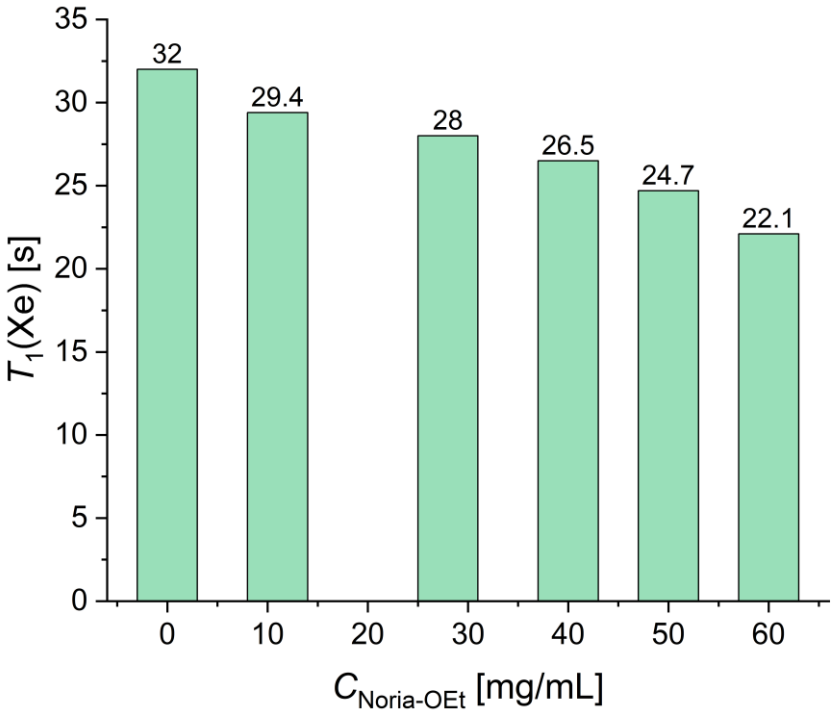

Figure 3.7. ^{129}Xe spin-lattice relaxation times of xenon dissolved in type II porous liquids as a function of Noria-OEt concentration. Zero concentration refers to pure 15-crown-5. All the measurements were carried out at 300 K.

As an additional characterization of the structure of type II porous liquids, we used pulsed field gradient NMR to measure the diffusion coefficients of xenon in pure

15-crown-5 and the porous liquid with 11 mg/mL Noria-OEt. The attempts to measure the diffusion coefficient of xenon in the other porous liquids were unsuccessful. This was probably due to the high viscosity of all but the most diluted porous liquid. This not only caused an increase in the linewidth of the xenon peak with increasing Noria-OEt concentration (see Figure 3.3) but also slowed down the xenon diffusion up to a point where it was not possible to obtain reliable data even when using short diffusion delays, which is usually needed when the diffusion coefficient is in the order of 10^{-10} m^2/s.

The diffusion coefficients of xenon in 15-crown-5 and the porous liquid with 11 mg/mL Noria-OEt were found to be equal at 2.15×10^{-10} m^2/s. For context, this value is several orders of magnitude smaller than that of free Xe gas, 5.3×10^{-6} m^2/s,[79] and about one order of magnitude smaller than xenon dissolved in water (2.2×10^{-9} m^2/s)[80] or in several alkanes.[75] In our case, the diffusion of xenon seems to be unchanged by the presence of Noria-OEt as its features seem to be mostly if not completely, determined by the characteristics of the bulk solvent. This is reasonable considering that the host:solvent molar ratio is 1:930 (see Table 3.1) and, thus, the amount of xenon interacting with Noria-OEt compared to 15-crown-5 is much lower. Notably, this suggests that the solvent and the most diluted type II porous liquid have the same transport properties. This feature could be interesting in applications where both enhanced gas sorption and very high fluidity are required.

3.4 Conclusions

In this Chapter, for the first time, we report the application of ^{129}Xe NMR techniques to the characterization of the porous structure of novel type II porous liquids based on Noria-OEt, an ethylated derivative of the molecular paddlewheel Noria, and 15-crown-5 as the bulky, size-excluded solvent.

The analysis of the room temperature xenon chemical shifts in pure 15-crown-5, solid Noria-OEt, and type II porous liquids with increasing concentrations of Noria-OEt reveals that a simple two-site model with xenon exploring both the cavities of the solvent and the host is too naïve to describe the porous topology of the PLs. The porous structure of these peculiar materials is instead well-described by a three-site model which comprises xenon exploring the six structural indentations on the outside of the

Noria-OEt molecule. These findings are also supported by variable temperature ^{129}Xe NMR measurements which indicate a smaller variation of the free volume with temperature with increasing the Noria-OEt concentration, compatible with the structural rigidity of this molecule compared to 15-crown-5.

Spin-lattice relaxation times of xenon are also responsive to the composition of the porous liquids since they decrease with increasing the host concentration. This indicates that the overall strength of the ^{129}Xe-^{1}H dipolar coupling, the predominant relaxation mechanism for xenon dissolved in liquids, increases with the amount of Noria-OEt. This indicates that xenon atoms interact strongly with the host molecules, which is consistent with xenon included within the hydrophobic central cavity and interacting with the hydrogen atoms located on the walls.

Pulsed field gradient NMR measurements performed for both pure 15-crown-5 and the most diluted porous liquid reveal that the diffusion coefficient of xenon in these liquids is the same. Interestingly, this indicates that observed that the formation of a diluted Noria-OEt-15-crown-5 porous liquid does not change the diffusional features of xenon within the bulk solvent. This peculiar property could be useful for applications in which a very high fluidity is required along with an enhanced gas sorption given by the intrinsic porosity. Measurements on even the second most diluted porous liquid could not be performed, probably due to the high viscosity of the sample.

Overall, our findings further demonstrate that by dissolving Noria-OEt in the size-excluded solvent 15-crown-5, liquids with intrinsic porosities are obtained. However, due to the peculiar shape of the Noria-OEt molecular paddlewheel, the obtained materials also display extrinsic porosity, which is instead typical of conventional liquids. More specifically, the six lateral indentations of the Noria-OEt molecule create additional, extrinsic pores that can be explored by small molecular or atomic species like Xe. Even if this does not prevent the formation of intrinsic porosity, this feature has important consequences on the properties of the porous liquids. For example, the selectivity towards certain species, which is of the utmost importance in gas capture and separation, could be lowered by the presence of extrinsic porosity since the central cavity is no longer the only accessible site.

In conclusion, this work paves the way for the use of ^{129}Xe NMR spectroscopy for the in-depth characterization of the porous structure of novel porous liquids. The ability

of this technique to simultaneously probe the liquid structure and the cavities is extremely valuable when analyzing materials where the porous structure is imbued in a liquid matrix. Moreover, our findings regarding the creation of extrinsic pores due to the shape of the Noria-OEt molecule build on the body of knowledge regarding type II porous liquids, potentially aiding in the design of materials with high performances in terms of gas selectivity and separation.

3.5 Bibliography

[1] N. P. Brandon, D. J. Brett, *Philos. Trans. R. Soc. A Math. Phys. Eng. Sci.* **2006**, *364*, 147–159.

[2] M. Arruebo, *Wiley Interdiscip. Rev. Nanomedicine Nanobiotechnology* **2012**, *4*, 16–30.

[3] C. M. A. Parlett, K. Wilson, A. F. Lee, *Chem. Soc. Rev.* **2013**, *42*, 3876–3893.

[4] D. J. Wales, J. Grand, V. P. Ting, R. D. Burke, K. J. Edler, C. R. Bowen, S. Mintova, A. D. Burrows, *Chem. Soc. Rev.* **2015**, *44*, 4290–4321.

[5] S. Rashidi, J. A. Esfahani, A. Rashidi, *Renew. Sustain. Energy Rev.* **2017**, *73*, 1198–1210.

[6] H. Cheng, L. Lijie, B. Wang, X. Feng, Z. Mao, G. J. Vancso, X. Sui, *Prog. Polym. Sci.* **2020**, *106*, 101253.

[7] A. Gharehghani, K. Ghasemi, M. Siavashi, S. Mehranfar, *Fuel* **2021**, *304*, 121411.

[8] M. E. Davis, *Nature* **2002**, *417*, 813–821.

[9] A. G. Slater, A. I. Cooper, *Science (80-.).* **2015**, *348*, aaa8075.

[10] X. Y. Yang, L. H. Chen, Y. Li, J. C. Rooke, C. Sanchez, B. L. Su, *Chem. Soc. Rev.* **2017**, *46*, 481–558.

[11] A. Pohorille, L. R. Pratt, *J. Am. Chem. Soc.* **1990**, *112*, 5066–5074.

[12] R. A. Pierotti, *J. Phys. Chem.* **1963**, *67*, 1840–1845.

[13] R. A. Pierotti, *Chem. Rev.* **1976**, *76*, 717–726.

[14] N. O'Reilly, N. Giri, S. L. James, *Chem. - A Eur. J.* **2007**, *13*, 3020–3025.

[15] G. Melaugh, N. Giri, C. E. Davidson, S. L. James, M. G. Del Pópolo, *Phys. Chem. Chem. Phys.* **2014**, *16*, 9422–9431.

[16] J. Zhang, S. H. Chai, Z. A. Qiao, S. M. Mahurin, J. Chen, Y. Fang, S. Wan, K. Nelson, P. Zhang, S. Dai, *Angew. Chemie - Int. Ed.* **2015**, *54*, 932–936.

[17] N. Giri, M. G. Del Pópolo, G. Melaugh, R. L. Greenaway, K. Rätzke, T. Koschine, L. Pison, M. F. C. Gomes, A. I. Cooper, S. L. James, *Nature* **2015**, *527*, 216–220.

[18] W. Shan, P. F. Fulvio, L. Kong, J. A. Schott, C. L. Do-Thanh, T. Tian, X. Hu, S. M. Mahurin, H. Xing, S. Dai, *ACS Appl. Mater. Interfaces* **2018**, *10*, 32–36.

[19] S. Liu, J. Liu, X. Hou, T. Xu, J. Tong, J. Zhang, B. Ye, B. Liu, *Langmuir* **2018**, *34*, 3654–3660.

[20] A. Koutsianos, R. Pallach, L. Frentzel-Beyme, C. Das, M. Paulus, C. Sternemann, S. Henke, *Nat. Commun.* **2023**, *14*, 1–10.

[21] R. E. Mow, G. A. Russell-Parks, G. E. B. Redwine, B. E. Petel, T. Gennett, W. A. Braunecker, *Chem. Mater.* **2024**, *36*, 1579–1590.

[22] Z. Deng, W. Ying, K. Gong, Y. J. Zeng, Y. Yan, X. Peng, *Small* **2020**, *16*, 1907016.

[23] J. Cahir, M. Y. Tsang, B. Lai, D. Hughes, M. A. Alam, J. Jacquemin, D. Rooney, S. L. James, *Chem. Sci.* **2020**, *11*, 2077–2084.

[24] K. Jie, N. Onishi, J. A. Schott, I. Popovs, D. Jiang, S. Mahurin, S. Dai, *Angew. Chemie* **2020**, *132*, 2288–2292.

[25] D. Wang, Y. Xin, X. Li, F. Wang, Y. Wang, W. Zhang, Y. Zheng, D. Yao, Z. Yang, X. Lei, *Chem. Eng. J.* **2021**, *416*, 127625.

[26] B. Lai, J. Cahir, M. Y. Tsang, J. Jacquemin, D. Rooney, B. Murrer, S. L. James, *ACS Appl. Mater. Interfaces* **2021**, *13*, 932–936.

[27] J. M. Rimsza, T. M. Nenoff, *ACS Appl. Mater. Interfaces* **2022**, *14*, 18005–18015.

[28] B. D. Egleston, A. Mroz, K. E. Jelfs, R. L. Greenaway, *Chem. Sci.* **2022**, *13*, 5042–5054.

[29] Z. Zhang, B. Yang, B. Zhang, M. Cui, J. Tang, X. Qiao, *Nat. Commun.* **2022**, *13*, 2353.

[30] F. Zhang, F. Yang, J. Huang, B. G. Sumpter, R. Qiao, *J. Phys. Chem. B* **2016**, *120*, 7195–7200.

[31] R. J. Kearsey, B. M. Alston, M. E. Briggs, R. L. Greenaway, A. I. Cooper, *Chem.*

Sci. **2019**, *10*, 9454–9465.

[32] M. Atilhan, A. Cincotti, S. Aparicio, *J. Mol. Liq.* **2021**, *330*, 115660.

[33] I. Borne, N. Simon, C. W. Jones, R. P. Lively, *Ind. Eng. Chem. Res.* **2022**, *61*, 11908–11921.

[34] M. Costa Gomes, L. Pison, C. Červinka, A. Padua, *Angew. Chemie* **2018**, *130*, 12085–12088.

[35] R. Gaillac, P. Pullumbi, K. A. Beyer, K. Chapman, D. A. Keen, T. D. Bennett, F. X. Coudert, *Nat. Mater.* **2017**, *16*, 1149–1155.

[36] T. D. Bennett, F. X. Coudert, S. L. James, A. I. Cooper, *Nat. Mater.* **2021**, *20*, 1179–1187.

[37] M. C. Brand, H. G. Trowell, M. J. Fuchter, R. L. Greenaway, *Chem. - A Eur. J.* **2024**, *30*, DOI 10.1002/chem.202303593.

[38] N. Giri, C. E. Davidson, G. Melaugh, M. G. Del Pópolo, J. T. A. Jones, T. Hasell, A. I. Cooper, P. N. Horton, M. B. Hursthouse, S. L. James, *Chem. Sci.* **2012**, *3*, 2153–2157.

[39] P. Li, J. A. Schott, J. Zhang, S. M. Mahurin, Y. Sheng, Z. Qiao, X. Hu, G. Cui, D. Yao, S. Brown, Y. Zheng, S. Dai, *Angew. Chemie* **2017**, *129*, 15154–15158.

[40] P. F. Fulvio, S. Dai, *Chem* **2020**, *6*, 3263–3287.

[41] B. D. Egleston, K. V. Luzyanin, M. C. Brand, R. Clowes, M. E. Briggs, R. L. Greenaway, A. I. Cooper, *Angew. Chemie - Int. Ed.* **2020**, *59*, 7362–7366.

[42] D. Wang, Y. Xin, D. Yao, X. Li, H. Ning, H. Zhang, Y. Wang, X. Ju, Z. He, Z. Yang, W. Fan, P. Li, Y. Zheng, *Adv. Funct. Mater.* **2022**, *32*, 1–45.

[43] D. Wang, Y. Ying, Y. Xin, P. Li, Z. Yang, Y. Zheng, *Accounts Mater. Res.* **2023**, *4*, 854–866.

[44] J. Zhang, N. Lv, Y. Chao, L. Chen, W. Fu, J. Yin, H. Li, W. Zhu, H. Li, *J. Mol. Graph. Model.* **2020**, *100*, 107694.

[45] M. Z. Ahmad, A. Fuoco, *Curr. Res. Green Sustain. Chem.* **2021**, *4*, 100070.

[46] R. L. Greenaway, D. Holden, E. G. B. Eden, A. Stephenson, C. W. Yong, M. J. Bennison, T. Hasell, M. E. Briggs, S. L. James, A. I. Cooper, *Chem. Sci.* **2017**, *8*, 2640–2651.

[47] K. Bartik, M. Luhmer, S. J. Heyes, R. Ottinger, J. Reisse, *J. Magn. Reson. Ser. B* **1995**, *109*, 164–168.

[48] N. Tassali, N. Kotera, C. Boutin, E. Léonce, Y. Boulard, B. Rousseau, E. Dubost, F. Taran, T. Brotin, J.-P. Dutasta, P. Berthault, *Anal. Chem.* **2014**, *86*, 1783–1788.

[49] F. T. Hane, A. Fernando, B. R. J. Prete, B. Peloquin, S. Karas, S. Chaudhuri, S. Chahal, Y. Shepelytskyi, A. Wade, T. Li, B. Deboef, M. S. Albert, *ACS Omega* **2018**, *3*, 677–681.

[50] E. Léonce, J. P. Dognon, D. Pitrat, J. C. Mulatier, T. Brotin, P. Berthault, *Chem. - A Eur. J.* **2018**, *24*, 6534–6537.

[51] F. M. Alexander, S. F. Fonrouge, J. L. Borioni, M. G. Del Pópolo, P. N. Horton, S. J. Coles, B. P. Hutchings, D. E. Crawford, S. L. James, *Chem. Sci.* **2021**, *12*, 14230–14240.

[52] H. Kudo, R. Hayashi, K. Mitani, T. Yokozawa, N. C. Kasuga, T. Nishikubo, *Angew. Chemie - Int. Ed.* **2006**, *45*, 7948–7952.

[53] N. Niina, H. Kudo, T. Nishikubo, *Chem. Lett.* **2009**, *38*, 1198–1199.

[54] N. Niina, H. Kudo, K. Maruyama, T. Kai, T. Shimokawa, H. Oizumi, T. Itani, T. Nishikubo, *Polym. J.* **2011**, *43*, 407–413.

[55] R. S. Patil, D. Banerjee, C. M. Simon, J. L. Atwood, P. K. Thallapally, *Chem. - A Eur. J.* **2016**, *22*, 12618–12623.

[56] M. S. Syamala, R. J. Cross, M. Saunders, *J. Am. Chem. Soc.* **2002**, *124*, 6216–6219.

[57] K. W. Miller, N. V. Reo, A. J. M. Schoot Uiterkamp, D. P. Stengle, T. R. Stengle, K. L. Williamson, *Proc. Natl. Acad. Sci. U. S. A.* **1981**, *78*, 4946–4949.

[58] Y. H. Lim, A. D. King, *J. Phys. Chem.* **1993**, *97*, 12173–12177.

[59] P. Morgado, R. Bonifacio, F. G. Martins, E. J. M. Filipe, *J. Phys. Chem. B* **2013**, *117*, 9014–9024.

[60] Y. H. Lim, N. Nugara, A. D. King, *Appl. Magn. Reson.* **1995**, *8*, 521–534.

[61] M. Claessens, O. Fabre, D. Zimmermann, J. Reisse, *Bull. des Sociétés Chim. Belges* **1984**, 983–989.

[62] K. M. Marczenko, H. P. A. Mercier, G. J. Schrobilgen, *Angew. Chemie - Int. Ed.* **2018**, *57*, 12448–12452.

[63] M. Oschatz, H. C. Hoffmann, J. Pallmann, J. Schaber, L. Borchardt, W. Nickel, I. Senkovska, S. Rico-Francés, J. Silvestre-Albero, S. Kaskel, E. Brunner, *Chem.*

Mater. **2014**, *26*, 3280–3288.

[64] Y. X. Ma, Z. J. Li, L. Wei, S. Y. Ding, Y. B. Zhang, W. Wang, *J. Am. Chem. Soc.* **2017**, *139*, 4995–4998.

[65] K. S. Han, S. D. Burton, E. D. Walter, Y. Shin, W. Kuang, K. L. Simmons, *J. Phys. Chem. B* **2022**, *126*, 3135–3142.

[66] J. Demarquay, J. Fraissard, *Chem. Phys. Lett.* **1987**, *136*, 314–318.

[67] T. Suzuki, M. Miyauchi, H. Yoshimizu, Y. Tsujita, *Polym. J.* **2001**, *33*, 934–938.

[68] G. Golemme, J. B. Nagy, A. Fonseca, C. Algieri, Y. Yampolskii, *Polymer (Guildf).* **2003**, *44*, 5039–5045.

[69] C. D. Keenan, M. M. Herling, R. Siegel, N. Petzold, C. R. Bowers, E. A. Rössler, J. Breu, J. Senker, *Langmuir* **2013**, *29*, 643–652.

[70] E. Tocci, L. De Lorenzo, P. Bernardo, G. Clarizia, F. Bazzarelli, N. B. McKeown, M. Carta, R. Malpass-Evans, K. Friess, K. Pilnáček, M. Lanč, Y. P. Yampolskii, L. Strarannikova, V. Shantarovich, M. Mauri, J. C. Jansen, *Macromolecules* **2014**, *47*, 7900–7916.

[71] B. Gierczyk, R. Pankiewicz, *Cent. Eur. J. Chem.* **2014**, *12*, 624–634.

[72] S. Komulainen, J. Roukala, V. V. Zhivonitko, M. A. Javed, L. Chen, D. Holden, T. Hasell, A. Cooper, P. Lantto, V. V. Telkki, *Chem. Sci.* **2017**, *8*, 5721–5727.

[73] P. Morgado, K. Shimizu, J. M. S. S. Esperanc, M. Reis, P. N. Rebelo, J. N. C. Lopes, E. J. M. Filipe, *J. Phys. Chem. Lett.* **2013**, *4*, 2758–2762.

[74] C. J. Jameson, D. N. Sears, S. Murad, *J. Chem. Phys.* **2004**, *121*, 9581–9592.

[75] F. Castiglione, G. Saielli, M. Mauri, R. Simonutti, A. Mele, *J. Phys. Chem. B* **2020**, *124*, 6617–6627.

[76] G. Saielli, F. Castiglione, M. Mauri, R. Simonutti, A. Mele, *ChemPhysChem* **2021**, *22*, 1880–1890.

[77] A. Moschos, J. Reisse, *J. Magn. Reson.* **1991**, *95*, 603–606.

[78] K. Oikarinen, J. Jokisaari, *Appl. Magn. Reson.* **1995**, *8*, 587–595.

[79] M. Pfeffer, O. Lutz, *J. Magn. Reson. Ser. A* **1995**, *113*, 108–113.

[80] J. Wolber, S. J. Doran, M. O. Leach, A. Bifone, *Chem. Phys. Lett.* **1998**, *296*, 391–396.

4. Insights into the structure of type V deep eutectic solvents

Parts of this Chapter have been published in

M. Boventi, M. Mauri, F. Castiglione, R. Simonutti, *Faraday Discuss.* **2024**, Advance Article.

4.1 Introduction

Deep eutectic solvents (DESs) are a novel class of solvents formed by mixing two or more appropriate neat constituents, obtaining a mixture with a melting point significantly lower than that of the individual components. Since the groundbreaking work of Abbott and co-workers on choline chloride:urea in 2003,[1] deep eutectic solvents have gained attention as promising alternatives to traditional organic solvents in both research and industrial applications.[2] The growing interest in DESs stems from their exceptional solvent and physical properties, such as low melting point, high thermal stability, and low volatility, combined with the fact that they can be produced from green and sustainable materials.[3] This makes them also potentially non-toxic, environmentally friendly, and highly cost-effective.[4–8] Deep eutectic solvents are also generally easy to prepare. The most common preparation method consists in simply heating and stirring the components under an inert atmosphere, such as nitrogen or argon, until a homogeneous liquid is formed. Other preparation methods include vacuum evaporation, grinding, and freeze-drying. In vacuum evaporation, an aqueous solution of the components is prepared, followed by evaporation of water under vacuum at 323 K. The grinding method consists in grinding the solid components in a mortar until a homogeneous liquid is obtained. This is often performed in a glovebox under an

inert atmosphere. Lastly, in freeze-drying, the components are dissolved in water, frozen, and freeze dried to obtain a clear liquid.

Since deep eutectic solvents can be prepared by simply mixing a general hydrogen bond donor (HBD) with a general hydrogen bond acceptor (HBA), there is an estimated of at least 10^6 different possible compositions.[4] Note that this number does not include the more complex three-component DESs that have been the subject of several papers in recent years.[9–12] Given this massive number of possible combinations, task-specific deep eutectic solvents can be developed and tailored to optimize the physicochemical properties, for example, density, viscosity, and solubility, matching those required for a selected application.[13–18] Common hydrogen bond donors used in DESs include urea, acetamide, glycerol, ethylene glycol, menthol, thymol, lactic acid, and linear carboxylic acids. On the other hand, the most common hydrogen bond acceptors are quaternary ammonium salts, for example choline chloride, tetraethylammonium chloride, tetrabutylammonium bromide, and benzyltriphenylphosphonium chloride. Nonionic species, such as glycine, proline, alanine, and nicotinic acid, can also be used as hydrogen bond donors.

Although many eutectic mixtures have been classified as DESs, it is crucial to distinguish between a simple eutectic mixture and an actual deep eutectic solvent. Martins et al. addressed this important distinction by defining a DES as a mixture whose eutectic point is lower than that of a thermodynamically ideal mixture.[19] The non-ideal behavior of DESs is generally attributed to the stronger intermolecular interactions between the two different components compared to those within the same component.[20,21] Therefore, to formally determine whether a mixture qualifies as a deep eutectic solvent, its solid-liquid phase diagram must be analyzed and compared with the ideal case. Importantly, the definition of Martins et al. applies not only to the eutectic point but also to the entire compositional range where the mixture remains liquid at the operating temperature for a certain process or system of interest.[19]

Based on the chemistry of their constituents, deep eutectic solvents have been classified into five different types.[4,5,22] Type I DESs are formed by a quaternary ammonium salt and a metal chloride. Type II consist of a quaternary ammonium salt and a metal chloride hydrate. Type III DESs are constituted by a quaternary ammonium salt mixed with a general hydrogen bond donor, typically an organic molecule such as

an alcohol, a carboxylic acid, or an amide. Deep eutectic solvents of this type are by far the most common: most of the reported research works on DESs are focused on their properties and, especially, their applications. Type IV are formed with a metal chloride hydrate and a general HBD. While type I-IV are composed of at least one ionic species, the recently proposed type V DESs are entirely non-ionic and composed only of molecular hydrogen bond donors and acceptors.[21,23] These novel deep eutectic solvents have demonstrated promising potential in various applications including extraction of metals and organic molecules,[24–28] separation processes,[29–32] gas capture,[33,34] detection of water pollutants,[12,35] and drug solubilization and delivery.[36,37] Among all the possible applications, CO_2 capture and separation is one of the most promising, thanks to the hydrophobic character of type V DESs.[38,39] Indeed, sometimes they are also indicated as hydrophobic eutectic solvents, HESs, even though this broad definition includes hydrophobic type I-IV solvents.

A recent study has explored the potential of hydrophobic nonionic deep eutectic solvents (DESs) derived from menthol and phenolic alcohols for the solubilization of carbon dioxide.[40] The authors applied the conductor-like screening model for realistic solvation (COSMO-RS) on a series of mixtures with different constituents and compositions to predict the CO_2 solubility, identifying the best ones to investigate experimentally. The screening identified the type V deep eutectic solvents L-menthol:thymol in a 1:2 molar ratio and thymol:2,6-xylenol in a 1:1 molar ratio as promising candidates for CO_2 solubilization. Thus, the authors prepared these DESs, and they measured the CO_2 solubility at different temperatures and gas pressures. This confirmed that these systems had higher performances than some popular ionic DESs and ionic liquids reported in the literature. In another recent study, the solubility of carbon dioxide in several natural deep eutectic solvents (NADESs) composed of thymol, menthol, camphor, octanoic acid, and 1-decanol, was evaluated experimentally to find the optimal composition.[41] The authors found that the thymol:camphor NADES had the best CO_2 capture efficiency. Thus, they optimized the CO_2 solubilization performance of this solvent by determining the best temperature and pressure conditions. In addition to that, they performed molecular dynamics simulations to understand the interactions involved in the dissolution of carbon dioxide. The results demonstrated that the high performances were mainly determined by the interaction

between thymol and carbon dioxide, while the presence of camphor decreased the mobility of CO_2 inside the solvent.

Despite the wealth of published works on DESs in the last few years, there is still a significant gap in the fundamental knowledge about the origin of their peculiar physical properties and the relationships between structure and properties.[42] A detailed understanding of the structural organization of deep eutectic solvents, and how this determines their outstanding physical and solvent properties, would help significantly in the spreading of these novel materials. Moreover, this would contribute to increasing their effectiveness in different applications and even help in creating predictive models useful to design task-specific solvents a priori.[43]

In this context, the nuclear magnetic resonance (NMR) spectroscopy of noble gases, particularly xenon, is especially valuable thanks to its ability to probe the matter at the nanoscopic level in a non-destructive and highly detailed manner. As described in detail in the previous Chapters, ^{129}Xe has been used as an inert probe to study the structure of isotropic liquids,[44–48] liquid mixtures,[49–51] and even supramolecular complexes in liquid solutions.[52–55] In addition to that, in the last decade this technique has found use in the analysis of the complex structural organization of ionic liquids, which are considered by many as very similar to deep eutectic solvents.[56–58] For example, in a work published in 2020, the ^{129}Xe NMR analysis of a series of 1-alkyl-3-methylimidazolium ionic liquids with the Cl^- and PF_6^- anions revealed that these systems segregate into polar and nonpolar nanodomains with radically different chemical and transport properties.[59] The experimental results were also supported by molecular dynamics (MD) simulations, which showed two different networks of alkyl and polar domains, respectively. In a later work, the authors studied a series of ionic liquids with analogous cations but containing the bis(trifluoromethylsulfonyl)imide (TFSI) anion.[60] ^{129}Xe NMR coupled with molecular dynamics simulations demonstrated that the presence of the rather hydrophobic TFSI anion radically changes the properties of the ionic liquids, making nano-segregation much less defined thanks to the possibility of the anions to diffuse in the alkyl domains, provided by their nonpolar trifluoromethyl moieties. Moreover, xenon NMR has also been employed alongside other techniques, such as small angle X-ray scattering (SAXS) and positron annihilation lifetime spectroscopy (PALS), to study the free volume of ionic liquid mixtures.[61,62]

In this Chapter, for the first time, we report the application of ^{129}Xe NMR spectroscopy to the investigation of the liquid structures of deep eutectic solvents and general eutectic mixtures. We have analyzed the reported deep eutectic solvents menthol:thymol and thymol:camphor,[23,41,63,64] alongside a series of known ideal eutectic mixtures formed by menthol as HBA and carboxylic acids with 8-14 carbon atoms as HBDs.[32,65] Several NMR parameters such as variable-temperature chemical shift, spin-lattice relaxation time, and self-diffusion coefficients, provided valuable information about the nanoscopic organization and the dynamic properties of the mixtures, demonstrating that ^{129}Xe NMR can be a powerful resource for the characterization of deep eutectic solvents.

4.2 Experimental section

4.2.1 Materials

Isotopically enriched xenon gas with 86.6% ^{129}Xe isotopic enrichment was acquired from CortecNet. L-menthol (99% purity) was obtained from Thermo Scientific. Octanoic acid (≥98%), dodecanoic acid (98%), thymol (≥98.5%), and camphor (96%) were obtained from Merck. Decanoic acid (99%) was purchased from Acros Organics. Tetradecanoic acid (99%) was purchased from Fluka Analytics. All reagents were used as received without further purification.

4.2.2 Binary mixtures preparation

Binary mixtures were prepared following a procedure reported in the literature.[65] The components were precisely weighed using an analytical balance and placed into 40 mL glass vials at the specified molar ratios. The mixtures were then heated to 60 °C while stirring with a magnetic stirrer for several hours until clear and homogeneous liquids were obtained. Afterward, the mixtures were cooled to room temperature and stored under nitrogen to prevent moisture. Deep eutectic solvents composed of menthol (Menth), thymol (Thym), and camphor (Camph) were prepared both at the eutectic and at different compositions. Besides, binary eutectic mixtures (EMs) of menthol and octanoic (OctA), decanoic (DecA), dodecanoic (DodecA), and tetradecanoic or myristic

(MyrA) acids were prepared along with low-melting mixtures (LMMs) of the same components with molar ratios different to the eutectic point. The prepared mixtures and their characteristics are listed in Table 4.1, while the chemical structures of the components used in this work are represented in Figure 4.1.

Table 4.1. Prepared mixtures and molar ratios of the components. DES, deep eutectic solvent, refers to non-ideal solvents at the eutectic compositions; EM, eutectic mixture, refers to non-DES binary mixtures at the eutectic compositions; LMM, low-melting mixture, refers to a binary mixture at a composition different from the eutectic point.

Components	Molar ratio	Type
Thymol:Camphor	0.5:0.5	DES
Thymol:Camphor	0.3:0.7	LMM
Thymol:Camphor	0.7:0.3	LMM
Menthol:Thymol	0.5:0.5	DES
Menthol:Octanoic acid	0.56:0.44	EM
Menthol:Octanoic acid	0.36:0.64	LMM
Menthol:Octanoic acid	0.76:0.24	LMM
Menthol:Decanoic acid	0.6:0.4	EM
Menthol:Decanoic acid	0.4:0.6	LMM
Menthol:Decanoic acid	0.8:0.2	LMM
Menthol:Decanoic acid	0.2:0.8	LMM
Menthol:Dodecanoic acid	0.75:0.25	EM
Menthol:Dodecanoic acid	0.6:0.4	LMM
Menthol:Dodecanoic acid	0.9:0.1	LMM
Menthol:Myristic acid	0.8:0.2	EM

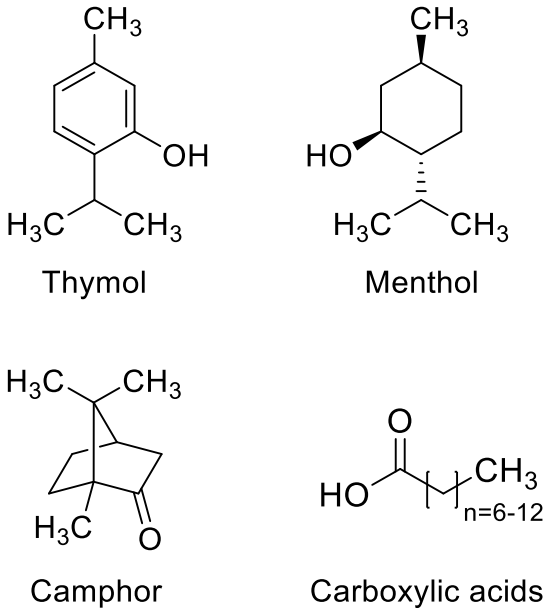

Figure 4.1. Chemical structures of the components used in the preparation of deep eutectic solvents, eutectic mixtures, and low-melting mixtures.

4.2.3 NMR sample preparation

A medium-wall Wilmad 504-PP-8 NMR tube with 5 mm outer diameter and 3.43 mm inner diameter was filled with a small amount of liquid sample (0.2-0.5 mL). The NMR tube was connected to a Schlenk line, and the liquid was degassed under a dynamic vacuum at a pressure of 6.0×10^{-2} torr by performing freeze-pump-thaw cycles until no gas bubbles were observed inside. Isotopically enriched xenon gas, with 86.6% ^{129}Xe, was introduced into a section of the manifold with a known volume, and its quantity was determined by measuring the pressure with an inline pressure gauge. The gas was then brought into contact with the sample and trapped within the tube by freezing it using liquid nitrogen. The tube was carefully flame-sealed, ensuring the sealing area was free of any liquid droplets that might decompose and contaminate the sample. Then, the NMR tube was gradually warmed to room temperature and allowed to equilibrate for several days before measurements were performed. For diffusion NMR experiments, the same preparation method was followed, with the addition of a thin, sealed capillary tube containing a small volume of DMSO-d_6 (80-100 µL) inside the NMR tube for deuterium lock. Across all samples, the final nominal xenon pressure ranged from 2 to 4 bar.

4.2.4 NMR spectroscopy

One-dimensional ^{129}Xe NMR spectra and spin-lattice relaxation times were measured on a Bruker Avance 500 spectrometer having a Larmor frequency of 500.13 MHz for ^{1}H, corresponding to 139.09 MHz for ^{129}Xe. The instrument was equipped with a double resonance direct observe broadband (BBO) probe. 1D ^{129}Xe NMR spectra were acquired with a number of scans between 8 and 256 to obtain a good signal-to-noise ratio. The relaxation delay was in the range of 60-200 s. ^{129}Xe chemical shifts were referenced by setting the signal of xenon dissolved in pure benzene at 298 K to 188.1 ppm.[66] Variable temperature spectra were acquired every 10 K in different temperature intervals depending on the melting points of the samples. ^{129}Xe spin-lattice relaxation times (T_1) were measured using the Inversion Recovery pulse sequence with the default t1ir Bruker pulse program. Each measurement consisted of 12 delay increments with a number of scans between 8 and 16 for each increment. The long relaxation delay was in the range of 200-400 s to ensure the complete relaxation of ^{129}Xe nuclei. The probe temperature was controlled with airflow using a Bruker BVT3000 variable temperature unit with an uncertainty of 0.1 K. Low-temperature experiments were performed by connecting a liquid nitrogen evaporator to the BBO probe. This was also controlled with the Bruker BVT3000 variable temperature unit.

Pulsed field gradient (PFG) NMR experiments were performed on a Bruker Avance Neo 500 spectrometer equipped with a direct observe broadband including ^{19}F (BBFO) iProbe. Experiments were performed using the bipolar pulse longitudinal eddy current delay (BPPLED) pulse sequence.[67] This pulse sequence consists of a stimulated echo block at the end of which the magnetization is stored longitudinally. Afterward, a crushing gradient pulse is applied to remove any residual transverse magnetization. This is followed by a time delay sufficiently long for all eddy currents to become negligible. Then, a final $\pi/2$ readout pulse is applied prior to the acquisition. A pulsed field gradient unit was employed to produce gradients having an intensity of up to 53 G/cm. The gradient pulse intensity was incremented from 2% to 95% of the maximum value in 24 linear steps. For each sample, the gradient pulse duration (δ) and the diffusion delay (Δ) were optimized to obtain about 95% signal intensity attenuation from the first to the last gradient pulse intensity value. ^{129}Xe diffusion experiments were performed with the following acquisition parameters: δ = 6 ms, Δ = 120-360 ms,

relaxation delay in the range of 150-200 s, and 16 scans for each linear step. The acquisition parameters for ^{1}H diffusion experiments were δ = 6 ms, Δ = 200-300 ms, 10 s relaxation delay, and 8 scans for each linear step. All experiments were performed at 298 K. The temperature was controlled with airflow using a Bruker BVT3000 variable temperature unit.

4.3 Results and discussion

4.3.1 Eutectic mixtures and deep eutectic solvents

For all the samples, the ^{129}Xe NMR spectrum of dissolved xenon shows a single, sharp, and intense peak, as usually observed for xenon in isotropic and anisotropic liquids. As an example, Figure 4.2 shows the spectra of xenon dissolved in mixtures of menthol and octanoic, decanoic, and dodecanoic acid at their eutectic compositions (see Table 4.1), acquired at 298 K.

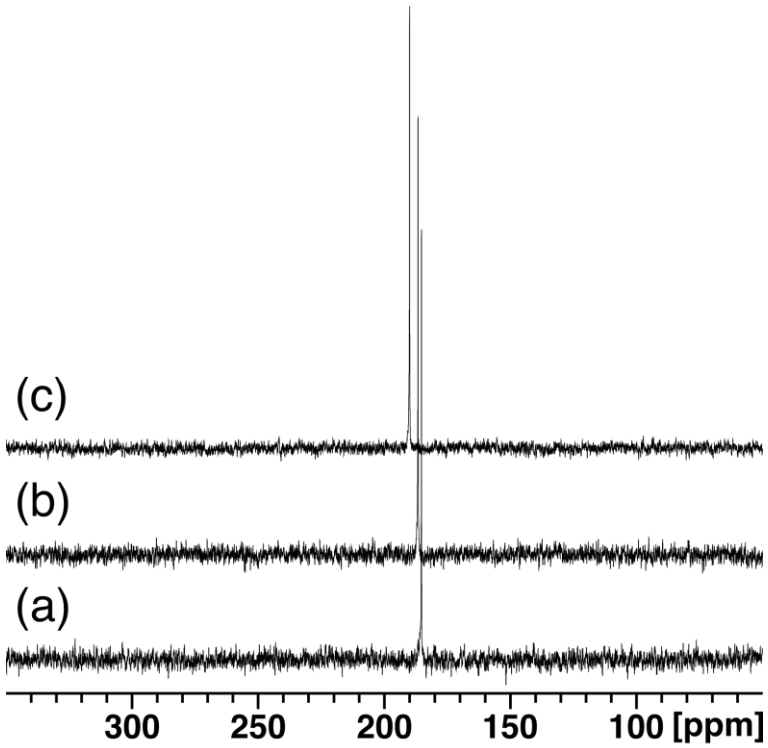

Figure 4.2. ^{129}Xe NMR spectra of xenon dissolved in mixtures of (a) menthol and octanoic acid (molar ratio 0.56:0.44), (b) menthol and decanoic acid (molar ratio 0.6:0.4), and (c) menthol and dodecanoic acid (molar ratio 0.75:0.25). The spectra were acquired at 298 K.

The chemical shifts of xenon loaded in the binary mixtures at their eutectic compositions, measured at 298 K and 308 K, are reported in Table 4.2. At 298 K, the chemical shifts fall within a rather narrow range, from 188.5 ppm for the eutectic mixture Menth:OctA 0.56:0.44 to 198.0 ppm for the deep eutectic solvent Thym:Camph 0.5:0.5. Xenon dissolved in the other type V deep eutectic solvent, Menth:Thym 0.5:0.5, has the second highest chemical shift at 194.2 ppm. The chemical shift of xenon dissolved in the eutectic mixture menthol and myristic acid 0.8:0.2 at 298 K could not be determined. This is because the sample was very close to its melting point, and it presented a very high viscosity.[65] Thus, the ^{129}Xe NMR spectrum showed only a very broad resonance, barely distinguishable from the baseline noise even after several scans. At 308 K and higher temperatures, the viscosity was low enough to allow a reliable chemical shift measurement.

Table 4.2. ^{129}Xe chemical shift of xenon loaded in deep eutectic solvents (DESs) and eutectic mixtures (EMs) at 298 K and 308 K.

Sample	δ_{Xe} [ppm] at 298 K	δ_{Xe} [ppm] at 308 K
Thymol:Camphor (0.5:0.5)	198.0	195.4
Menthol:Thymol (0.5:0.5)	194.2	190.9
Menthol:Myristic acid (0.8:0.2)	-	190.1
Menthol:Dodecanoic acid (0.75:0.25)	193.0	190.0
Menthol:Decanoic acid (0.6:0.4)	189.8	186.7
Menthol:Octanoic acid (0.56:0.44)	188.5	185.2

It is well-known that the chemical shift of xenon dissolved in isotropic and anisotropic liquids is generally determined by non-covalent xenon-solvent interactions. As shown by Jameson et al. through molecular dynamics simulations, in molecular liquids the chemical shift of xenon is influenced by the free volume available to xenon and the range of free volumes sampled over time.[68] More specifically, the chemical shift is inversely proportional to the free volume, as in the case of gaseous xenon sorbed in porous materials.[69,70] Our results suggest that the thymol:camphor and menthol:thymol DESs have a smaller free volume compared to general eutectic

mixtures of menthol and carboxylic acids. This may be due to the more efficient packing of components in deep eutectic solvents, likely driven by strong hydrogen bonding interactions. These interactions are considered the key factor influencing the non-ideality observed in type V DESs.[21,71,72] This is a tentative explanation since xenon itself is not able to probe the strength of the hydrogen bonds involved in the formation of liquid DESs, but instead, it gives detailed morphological information. Molecular dynamics simulations could be employed in the future to validate this hypothesis.

Interestingly, when considering the menthol and carboxylic acids EMs, the chemical shift increases as a function of the number of carbon atoms, N_C, of the acid alkyl chain, until reaching a plateau at $N_C = 12$. This behavior is clearly visible in Figure 4.3, where the chemical shift of dissolved xenon at 308 K is represented as a function of N_C.

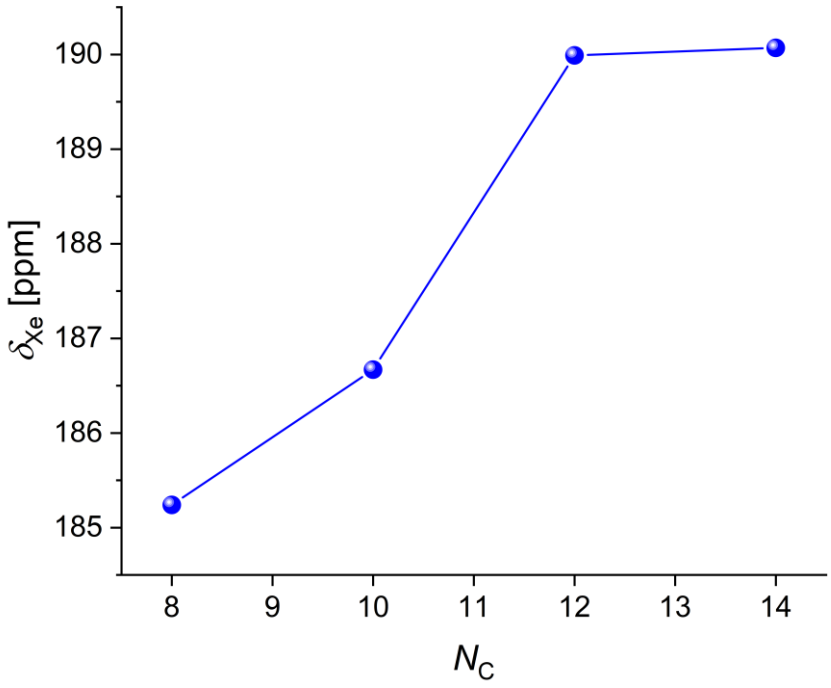

Figure 4.3. Chemical shifts of xenon (308 K) dissolved in menthol and carboxylic acids EMs represented as a function of the number of carbon atoms of the carboxylic acid molecules (N_C).

The increase in the ^{129}Xe chemical shift with a growing number of carbon atoms has been previously observed in both linear alkanes and cycloalkanes.[48] This effect is

attributed to the deshielding influence of both $–CH_3$ and $–CH_2$ groups on xenon. Excluding the contribution of the carboxyl group, which can be considered approximately constant across different carboxylic acids, the rise in the chemical shift aligns with the enhanced deshielding caused by a greater number of methylene groups interacting with xenon. This result also indicates that xenon atoms tend to be solvated by the nonpolar groups of the alkyl chains. In other words, xenon is preferentially located in the nonpolar alkyl portion of the EMs, as already observed in the case of perfluoroalkylalkanes and alkane/perfluoroalkane mixtures.[51,73]

To gain more insight into the nanostructure of the investigated mixtures, xenon T_1 relaxation times were determined at 298 K. The results are shown in Figure 4.4.

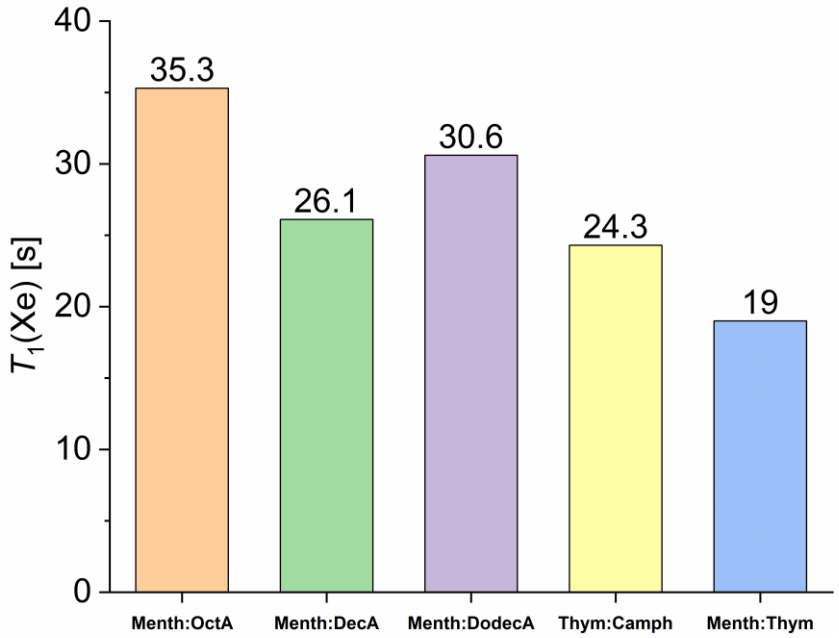

Figure 4.4. T_1 relaxation times of ^{129}Xe dissolved in eutectic mixtures and deep eutectic solvents at 298 K.

For all the samples, the T_1 values were obtained by fitting the Inversion Recovery data to a mono-exponential function. This indicates that xenon atoms experience a single homogeneous environment in the NMR time scale. For all the mixtures, the measured spin-lattice relaxation times are an order of magnitude lower than those of xenon dissolved in linear alkanes and in benzene.[59,74–76] Additionally, the two DESs show the lowest T_1 values, as well as the highest chemical shifts, compared to the EMs.

The primary relaxation mechanism for ^{129}Xe dissolved in liquids is known to be the dipolar interaction between ^{129}Xe and ^{1}H.[74–77] The strength of the dipolar interaction increases as the distance between the interacting nuclei decreases (see Section 1.1.3). The lower ^{129}Xe T_1 relaxation times in the case of DESs compared to general EMs suggest that, on average, the ^{129}Xe-^{1}H dipolar interaction is stronger in the former. This can be explained by an average shorter distance between xenon and hydrogen atoms, which again indicates that the free volume experienced by xenon is lower in deep eutectic solvents than in general eutectic mixtures.

Pulsed field gradient NMR experiments allowed us to study the self-diffusion of xenon and the components of the mixtures. The self-diffusion coefficients of xenon, $D(^{129}\text{Xe})$, determined at 298 K are reported in Figure 4.5. In all samples, the xenon diffusion coefficient is about one order of magnitude lower than that of xenon in water (2.2×10^{-9} m^2/s).[78] Furthermore, the $D(^{129}\text{Xe})$ values for the menthol:carboxylic acid eutectic mixtures consistently decrease as the number of carbon atoms of the carboxylic acid chain, N_C, increases. Martins et al. previously reported that the dynamic viscosities of menthol:carboxylic acid eutectic mixtures increase with higher N_C.[65] Our NMR diffusion measurements are consistent with these findings, as higher viscosity correlates with slower diffusion. This pattern is also reflected in the ^{1}H self-diffusion coefficients at 298 K, which follow the same trend but with values that are about an order of magnitude lower, as represented in Figure 4.6. This is due to the bigger dimensions of the constituents of the mixtures compared to the very small xenon atoms. The strong correlation between self-diffusion and dynamic viscosity indicates the absence of segregated nanodomains or cage-like aggregates. A similar behavior has been observed for xenon dissolved in 1-alkyl-3-methylimidazolium-based ionic liquids, where the self-diffusion coefficients of ^{129}Xe decreased with the alkyl chain length.[60]

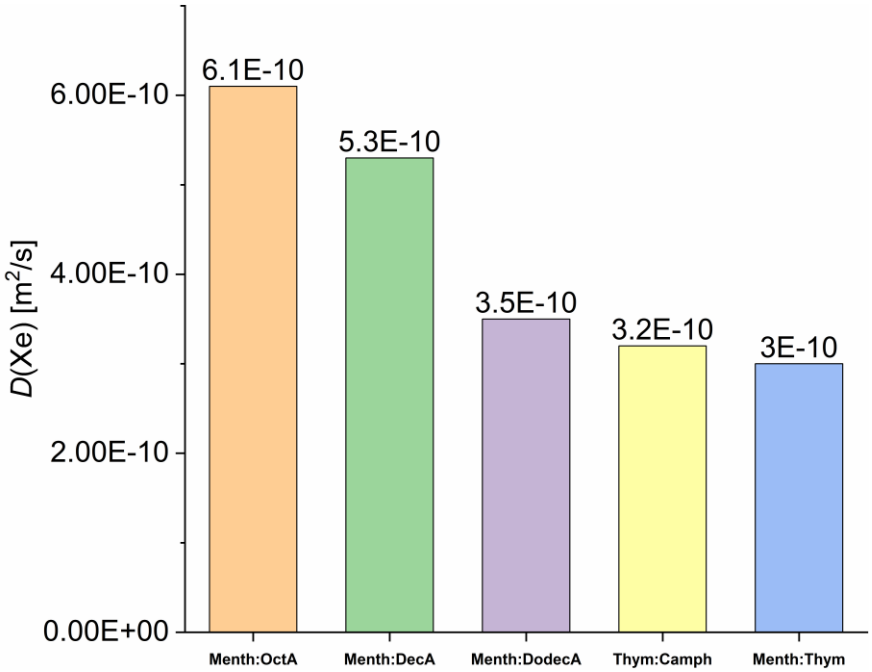

Figure 4.5. NMR self-diffusion coefficients of xenon in eutectic mixtures and deep eutectic solvents at 298 K.

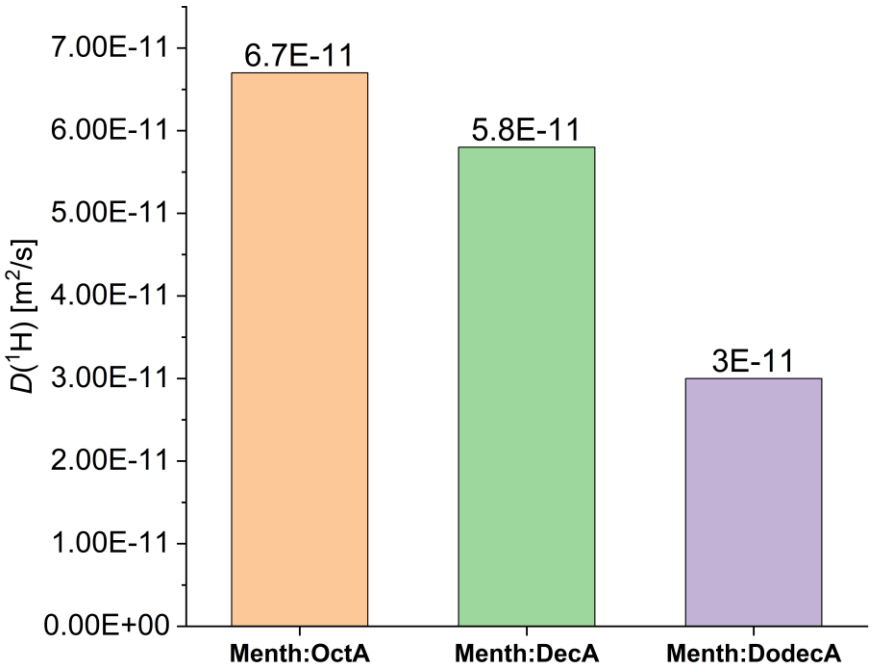

Figure 4.6. ^{1}H NMR self-diffusion coefficients of the constituents of eutectic mixtures measured at 298 K.

4.3.2 Mixtures with variable compositions and comparisons

A key factor affecting the physicochemical properties of the binary mixtures, such as viscosity, density, and CO_2 solubility, is the molar ratio between the hydrogen bond acceptor (HBA) and hydrogen bond donor (HBD).[40,41,79] To examine how the HBA:HBD molar ratio influences the nanostructure of these mixtures, ^{129}Xe NMR chemical shifts and spin-lattice relaxation times were measured for the low-melting mixtures (LMMs) Menth:OctA, Menth:DecA, Menth:DodecA, and Thym:Camph, at different compositions from the eutectic point.

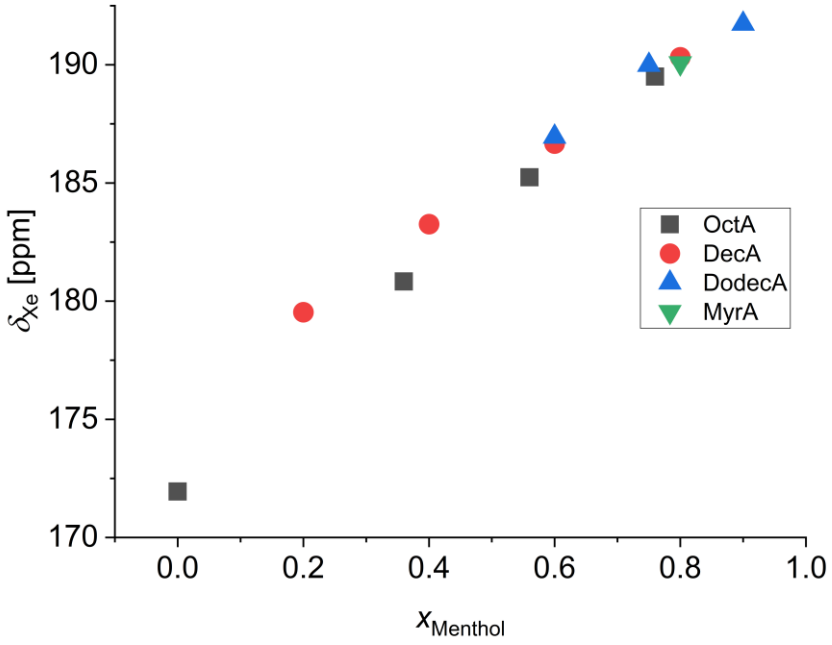

Figure 4.7. Chemical shifts of xenon in menthol:carboxylic acid mixtures as a function of the menthol molar fraction, measured at 308 K. The gray square at $x_{Menthol} = 0$ represents pure octanoic acid.

Figure 4.7 shows the chemical shift of xenon in the menthol:carboxylic acid mixtures as a function of the menthol molar fraction, measured at 308 K. The ^{129}Xe chemical shift of xenon dissolved in pure octanoic acid is also presented, as, among the employed carboxylic acids, this is the only one that is sufficiently above its melting point at 308 K to accurately measure the chemical shift of dissolved xenon. Figure 4.7 shows that the chemical shift is sensitive to the sample composition, increasing almost linearly with the molar fraction of menthol. Notably, at high menthol molar fractions,

the chemical shifts of dissolved xenon are nearly identical, independently of the type of carboxylic acid. This suggests that (1) at high menthol concentrations, the xenon chemical shift is predominantly influenced by interactions with the chemical groups of menthol, and (2) at lower menthol fractions, where the carboxylic acids become predominant in the mixtures, xenon tends to move away from menthol, being preferentially solvated by the nonpolar alkyl chains due to its hydrophobic nature.

Interestingly, the ^{129}Xe spin-lattice relaxation times, measured at 298 K, follow an opposite trend since they decrease with increasing the menthol molar fraction, as represented in Figure 4.8. The T_1 of xenon dissolved in the low-melting mixtures menthol:decanoic acid 0.2:0.8 and menthol:dodecanoic acid 0.6:0.4 and 0.9:0.1 could not be determined since the melting point of these mixtures is between 298 K and 308 K.[65]

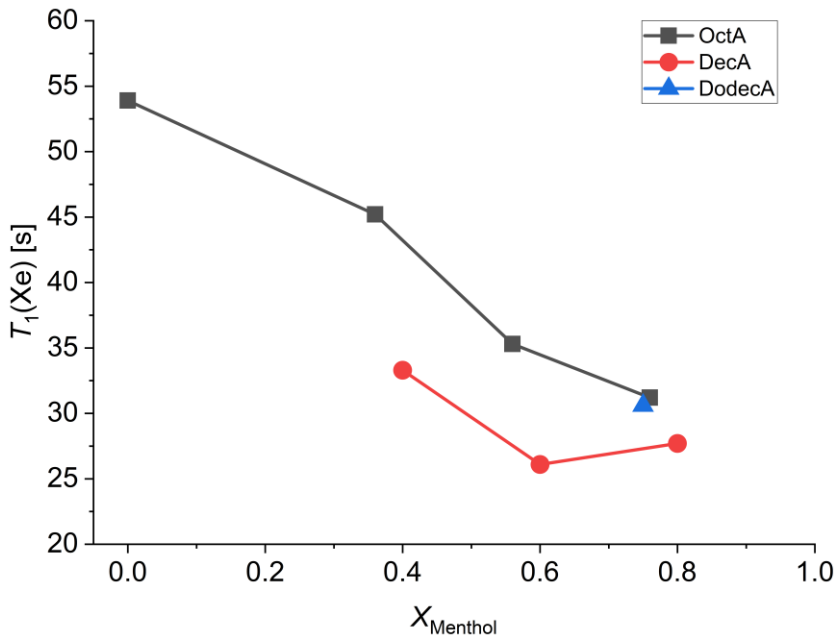

Figure 4.8. T_1 relaxation times of ^{129}Xe dissolved in menthol:carboxylic acid mixtures at 298 K as a function of the menthol molar fraction. The gray square at $x_{Menthol}$ = 0 represents pure octanoic acid.

Specifically, the spin-lattice relaxation times decrease from about 54 s for xenon dissolved in pure octanoic acid to 28 s in the mixture menthol:decanoic acid 0.8:0.2. This trend highlights the presence of stronger dipolar interactions between xenon and menthol molecules compared to those between xenon and carboxylic acids, suggesting

that menthol plays a dominant role in xenon relaxation. Indeed, as the molar fraction of menthol increases, the relaxation times become progressively independent of the structure of the carboxylic acid, as already observed in the chemical shifts at 308 K (Figure 4.7). This confirms that, at high menthol molar fractions, xenon atoms are primarily interacting with the chemical groups of menthol molecules. On the other hand, at lower menthol molar fractions ^{129}Xe is preferentially solvated by the alkyl chains of the carboxylic acid molecules. Naturally, a more comprehensive understanding of the nanostructure of these mixtures and of the precise mechanisms determining the T_1 trend could be gained by integrating the experimental findings with molecular dynamics simulations. These simulations could be conducted in the future to further elucidate the nanostructure of these mixtures.

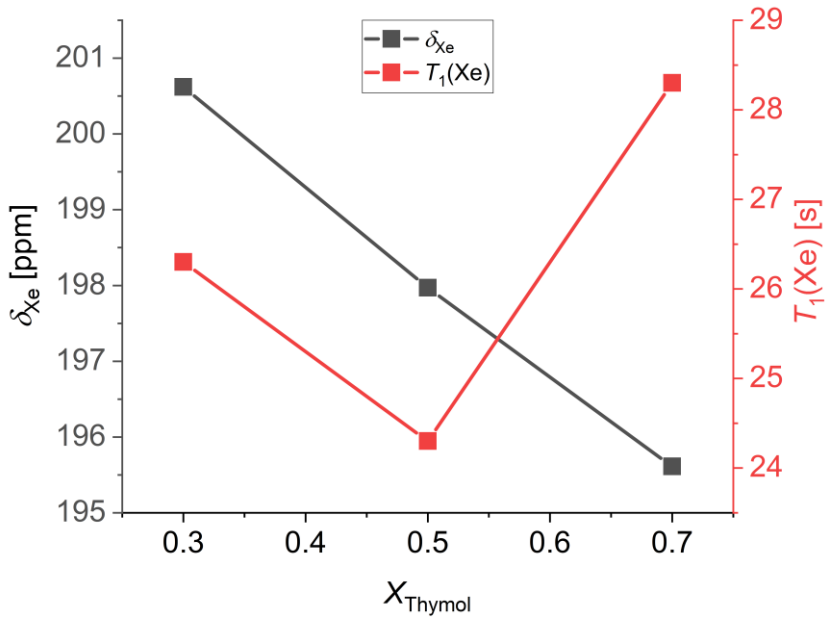

Figure 4.9. ^{129}Xe chemical shifts and T_1 relaxation times of xenon dissolved in thymol:camphor mixtures at 298 K as a function of the thymol molar fraction.

To examine the effect of the HBA:HBD ratio on the structure of a deep eutectic solvent, as opposed to a general eutectic mixture, we determined the chemical shifts and spin-lattice relaxation times of ^{129}Xe dissolved in thymol:camphor mixtures at 0.3:0.7 and 0.7:0.3 molar ratios. The results are represented in Figure 4.9 along with the data for the thymol:camphor 0.5:0.5 deep eutectic solvents presented in the previous section.

Notably, the chemical shift increases as the thymol molar fraction decreases, or, in other words, as the camphor molar fraction increases. Camphor, being a rigid and structurally constrained molecule (see Figure 4.1), imposes specific spatial limitations on its surroundings. This restriction reduces the average free volume available for xenon atoms as the camphor content increases, which in turn influences the chemical shift of dissolved xenon. Interestingly, the spin-lattice relaxation time of xenon in thymol:camphor mixtures exhibits a minimum at the eutectic composition. This indicates that the ^{129}Xe-^{1}H dipole-dipole interaction is more pronounced at the eutectic point compared to other compositions. A possible explanation for this behavior is that xenon experiences a markedly different environment in the deep eutectic solvent compared to the non-eutectic compositions. This in turn could be related to the physical and chemical interactions underlying the formation of deep eutectic solvents. Further studies on the spin-lattice relaxation of xenon dissolved in deep eutectic solvents are necessary to provide a more detailed and accurate explanation of this behavior.

4.3.3 Variable temperature ^{129}Xe NMR chemical shifts

To study the behavior of the menthol and carboxylic acid low-melting mixtures and eutectic solvents and the thymol:camphor DES, we measured the chemical shift of xenon dissolved in these systems every 10 K in the range of 298-348 K. Similar to the room temperature data shown in Figure 4.2, for all the samples the spectra showed a single, sharp and intense peak at every temperature. The chemical shifts of the peaks are represented in Figure 4.10 as a function of temperature. We note that we could not represent the data as a function of the reduced temperature, which is a better way to compare different samples in the same thermodynamic states (see Section 2.3.1),[48,57] since the critical temperature of the analyzed mixtures is unknown.

For all the mixtures, whether at eutectic or non-eutectic compositions, the chemical shift of dissolved xenon decreases linearly as the temperature increases. By applying a linear fit to the variable temperature data, we determined the temperature dependence of the chemical shift from the slopes of the resulting linear equations. The results are reported in Table 4.3.

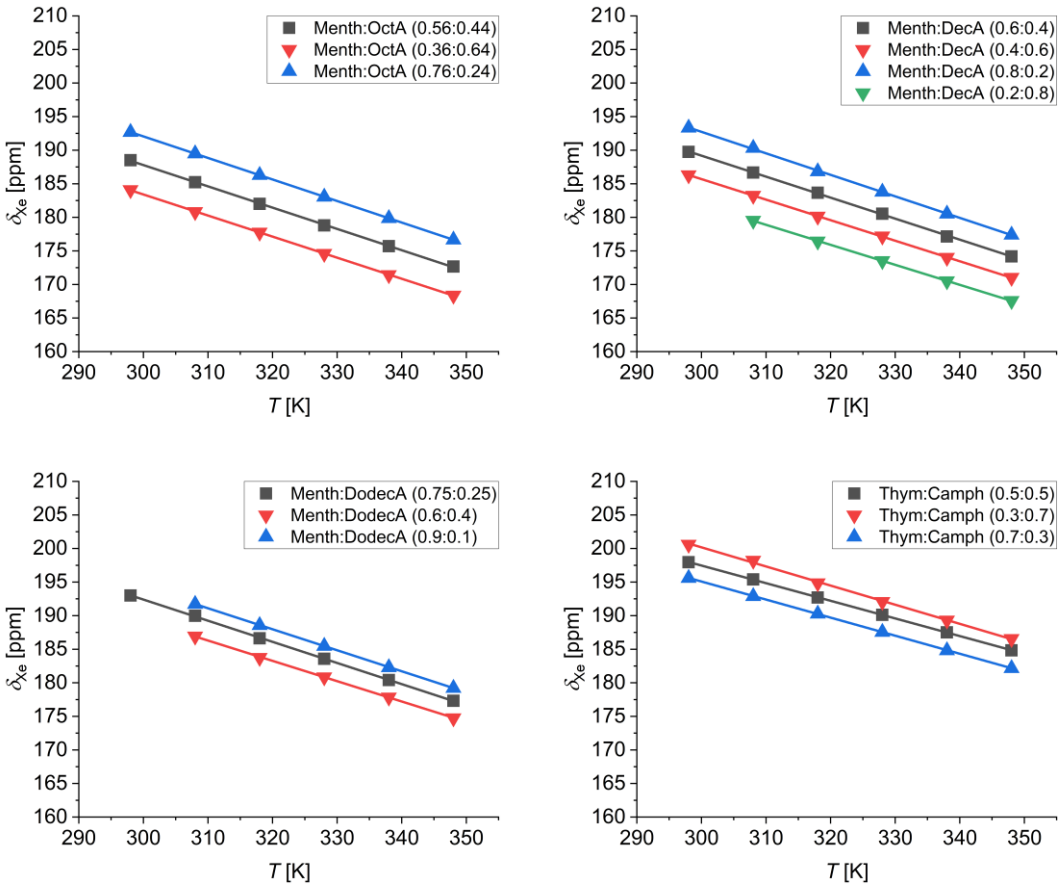

Figure 4.10. Variable-temperature ^{129}Xe chemical shift of xenon dissolved in menthol:carboxylic acid and thymol:camphor mixtures at different compositions. Gray squares represent mixtures at their eutectic compositions. The lines are linear fits to the data.

For all the menthol:carboxylic acid mixtures, the linear fits of the variable temperature data returned a slope very close to -0.3 ppm/K, which is similar to the values for xenon dissolved in various alkanes and cycloalkanes.[48] As noted by Jameson and co-workers, the temperature dependence of the chemical shift of xenon dissolved in liquids is primarily driven by changes in the free volume available to xenon as the temperature varies.[68] Thus, the linear trend and the similarity between our values and those of xenon in alkanes and cycloalkanes rule out the presence of cage-like structures or host-guest complexes between xenon and the molecules of the eutectic mixtures, suggesting that these systems behave as homogeneous isotropic liquids.

Table 4.3. Slopes of the linear equations resulting from the fits of variable-temperature ^{129}Xe chemical shifts.

Sample	$\Delta\delta/\Delta T$ [ppm/K]
Menthol:Octanoic acid (0.56:0.44)	-0.32
Menthol:Octanoic acid (0.36:0.64)	-0.31
Menthol:Octanoic acid (0.76:0.24)	-0.32
Menthol:Decanoic acid (0.6:0.4)	-0.31
Menthol:Decanoic acid (0.4:0.6)	-0.31
Menthol:Decanoic acid (0.8:0.2)	-0.32
Menthol:Decanoic acid (0.2:0.8)	-0.30
Menthol:Dodecanoic acid (0.75:0.25)	-0.31
Menthol:Dodecanoic acid (0.6:0.4)	-0.30
Menthol:Dodecanoic acid (0.9:0.1)	-0.31
Thymol:Camphor (0.5:0.5)	-0.26
Thymol:Camphor (0.3:0.7)	-0.28
Thymol:Camphor (0.7:0.3)	-0.27

The error is ±5%.

The chemical shift follows a linear trend with temperature even in the case of the thymol:camphor 0.3:0.7 and 0.7:0.3 mixture, as well as the 0.5:0.5 deep eutectic solvent. However, the dependence of the xenon chemical shift on temperature is slightly lower in these systems, being between -0.28 ppm/K and -0.26 ppm/K. Similar to the behavior observed in porous liquids (see Section 3.3.2), this is linked to a smaller variation in the free volume available to xenon with temperature changes. This phenomenon is influenced by the chemical structure of the components of the mixture. As previously mentioned, camphor is a rigid and constrained molecule, while thymol is an aromatic molecule with limited mobility. Therefore, it is reasonable to expect that, due to the structural rigidity of these molecules, the free volume experienced by xenon in these systems changes less with temperature compared to the mixtures with the

flexible alkyl chains of carboxylic acids and menthol, the non-aromatic counterpart of thymol.

4.4 Conclusions

In this Chapter, for the first time, we used ^{129}Xe NMR spectroscopy to explore the liquid structure of two type V deep eutectic solvents, menthol:thymol and thymol:camphor, as well as several eutectic mixtures composed of menthol and carboxylic acids, both at eutectic and non-eutectic compositions. The use of isotopically enriched ^{129}Xe gas allowed us to determine the chemical shift of dissolved xenon at variable temperatures, along with the spin-lattice relaxation times and diffusion coefficients at 298 K.

The chemical shifts and spin-lattice relaxation times of xenon in DESs and EMs measured at room temperature are sensitive to the chemical structure of the components of the mixtures and their molar ratios. The analysis of these NMR parameters suggests that the free volume experienced by xenon is lower in the deep eutectic solvents as opposed to the general eutectic mixtures, which is attributable to the more efficient spatial organization of the constituents of the DESs. Moreover, in the case of menthol:carboxylic acid mixtures with variable composition, the ^{129}Xe chemical shift and T_1 indicate that, at high menthol molar fractions, xenon mainly interacts with the chemical groups of menthol, while, at lower menthol molar fractions, xenon is preferentially located near the nonpolar alkyl chains of the carboxylic acids due to its hydrophobicity, similar to what has been observed in the case of 1-alkyl-3-methylimidazolium ionic liquids with variable alkyl chain length.[59] Variable temperature chemical shifts reveal that all the eutectic mixtures and the thymol:camphor deep eutectic solvents behave as homogeneous isotropic liquids. Moreover, the results indicate that the free volume changes less with temperature in the thymol:camphor DES compared to the EMs, most likely due to the high structural rigidity of thymol and camphor, similar to the results reported in Chapter 3 for porous liquids (see Section 3.3.2).

The NMR self-diffusion coefficients of xenon within the liquids suggest the absence of nano-segregation among the components of the mixture, aligning with the

reported viscosity data in the case of menthol:carboxylic acid mixtures.[65] This constitutes additional evidence that these systems can be considered as completely homogeneous liquids. These findings are also supported by the ^{1}H self-diffusion coefficients of the constituents of the mixture, which follow the same trend but on a lower order of magnitude, due to the bigger dimensions of the molecules compared to the small xenon atoms.

Overall, this Chapter demonstrates the possibility of using ^{129}Xe NMR spectroscopy to offer new insights into the complex structure of deep eutectic solvents and eutectic mixtures. The detailed information provided by this technique could help in understanding the intricated reasons behind the thermodynamic non-ideality of deep eutectic solvents, especially if combined with molecular dynamics simulations and quantum mechanical calculations in the future. This in turn would help tremendously in designing novel, efficient, and task-specific deep eutectic solvents, especially for applications such as gas capture and separation.

4.5 Bibliography

[1] A. P. Abbott, G. Capper, D. L. Davies, R. K. Rasheed, V. Tambyrajah, *Chem. Commun.* **2003**, 70–71.

[2] A. Mannu, M. Blangetti, S. Baldino, C. Prandi, *Materials (Basel).* **2021**, *14*, DOI 10.3390/ma14102494.

[3] A. Prabhune, R. Dey, *J. Mol. Liq.* **2023**, *379*, 121676.

[4] B. B. Hansen, S. Spittle, B. Chen, D. Poe, Y. Zhang, J. M. Klein, A. Horton, L. Adhikari, T. Zelovich, B. W. Doherty, B. Gurkan, E. J. Maginn, A. Ragauskas, M. Dadmun, T. A. Zawodzinski, G. A. Baker, M. E. Tuckerman, R. F. Savinell, J. R. Sangoro, *Chem. Rev.* **2021**, *121*, 1232–1285.

[5] T. El Achkar, H. Greige-Gerges, S. Fourmentin, *Environ. Chem. Lett.* **2021**, *19*, 3397–3408.

[6] J. Liu, X. Li, K. H. Row, *J. Mol. Liq.* **2022**, *362*, 119654.

[7] T. R. Sekharan, R. M. Chandira, S. Tamilvanan, S. C. Rajesh, B. S. Venkateswarlu, *Biointerface Res. Appl. Chem.* **2022**, *12*, 847–860.

[8] F. Oyoun, A. Toncheva, L. C. Henríquez, R. Grougnet, F. Laoutid, N. Mignet, K.

Alhareth, Y. Corvis, *ChemSusChem* **2023**, *16*, DOI 10.1002/cssc.202300669.

[9] Z. Ghazali, N. Suhaili, M. N. A. Tahari, M. A. Yarmo, N. H. Hassan, R. Othaman, *J. Mater. Res. Technol.* **2020**, *9*, 3249–3260.

[10] L. Xu, H. Jia, D. Zhu, F. Huan, R. Liu, W. Jiang, W. Zhu, H. Li, *J. Mol. Liq.* **2022**, *368*, 120725.

[11] L. Y. Ee, Y. K. Tan, J. Miao, H. T. Chu, S. F. Y. Li, *Green Chem.* **2023**, *25*, 3137–3151.

[12] M. F. Lanjwani, N. Altunay, M. Tuzen, *Food Chem.* **2023**, *400*, 134085.

[13] M. Francisco, A. Van Den Bruinhorst, M. C. Kroon, *Green Chem.* **2012**, *14*, 2153–2157.

[14] J. M. Silva, R. L. Reis, A. Paiva, A. R. C. Duarte, *ACS Sustain. Chem. Eng.* **2018**, *6*, 10355–10363.

[15] N. Zhang, Z. Huang, H. Zhang, J. Ma, B. Jiang, L. Zhang, *Ind. Eng. Chem. Res.* **2019**, *58*, 13321–13329.

[16] S. Arnaboldi, A. Mezzetta, S. Grecchi, M. Longhi, E. Emanuele, S. Rizzo, F. Arduini, L. Micheli, L. Guazzelli, P. R. Mussini, *Electrochim. Acta* **2021**, *380*, 138189.

[17] M. Shi, W. Xiong, Z. Tu, X. Zhang, X. Hu, Y. Wu, *Sep. Purif. Technol.* **2021**, *276*, 119357.

[18] Y. Chen, D. Zhao, Y. Bai, Y. Duan, C. Liu, J. Gu, X. Wang, X. Sun, Y. Li, L. Zhang, *J. Mol. Liq.* **2022**, *348*, 118031.

[19] M. A. R. Martins, S. P. Pinho, J. A. P. Coutinho, *J. Solution Chem.* **2019**, *48*, 962–982.

[20] J. Cao, E. Su, *J. Clean. Prod.* **2021**, *314*, 127965.

[21] D. O. Abranches, J. A. P. Coutinho, *Curr. Opin. Green Sustain. Chem.* **2022**, *35*, 100612.

[22] E. L. Smith, A. P. Abbott, K. S. Ryder, *Chem. Rev.* **2014**, *114*, 11060–11082.

[23] D. O. Abranches, M. A. R. Martins, L. P. Silva, N. Schaeffer, S. P. Pinho, J. A. P. Coutinho, *Chem. Commun.* **2019**, *55*, 10253–10256.

[24] N. Schaeffer, M. A. R. Martins, C. M. S. S. Neves, S. P. Pinho, J. A. P. Coutinho, *Chem. Commun.* **2018**, *54*, 8104–8107.

[25] M. Gilmore, É. N. McCourt, F. Connolly, P. Nockemann, M. Swadźba-Kwaśny,

J. D. Holbrey, *ACS Sustain. Chem. Eng.* **2018**, *6*, 17323–17332.

[26] A. van den Bruinhorst, S. Raes, S. A. Maesara, M. C. Kroon, A. C. C. Esteves, J. Meuldijk, *Sep. Purif. Technol.* **2019**, *216*, 147–157.

[27] N. H. C. S. Silva, E. S. Morais, C. S. R. Freire, M. G. Freire, A. J. D. Silvestre, *Molecules* **2020**, *25*, 210.

[28] A. P. S. Crema, N. Schaeffer, H. Bastos, L. P. Silva, D. O. Abranches, H. Passos, M. C. Hespanhol, J. A. P. Coutinho, *Hydrometallurgy* **2023**, *215*, DOI 10.1016/j.hydromet.2022.105971.

[29] C. H. J. T. Dietz, M. C. Kroon, M. Di Stefano, M. Van Sint Annaland, F. Gallucci, *Faraday Discuss.* **2018**, *206*, 77–92.

[30] S. J. R. Vargas, G. Pérez-Sánchez, N. Schaeffer, J. A. P. Coutinho, *Green Chem.* **2021**, *23*, 4540–4550.

[31] L. Zhang, J. Li, L. Ji, L. Li, *J. Mol. Liq.* **2021**, *344*, 117729.

[32] M. Lalikoglu, *Biomass Convers. Biorefinery* **2022**, *12*, 1331–1341.

[33] C. C. Chen, Y. H. Huang, S. M. Hung, C. Chen, C. W. Lin, H. H. Yang, *Chem. Eng. J.* **2021**, *424*, 130420.

[34] K. Xin, F. Gallucci, M. Van Sint Annaland, *ACS Sustain. Chem. Eng.* **2022**, *10*, 15284–15296.

[35] Á. Santana-Mayor, B. Socas-Rodríguez, R. Rodríguez-Ramos, A. V. Herrera-Herrera, M. Á. Rodríguez-Delgado, *Anal. Bioanal. Chem.* **2021**, *413*, 1967–1981.

[36] M. A. R. Martins, L. P. Silva, P. S. Jorge, D. O. Abranches, S. P. Pinho, J. A. P. Coutinho, *Eur. J. Pharm. Sci.* **2021**, *156*, 105583.

[37] V. Vanoli, J. Pietrowska, G. de Araujo Lima e Souza, M. E. Di Pietro, F. Briatico Vangosa, A. Mele, F. Castiglione, *ACS Appl. Eng. Mater.* **2024**, *2*, 388–396.

[38] K. Xin, M. van Sint Annaland, *Sep. Purif. Technol.* **2023**, *307*, 122779.

[39] A. R. Harifi-Mood, M. Sarafrazi, H. Akbarzadeh, M. Alinejad, *Sep. Purif. Technol.* **2023**, *306*, 122575.

[40] A. Alhadid, J. Safarov, L. Mokrushina, K. Müller, M. Minceva, *Front. Chem.* **2022**, *10*, 1–8.

[41] A. R. Harifi-Mood, M. Sarafrazi, *J. Environ. Chem. Eng.* **2023**, *11*, 109177.

[42] N. M. Stephens, E. A. Smith, *Langmuir* **2022**, *38*, 14017–14024.

[43] C. Fan, Y. Liu, Y. Shan, X. Cao, *Food Chem.* **2022**, *376*, 131930.

[44] K. W. Miller, N. V. Reo, A. J. M. Schoot Uiterkamp, D. P. Stengle, T. R. Stengle, K. L. Williamson, *Proc. Natl. Acad. Sci. U. S. A.* **1981**, *78*, 4946–4949.

[45] T. R. Stengle, S. M. Hosseini, K. L. Williamson, *J. Solution Chem.* **1986**, *15*, 777–790.

[46] Y. H. Lim, N. Nugara, A. D. King, *Appl. Magn. Reson.* **1995**, *8*, 521–534.

[47] J. Saunavaara, J. Jokisaari, *J. Magn. Reson.* **2006**, *180*, 58–62.

[48] P. Morgado, R. Bonifacio, F. G. Martins, E. J. M. Filipe, *J. Phys. Chem. B* **2013**, *117*, 9014–9024.

[49] Y. H. Lim, A. D. King, *J. Phys. Chem.* **1993**, *97*, 12173–12177.

[50] Y. H. Lim, A. R. Calhoun, A. D. King, *Appl. Magn. Reson.* **1997**, *12*, 555–574.

[51] P. Morgado, L. F. G. Martins, E. J. M. Filipe, *Phys. Chem. Chem. Phys.* **2019**, *21*, 3742–3751.

[52] K. Bartik, M. Luhmer, S. J. Heyes, R. Ottinger, J. Reisse, *J. Magn. Reson. Ser. B* **1995**, *109*, 164–168.

[53] N. Tassali, N. Kotera, C. Boutin, E. Léonce, Y. Boulard, B. Rousseau, E. Dubost, F. Taran, T. Brotin, J.-P. Dutasta, P. Berthault, *Anal. Chem.* **2014**, *86*, 1783–1788.

[54] F. T. Hane, A. Fernando, B. R. J. Prete, B. Peloquin, S. Karas, S. Chaudhuri, S. Chahal, Y. Shepelytskyi, A. Wade, T. Li, B. Deboef, M. S. Albert, *ACS Omega* **2018**, *3*, 677–681.

[55] E. Léonce, J. P. Dognon, D. Pitrat, J. C. Mulatier, T. Brotin, P. Berthault, *Chem. - A Eur. J.* **2018**, *24*, 6534–6537.

[56] F. Castiglione, R. Simonutti, M. Mauri, A. Mele, *J. Phys. Chem. Lett.* **2013**, *4*, 1608–1612.

[57] P. Morgado, K. Shimizu, J. M. S. S. Esperanc, M. Reis, P. N. Rebelo, J. N. C. Lopes, E. J. M. Filipe, *J. Phys. Chem. Lett.* **2013**, *4*, 2758–2762.

[58] G. Saielli, A. Bagno, F. Castiglione, R. Simonutti, M. Mauri, A. Mele, *J. Phys. Chem. B* **2014**, *118*, 13963–13968.

[59] F. Castiglione, G. Saielli, M. Mauri, R. Simonutti, A. Mele, *J. Phys. Chem. B* **2020**, *124*, 6617–6627.

[60] G. Saielli, F. Castiglione, M. Mauri, R. Simonutti, A. Mele, *ChemPhysChem* **2021**, *22*, 1880–1890.

[61] N. J. Brooks, F. Castiglione, C. M. Doherty, A. Dolan, A. J. Hill, P. A. Hunt, R. P. Matthews, M. Mauri, A. Mele, R. Simonutti, I. J. Villar-Garcia, C. C. Weber, T. Welton, *Chem. Sci.* **2017**, *8*, 6359–6374.

[62] C. C. Weber, N. J. Brooks, F. Castiglione, M. Mauri, R. Simonutti, A. Mele, T. Welton, *Phys. Chem. Chem. Phys.* **2019**, *21*, 5999–6010.

[63] M. A. R. Martins, L. P. Silva, N. Schaeffer, D. O. Abranches, G. J. Maximo, S. P. Pinho, J. A. P. Coutinho, *ACS Sustain. Chem. Eng.* **2019**, *7*, 17414–17423.

[64] N. Schaeffer, D. O. Abranches, L. P. Silva, M. A. R. Martins, P. J. Carvalho, O. Russina, A. Triolo, L. Paccou, Y. Guinet, A. Hedoux, J. A. P. Coutinho, *ACS Sustain. Chem. Eng.* **2021**, *9*, 2203–2211.

[65] M. A. R. Martins, E. A. Crespo, P. V. A. Pontes, L. P. Silva, M. Bülow, G. J. Maximo, E. A. C. Batista, C. Held, S. P. Pinho, J. A. P. Coutinho, *ACS Sustain. Chem. Eng.* **2018**, *6*, 8836–8846.

[66] M. S. Syamala, R. J. Cross, M. Saunders, *J. Am. Chem. Soc.* **2002**, *124*, 6216–6219.

[67] D. H. Wu, A. Chen, C. S. Johnson, *J. Magn. Reson. Ser. A* **1995**, *115*, 260–264.

[68] C. J. Jameson, D. N. Sears, S. Murad, *J. Chem. Phys.* **2004**, *121*, 9581–9592.

[69] J. Demarquay, J. Fraissard, *Chem. Phys. Lett.* **1987**, *136*, 314–318.

[70] V. V. Terskikh, I. L. Mudrakovskii, V. M. Mastikhin, *J. Chem. Soc. Faraday Trans.* **1993**, *89*, 4239–4243.

[71] D. J. G. P. Van Osch, C. H. J. T. Dietz, S. E. E. Warrag, M. C. Kroon, *ACS Sustain. Chem. Eng.* **2020**, *8*, 10591–10612.

[72] A. Malik, H. S. Dhattarwal, H. K. Kashyap, *ChemPhysChem* **2022**, *23*, DOI 10.1002/cphc.202200239.

[73] P. Morgado, J. Barras, E. J. M. Filipe, *Phys. Chem. Chem. Phys.* **2020**, *22*, 14736–14747.

[74] A. Moschos, J. Reisse, *J. Magn. Reson.* **1991**, *95*, 603–606.

[75] M. Luhmer, A. Moschos, J. Reisse, *J. Magn. Reson. Ser. A* **1995**, *113*, 164–168.

[76] K. Oikarinen, J. Jokisaari, *Appl. Magn. Reson.* **1995**, *8*, 587–595.

[77] P. Diehl, J. Jokisaari, *J. Magn. Reson.* **1990**, *88*, 660–665.

[78] J. Wolber, S. J. Doran, M. O. Leach, A. Bifone, *Chem. Phys. Lett.* **1998**, *296*, 391–396.

[79] F. P. Pelaquim, A. M. Barbosa Neto, I. A. L. Dalmolin, M. C. da Costa, *Ind. Eng. Chem. Res.* **2021**, *60*, 8607–8620.

5. Characterization of hemp-derived electrocatalysts

The synthetic procedures and the non-NMR characterizations were performed by Dr. Leire Caizán-Juanarena, a former post-doctoral research fellow in the group of Prof. Carlo Santoro from the Department of Materials Science at the University of Milano-Bicocca, Milan.

5.1 Introduction

In the context of the Hydrogen Economy (HE), producing hydrogen through water electrolyzers powered by renewable energy sources is essential for classifying it as green hydrogen. This sustainable hydrogen can be utilized in a wide range of chemical industry reactions, serving both as a reagent and a fuel. Achieving complete decarbonization by 2050 necessitates the widespread use of green hydrogen in hard-to-abate sectors, including for example steel and chemical manufacturing, aviation, and shipping.[1] This would significantly reduce carbon dioxide emissions and facilitate the transition to a sustainable energy system.

Hydrogen also plays a crucial role as fuel in the electrochemical devices known as fuel cells (FCs), which convert hydrogen into valuable electricity.[2] Fuel cells find applications in different sectors such as transportation, aerospace, portable power generation, and industry. Among the various types of fuel cells, low-temperature fuel cells are ideal for portable devices and automotive uses.[3] The most advanced low-temperature fuel cell is the proton exchange membrane fuel cell (PEMFC), which is widely recognized for its high efficiency and stability.[4]

To improve the kinetics of the reactions involved in the fuel cells, precious metal electrocatalysts are employed on both the anode and cathode, with platinum supported on carbon (Pt/C) being the most commonly used catalyst.[5,6] The anodic reaction, known as the hydrogen oxidation reaction (HOR), requires only a low loading of Pt/C. In contrast, the cathodic reaction, called the oxygen reduction reaction (ORR), is significantly slower, necessitating a higher loading of Pt/C and limiting the overall fuel

cell performance.[7–9] Given that platinum is expensive, rare, and classified as a critical element by the European Union, finding suitable replacements is vital for the widespread commercialization of PEMFCs.[10–12]

Over the last 10-15 years, there has been a growing interest in anion exchange membrane fuel cells (AEMFCs),[13–16] which operate in alkaline environments and enable the use of platinum group metal-free (PGM-free) electrocatalysts.[17–20] This shift presents a significant opportunity to improve the sustainability and cost-effectiveness of fuel cell technology. PGM-free electrocatalysts for the oxygen reduction reaction (ORR) are primarily based on carbonaceous materials with high surface area. Recently, researchers have focused on synthetic methods involving the pyrolysis of waste biomass and plastics to produce electrocatalysts with performances comparable to traditional Pt/C catalysts.[21,22]

A key advantage of these pyrolysis processes is their ability to produce conductive biochar with adjustable porosity and pore size distribution.[23,24] By controlling the pyrolysis conditions, the resulting biochar can exhibit tailored porosity that enhances its catalytic activity by improving the accessibility of active sites and facilitating efficient mass transport. Secondary and tertiary treatments can further fine-tune the porosity, making it possible to create electrocatalysts with even more precise structural features.

An example of effective waste biomass valorization for ORR electrocatalysts is lignin, a natural polymer with abundant availability and unique structural properties that offer great potential for enhancing porosity.[25] Waste plastics, such as scrap tires and surgical masks, have also been successfully transformed into electrocatalysts with optimized porosity, further contributing to the development of sustainable alternatives for fuel cell applications.[26,27]

This Chapter investigates the use of hemp stems for producing electrocatalysts, focusing on two components: hemp bast fibers from the outer part of the stem, which are widely used in the textile industry due to their sustainable qualities, and hemp hurds or shives from the woody core, typically considered waste and used for low-value products.[28] Previous research has explored CO_2 adsorption with activated carbon derived from hemp hurds,[29] as well as the synthesis of nitrogen- and cobalt-doped electrocatalysts from hemp powder for the oxygen reduction reaction.[30] In this study, Fe-doped PGM-free ORR electrocatalysts have been prepared for the first time from

pyrolyzed hemp fibers and shives as separate substrates. Different pyrolysis temperatures have been employed, and the resulting electrocatalysts have been characterized using a wide range of physicochemical and electrochemical techniques, such as X-ray diffraction (XRD), Raman spectroscopy, scanning electron microscopy (SEM), energy-dispersive X-ray fluorescence (XRF), and X-ray photoelectron spectroscopy (XPS). The morphology and the porous structure of the hemp-derived materials were thoroughly studied with variable temperature ^{129}Xe NMR spectroscopy. This technique exploits the high sensitivity of xenon gas to the surrounding environment to provide detailed information about the porous structure of solid materials, including pore size distribution, homogeneity, interconnectivity, hierarchy, and pore blocking. This method has previously been applied to a wide range of porous solids, including zeolites,[31–35] mesoporous silica,[36–41] porous polymers,[42–54] and carbon-based materials.[55–60] In this study, we applied ^{129}Xe NMR to the hemp-based materials after every step of the electrocatalyst preparation, from the initial pyrolysis to the final doping with iron. This allowed us to observe the morphological history of the samples throughout the various treatments, providing important correlations between the porous structures of the initial substrates and the final materials. Lastly, we correlated the electrochemical performances of the electrocatalysts with their morphological properties, showing how impactful the porous structure is on the electrocatalytic activity.

5.2 Experimental section

5.2.1 Preparation of hemp-derived electrocatalysts

The overall procedure for the preparation of the electrocatalysts is represented schematically in Figure 5.1. The hemp stem is constituted of two parts that differ in composition and morphology: the outer bast fibers and the inner woody core. These two parts were separated manually in order to isolate the hemp fibers and the hemp shives, which are small wooden pieces derived from the inner woody core. After the separation, both materials were dried at 80 °C overnight before being subjected to one hour of pyrolysis at three different temperatures, 400 °C, 600 °C, and 800 °C, using a

Nabertherm furnace. The heating and cooling rates were controlled at 5 °C/min, and the pyrolysis was performed under a nitrogen atmosphere with a flow rate of 100 cm^3/min.

After pyrolysis, each sample was ground into a fine powder and transferred into a round-bottom flask containing a 1 M potassium hydroxide (KOH) solution diluted in 30-40 mL of ethanol, maintaining a weight ratio of 4:1 between the pyrolyzed material and KOH. The mixture was stirred at 250 rpm overnight in a sealed flask to prevent ethanol evaporation. The following day, ethanol was evaporated on a hot plate set at 80 °C, and the dried carbon-KOH mixture was placed in ceramic boats for additional heat treatment. To prevent any chemical interaction between KOH and the silica boats, nickel strips were used to cover the boats. Carbon powders were then activated, with the aim of enhancing their porosity, by heating at 700 °C for one hour under a controlled N_2 atmosphere (flow rate of 100 cm^3/min). The heating and cooling rates were set to 5 °C/min. After activation, the carbon powder was thoroughly washed with 100 mL of HCl for 10 minutes to neutralize the pH, followed by repeated rinsing with demineralized water under vacuum filtration. To ensure the complete neutralization of the carbon powder, the pH of the final rinsing water was controlled. Finally, the carbon was dried overnight in an oven at 150 °C.

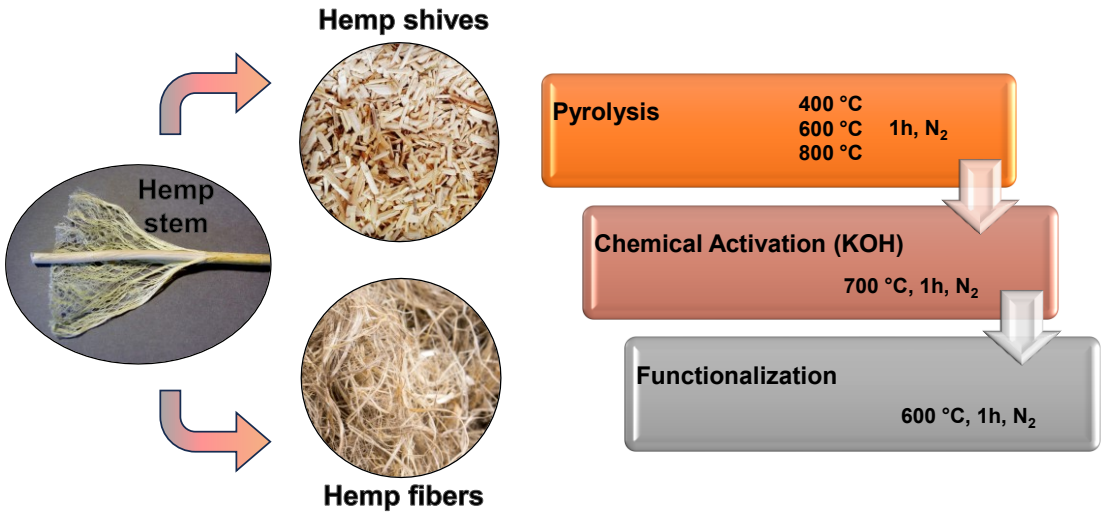

Figure 5.1. Hemp stem-derived substrates, shives and fibers, were used to synthesize electrocatalysts for oxygen reduction reaction (ORR) through three main processes: 1) pyrolysis at three different temperatures (400 °C, 600 °C, and 800 ºC), 2) chemical activation with KOH as the reagent, and 3) functionalization, with iron phthalocyanine (FePc) as a precursor.

To functionalize the six activated carbon samples, each was blended with iron phthalocyanine (FePc) in a 4:1 weight ratio between the carbonaceous material and FePc. The blend was then heat treated for one hour at 600 °C using the same conditions as the two previous heat treatments: 5 °C/min heating and cooling rates, and nitrogen atmosphere with a controlled flow rate of 100 cm^3/min. Functionalized samples are labeled HF400, HF600, and HF800 for hemp fiber-based catalysts, and HS400, HS600, and HS800 for hemp shives, with the numbers referring to the pyrolysis temperature of the initial step.

5.2.2 Non-NMR physicochemical characterization of the electrocatalysts

5.2.2.1 X-ray powder diffraction (XRD)

X-ray powder diffraction (XRD) was performed over a 2θ range of 10° to 90° using a Rigaku Miniflex 600 instrument with a Cu X-ray source to evaluate the crystallinity of the samples.

5.2.2.2 Raman spectroscopy

To analyze the carbonaceous structure of the synthesized electrocatalysts in powder form, we employed Raman spectroscopy using a LabRam system (Jobin Yvon, France). The system utilized a helium-neon laser (λ = 632.8 nm) as the excitation source, with an Olympus BX40 microscope (Japan) to focus the laser on the sample and a silicon-based CCD detector (Sincerity, Jobin Yvon, France) to collect the emitted signals.

5.2.2.3 Scanning electron microscopy (SEM)

Scanning electron microscopy (SEM) images of the synthesized carbonaceous electrocatalysts were captured using a FEI Helios Nanolab 650 instrument.

5.2.2.4 Energy-dispersive X-ray fluorescence (XRF)

The elemental composition of the synthesized electrocatalysts was qualitatively determined by employing the energy-dispersive X-ray fluorescence (XRF) technique,

using a Bruker Artax 200 spectrometer equipped with an X-ray tube with a molybdenum anode.

5.2.2.5 X-ray photoelectron spectroscopy (XPS)

The surface chemistry of all samples was quantitatively analyzed using X-ray photoelectron spectroscopy (XPS) with a Nexsa spectrometer (England), featuring a monochromatic, micro-focused Al Kα X-ray source (photon energy 1486.6 eV). Measurements were conducted under ultra-high vacuum (UHV) conditions, with a base pressure of 5×10^{-10} torr, never exceeding 3×10^{-9} torr.

5.2.2.6 Electrochemical characterization

The electrocatalytic activity of the synthesized samples for the oxygen reduction reaction (ORR) was investigated using a rotating ring disk electrode (RRDE) setup, following a previously reported methodology.[61–63] An ink was prepared by suspending 5 mg of the synthesized electrocatalyst in a solution of 985 µL isopropanol (Alfa Aesar) and 15 µL of Nafion® D-520 (5 wt%, Alfa Aesar). This mixture underwent probe sonication for 10 minutes, followed by bath sonication for 30 minutes at room temperature, resulting in a homogeneous ink. The working electrode was fabricated by drop-casting the electrocatalyst ink on the glassy carbon disk of the RRDE tip. Two different electrocatalyst loadings of 0.2 mg/cm^2 and 0.6 mg/cm^2 were employed.

The experiments were conducted in a three-electrode setup, with a platinum wire as the counter electrode and a saturated calomel electrode (SCE) as the reference electrode. The entire assembly was immersed in an in-house prepared 0.1 M KOH electrolyte saturated with oxygen to simulate oxygen reduction reaction (ORR) activity under alkaline conditions. All potentials in this study were referenced to the reversible hydrogen electrode (RHE) by applying the equation $0.241 + pH \times 0.0591$ to the measured potentials (relative to SCE).

The kinetic parameters of the synthesized electrocatalysts were evaluated using the rotating ring disk electrode (RRDE) methodology, employing a Pine Wave Vortex RDE connected to a Pine bi-potentiostat with 85% IR compensation using an SP-100 Biologic® potentiostat. Linear sweep voltammetry (LSV) was performed to obtain polarization curves at a scan rate of 5 mV/s from 1200 to 0 mV vs RHE, with the ring

potential maintained at approximately 1200 mV vs RHE and the RRDE rotating at 1600 rpm. Before recording the actual LSV curves, the electrocatalyst was conditioned through multiple cyclic voltammograms until a stable current was reached.

Both the disk current (I_{disk}) and ring current (I_{ring}) of the RRDE were measured. The onset potential (E_{onset}) and half-wave potential ($E_{1/2}$) were derived from the I_{disk}, serving as kinetic indicators for comparing the electroactivity of the different synthesized electrode materials. E_{onset}, indicating the threshold potential for initiating the ORR, was determined at -0.1 mA/cm², while $E_{1/2}$ was identified at the peak of the first derivative of the LSV, in accordance with established ORR protocols. The limiting current (I_{limit}), which reflects the maximum current when the electrochemical process is diffusion-controlled, was also evaluated to further distinguish the performance of electrocatalysts with similar E_{onset} and $E_{1/2}$ values.

Additionally, the peroxide yield and the number of transferred electrons (n) during the ORR were estimated using Equations (5.1) and (5.2), respectively, using an RRDE collection efficiency (N) of 0.38. These parameters are crucial for assessing the reaction's selectivity toward a four-electron pathway, minimizing peroxide production.

$$Peroxide\,[\%] = \frac{200 \times \frac{I_{ring}}{N}}{I_{disk} + \frac{I_{ring}}{N}} \tag{5.1}$$

$$n = \frac{4I_{disk}}{I_{disk} + \frac{I_{ring}}{N}} \tag{5.2}$$

5.2.3 ^{129}Xe NMR spectroscopy

Samples for ^{129}Xe NMR spectroscopy were prepared by inserting a small amount of material (0.1-0.15 g) in a thick wall NMR tube with 10 mm outer diameter and 8 mm inner diameter. The tube was connected to a Schlenk line and degassed under a dynamic vacuum at a pressure of 6.0×10^{-2} torr for at least six hours. Isotopically enriched xenon gas (86.6% ^{129}Xe isotopic enrichment) was quantitated by inserting it into a portion of the line with known volume and measuring its pressure with an inline pressure gauge. The gas was then brought into contact with the NMR tube and trapped inside by freezing with liquid nitrogen. Lastly, the tube was flame-sealed while keeping the gas

frozen. For all the samples, the nominal xenon pressure inside the tube was between 2.5-3 bar.

^{129}Xe NMR spectra were acquired on a Bruker Avance 500 spectrometer operating at a Larmor frequency of 500.13 MHz for ^{1}H, corresponding to 139.09 MHz for ^{129}Xe, equipped with a double resonance direct observe broadband (BBO) probe. The free xenon gas peak, visible in the spectra, was set to 0 ppm and used as an internal chemical shift reference. Spectra were acquired with a relaxation delay of 15 s and a number of scans between 1024 and 4096 to obtain a good signal-to-noise ratio. Measurements were performed every 20 K in the temperature range between 238 K and 298 K. The temperature was controlled with a Bruker BVT3000 variable temperature unit with an uncertainty of 0.1 K. Low-temperature experiments were performed by connecting a liquid nitrogen evaporator to the NMR probe. The evaporator was also controlled using the BVT3000 unit.

5.3 Results and discussion

5.3.1 Synthesis of electrocatalysts

The synthesis of electrocatalysts was successfully conducted at three pyrolysis temperatures (400 °C, 600 °C, and 800 °C) using two types of substrates: hemp fibers and shives. For the hemp fibers, the pyrolysis yields were 29.7%, 22.6%, and 23.2% at each respective temperature. In contrast, the yields for hemp shives were slightly higher, at 33.5%, 27.7%, and 26.0%. The rates of chemical activation varied significantly based on the substrate type; for hemp fibers, the activation rates were 20.1%, 29.4%, and 20.5% at 400 °C, 600 °C, and 800 °C, respectively. For hemp shives, the rates were notably higher, measuring 47.2%, 54.7%, and 57.5% under the same temperature conditions.

5.3.2 Non-NMR physicochemical characterization of electrocatalysts

5.3.2.1 Structural characterization

The XRD patterns for electrocatalysts derived from hemp shives and fibers are shown in Figure 5.2a and 5.2b, respectively.

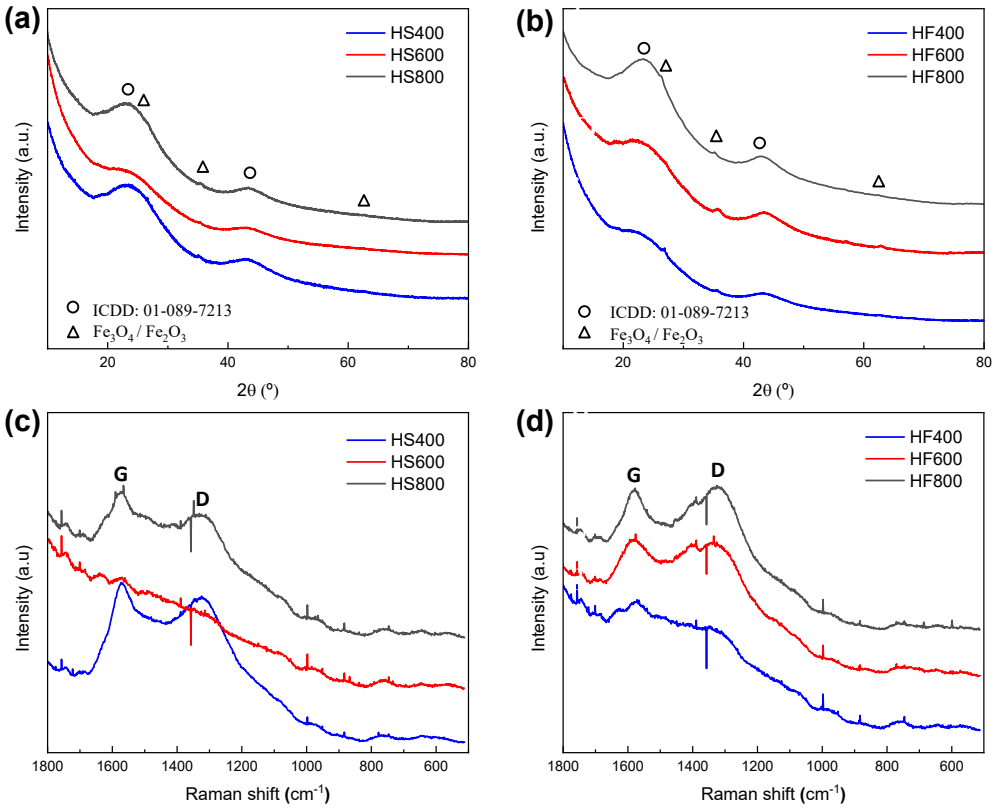

Figure 5.2. (a, b) XRD patterns of the synthesized hemp-derived electrocatalysts. The circles denote the peaks at 24° and 42°, attributed to the (002) and (101) crystallographic planes of graphite. The triangles indicate the peaks at 27°, 34°, and 61°, associated with iron oxide in the magnetite (Fe_3O_4) and/or hematite (Fe_2O_3) forms. (c, d) Raman spectra of the electrocatalysts. The G and D bands at 1575 cm^{-1} and 1320 cm^{-1}, respectively, are indicated.

Each sample displays two broad peaks at approximately 24° and 42°, corresponding to the (002) and (101) crystallographic planes of graphite (ICDD: 01-089-7213), which indicates the distorted structure of the graphitic matrix. Additionally,

smaller peaks at 27°, 34°, and 61° are identified, attributed to iron oxide in the forms of magnetite (Fe_3O_4) and/or hematite (Fe_2O_3). The presence of iron in the amorphous carbon matrix of the electrocatalysts has been confirmed by other characterization techniques (see Section 5.3.2.3).

The Raman spectra of the electrocatalysts derived from hemp shives and fibers are presented in Figure 5.2c and 5.2d, respectively. The spectra exhibit typical signals for carbon powder in the first-order region: the G band around 1575 cm^{-1}, associated with the bond stretching of sp^2 carbon atoms in both rings and chains, and the D band near 1320 cm^{-1}, which relates to the breathing modes of sp^2 atoms in rings.[64] The ratio between the intensities of the D and G peaks, I_D/I_G, provides insights into structural disorder and defects in carbon-based materials. Electrocatalysts derived from hemp shives showed I_D/I_G values between 0.93 and 0.94, while those from hemp fibers ranged from 0.88 to 1.00. These values indicate a lower number of defects compared to ratios above one, which would suggest destructive grain boundaries and edges caused by micropore formation, cracks, the presence of heteroatoms like iron oxides, or atomic vacancies, as reported in other studies.[65] These findings are consistent with the amorphous carbon signals and iron oxide peaks identified in the XRD spectra. Overall XRD and Raman spectroscopy demonstrate that these electrocatalysts have disordered structures that include a non-negligible amount of Fe heteroatoms. These features are potentially helpful for the ORR catalytic activity.

5.3.2.2 Morphological characterization

The morphological features of the electrocatalysts, including particle size distribution, shape, surface roughness, and micrometric porosity, were analyzed using SEM. Figure 5.3 shows the backscattered electrons images of the electrocatalysts derived from the two different substrates pyrolyzed at 400 °C, 600 °C, and 800 °C, with a magnification of 2500×. For each sample, the particles have sizes in the range of 5-50 µm, with the electrocatalysts derived from hemp fibers having overall slightly larger particles compared to those derived from hemp shives. In terms of particle shape, those pyrolyzed at 400 °C display a more rounded morphology, forming rough spheres. In contrast, particles pyrolyzed at 600 °C and 800 °C for both substrate types exhibit a more elongated polyhedral shape. SEM images reveal noticeable surface roughness and

macroporosity in all samples. The rounded particles feature multiple cavities and large surface pores, while the elongated particles display polygonal faces, straight edges, sharp vertices, and elongated pores evident in cross-sections.

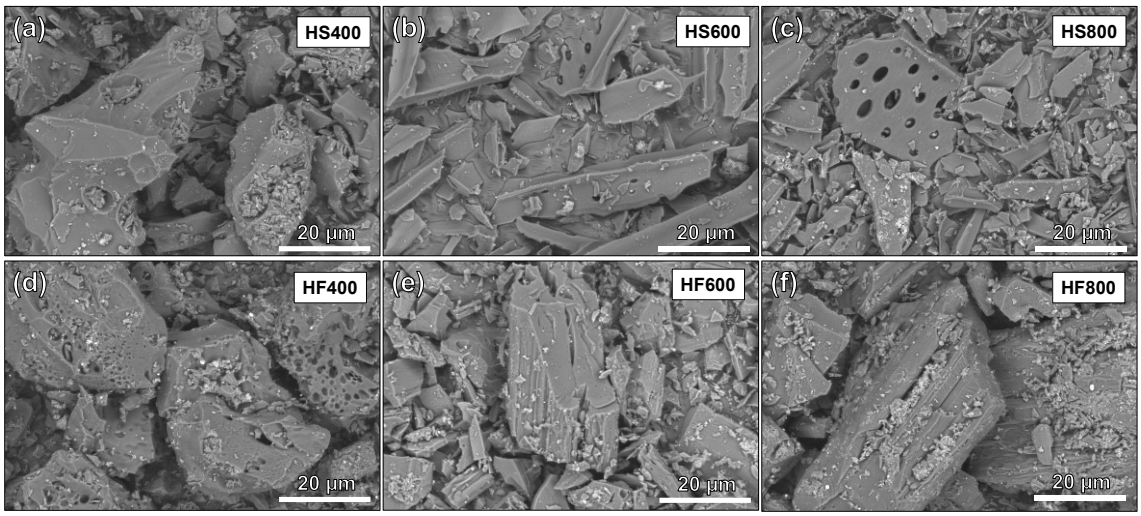

Figure 5.3. Backscattered electrons SEM images of the synthesized electrocatalysts derived from hemp shives and hemp fibers pyrolyzed at 400 °C, 600 °C, and 800 °C. The images have a magnification of 2500×.

5.3.2.3 Surface chemistry

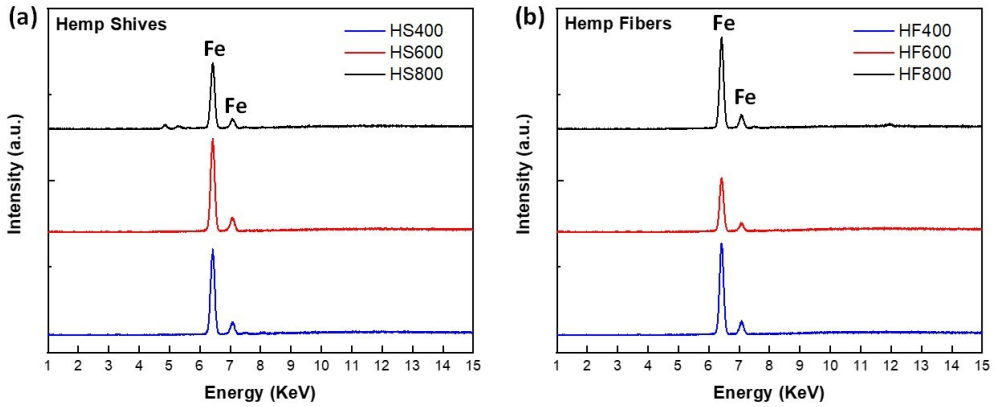

Figure 5.4. XRF spectra of hemp shives- and hemp fibers-derived electrocatalysts in the range of 1-15 keV.

As a first approach, we evaluated the surface chemistry of the prepared electrocatalysts with XRF. The resulting spectra, shown in Figure 5.4, indicate that Fe is the only metal present in the electrocatalysts. The presence of iron is due to the use of FePc in the functionalization step.

The contents of various elements such as carbon (C), nitrogen (N), oxygen (O), and iron (Fe) were analyzed in detail with XPS. Table 5.1 shows the overall weight percentages of each of the elements. It can be seen that hemp shives-derived samples are slightly richer in carbon compared to those derived from hemp fibers. On the other hand, hemp fiber-based electrocatalysts have slightly higher nitrogen and iron contents. Lastly, in both series of samples, the nitrogen weight percentage decreases with increasing the initial pyrolysis temperature.

Table 5.1. Weight percentages of carbon, oxygen, nitrogen, and iron in the prepared electrocatalysts, calculated with XPS.

Sample	C [%]	O [%]	N [%]	Fe [%]
HS400	84.8	10.2	4.4	0.5
HS600	87.7	8.3	3.5	0.5
HS800	85.6	10.9	3.1	0.4
HF400	82.6	11.7	4.8	0.9
HF600	83.1	11.6	4.5	0.8
HF800	82.0	13.2	4.1	0.7

5.3.2.4 Electrochemical activity

The electrochemical activity of the synthesized electrocatalysts for the oxygen reduction reaction was determined with the RRDE method in an alkaline medium (oxygen-saturated 0.1 M KOH). Table 5.2 summarizes the parameters obtained from the measurements of all the studied catalysts.

Table 5.2. Kinetic parameters determining the electrochemical activity of the synthesized electrocatalysts. The measurements were conducted with two different electrocatalyst loadings of 0.2 mg/cm^2 and 0.6 mg/cm^2.

	0.2 mg/cm^2					**0.6 mg/cm^2**				
Sample	E_{onset} **[V]**	$E_{1/2}$ **[V]**	J_{limit} **[mA/cm^2]**	**Peroxide [%]**	**e$^-$ [*n*]**	E_{onset} **[V]**	$E_{1/2}$ **[V]**	J_{limit} **[mA/cm^2]**	**Peroxide [%]**	**e$^-$ [*n*]**
HS400	1.00	0.9	-2.9	21	3.6	0.98	0.90	-3.5	12	3.77
HS600	1.01	0.90	-2.9	12	3.8	1.02	0.91	-3.0	7	3.85
HS800	1.01	0.89	-3.9	25	3.5	1.00	0.90	-5.0	15	3.7
HF400	1.00	0.91	-2.7	17	3.65	0.98	0.92	-3.5	10	3.8
HF600	0.99	0.90	-2.7	21	3.6	0.96	0.90	-4.2	9	3.82
HF800	1.00	0.90	-3.3	23	3.55	1.00	0.92	-3.3	14	3.72

Figure 5.5 illustrates the electrochemical performance of electrocatalysts derived from hemp shives pyrolyzed at three distinct temperatures, tested at a loading of 0.6 mg/cm^2. The HS600 sample (red curves in Figure 5.5) exhibits the highest onset potential (E_{onset}) and half-wave potential ($E_{1/2}$) at 1.02 V and 0.91 V vs RHE, respectively. While HS800 achieves the best J_{limit} of approximately -5 mA/cm^2, it also results in the greatest peroxide production (15%) and the lowest electron transfer efficiency (3.7). Notably, HS600 produces the least peroxide while maintaining a high number of transferred electrons. Peroxide is an unwanted byproduct, as it can be harmful to the integrity of the cell membrane. The expected limiting current density is around -6 mA/cm^2. However, the higher limiting current density observed in the synthesized electrocatalysts indicates that complete 4-electron conversion is not always possible, leading to peroxide formation. This suggests the presence of various active sites, including those that facilitate direct 4-electron transfer, those that produce 2-electron transfers, and those that convert intermediates into final products.

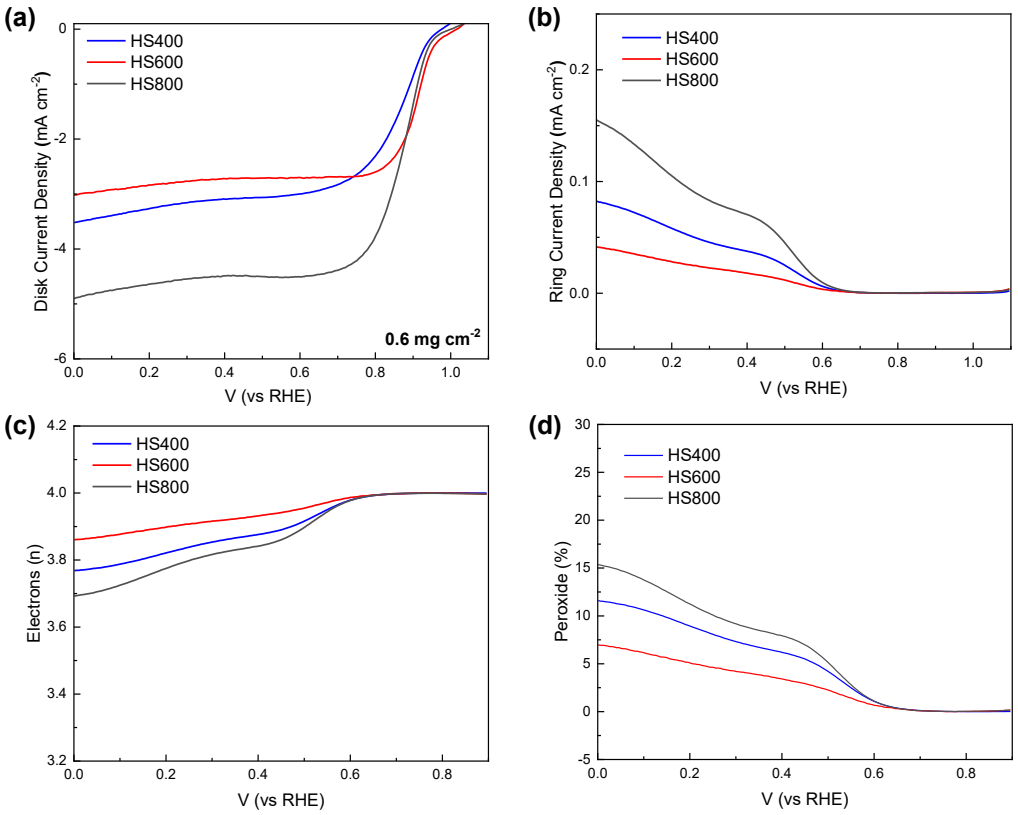

Figure 5.5. RRDE measurements of the prepared hemp shives-based electrocatalysts in oxygen-saturated 0.1 M KOH with an electrocatalyst loading of 0.6 mg/cm^2. (a) Linear sweep voltammetry disk current densities obtained at a scan rate of 5 mV/s, (b) ring current densities, (c) number of electrons transferred during the oxygen reduction reaction, and (d) peroxide yield.

Figure 5.6 shows similar results obtained for electrocatalysts derived from hemp fibers. Here, the electrocatalyst HF800 (black curves) achieves the highest E_{onset} and $E_{1/2}$ at 1.00 V and 0.92 V vs RHE, respectively. In terms of other parameters, HF600 displays the best J_{limit} at -4.2 mA/cm^2. However, this value is still above the expected limiting current density of -6 mA/cm^2, indicating a mixed reaction regime even with fiber-based catalysts, which leads to a non-zero peroxide production.

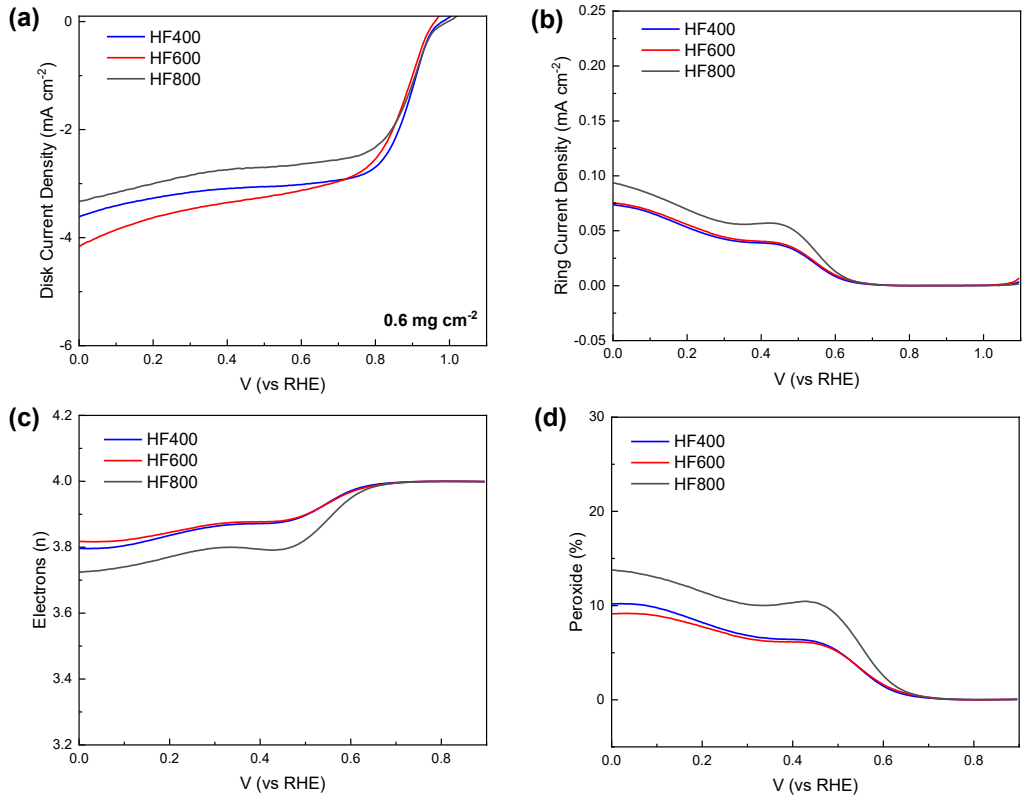

Figure 5.6. RRDE measurements of the prepared hemp fibers-based electrocatalysts in oxygen-saturated 0.1 M KOH with an electrocatalyst loading of 0.6 mg/cm^2. (a) Linear sweep voltammetry disk current densities obtained at a scan rate of 5 mV/s, (b) ring current densities, (c) number of electrons transferred during the oxygen reduction reaction, and (d) peroxide yield.

Figure 5.7 and Figure 5.8 display the performance parameters for electrocatalysts derived from hemp shives and hemp fibers, respectively, with a loading of 0.2 mg/cm^2 in the RRDE. Overall, even with a lower loading the E_{onset} and $E_{1/2}$ values remain rather similar (see Table 5.2). However, with these catalysts the peroxide production increases by 5-12%, and the number of transferred electrons decreases, indicating that the 4-electron reaction pathway is less likely to occur. It has already been reported in the literature that higher loadings can reduce peroxide production due to the thicker electrocatalyst layer, so these results are in line with expectations.

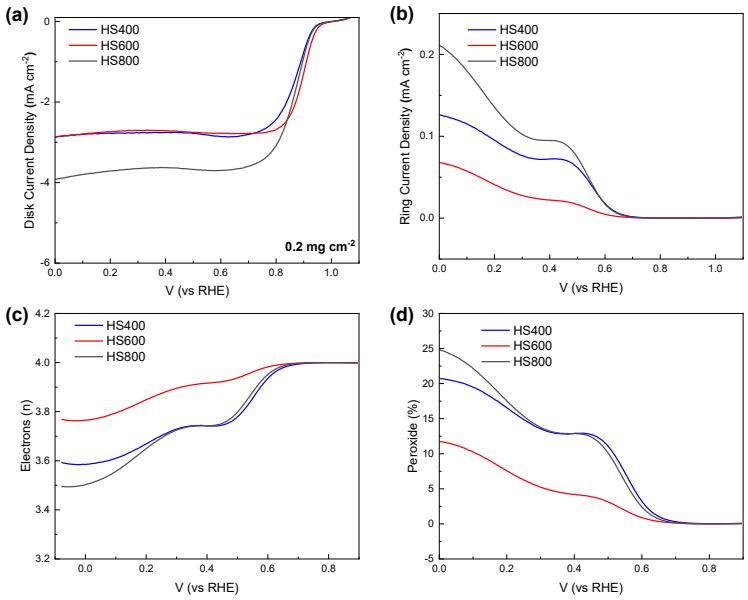

Figure 5.7. RRDE measurements of the prepared hemp shives-based electrocatalysts in oxygen-saturated 0.1 M KOH with an electrocatalyst loading of 0.2 mg/cm^2. (a) Linear sweep voltammetry disk current densities obtained at a scan rate of 5 mV/s, (b) ring current densities, (c) number of electrons transferred during the oxygen reduction reaction, and (d) peroxide yield.

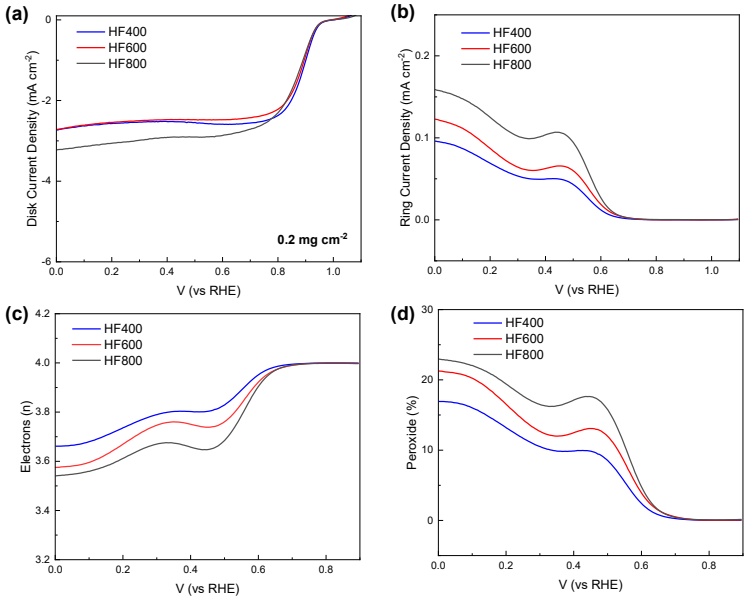

Figure 5.8. RRDE measurements of the prepared hemp fibers-based electrocatalysts in oxygen-saturated 0.1 M KOH with an electrocatalyst loading of 0.2 mg/cm^2. (a) Linear sweep voltammetry disk current densities obtained at a scan rate of 5 mV/s, (b) ring current densities, (c) number of electrons transferred during the oxygen reduction reaction, and (d) peroxide yield.

In terms of electrochemical properties, the results were consistent with those reported in the literature for other electrocatalysts under similar conditions, including alkaline media, a loading rate of 0.6 mg/cm^2, and a rotating speed of 1600 rpm. Table 5.3 provides a summary of the key electrocatalytic parameters obtained from LSV curves in various studies, with the current work standing out for having higher E_{onset} and $E_{1/2}$ values compared to others. Additionally, the values are within the range of 20% Pt/C catalysts. Peroxide production is also significantly lower compared to other studies, which is beneficial for maintaining the integrity of the cell's membranes. The limiting current density of the synthesized electrocatalysts, in absolute value, is below 6 mA/cm^2, similar to most studies, though on the lower side (3 to 5 mA/cm^2). However, the number of transferred electrons was in the higher range, between 3.6 and 3.8.

Table 5.3. Performance of waste-derived electrocatalysts for oxygen reduction reaction in alkaline media at a loading of 0.6 mg/cm^2 and a rotating speed of 1600 rpm.

Sample	E_{onset} [V]	$E_{1/2}$ [V]	J_{limit} [mA/cm^2]	Peroxide [%]	e$^-$ [n]	Reference
HS600	1.02	0.91	-3.0	7	3.8	This Chapter
HS800	1.00	0.90	-5.0	15	3.7	This Chapter
HF600	0.96	0.90	-4.2	9	3.82	This Chapter
Fe-N-C$_{pyro\text{-}tea}$*	0.94	0.95	-3	25	3.5	[66]
CIGF_450	0.94	0.89	-3.4	10	3.8	[65]
L_Fe	0.94	0.87	-4.5	25	3.5	[25]
ACP	0.94	0.85	-3.1	49	3	[61]
Co/NHPC-90**	-	0.83	-5.4	-	-	[30]
FeNC_P	0.88	0.63	-4.6	20	3.5	[67]
20% Pt/C	-	0.83	-5.1	15	-	[65]

**Rotating speed of 900 rpm. **Loading not specified.*

5.3.3 ^{129}Xe NMR spectroscopy

To investigate the porous structure of the materials obtained at every step of the electrocatalysts preparation, we performed variable temperature ^{129}Xe NMR measurements on the pyrolyzed, activated, and functionalized hemp shives- and fibers-derived materials.

5.3.3.1 Pyrolyzed hemp shives and fibers

First, we analyzed the porous structure of the starting materials: hemp shives and fibers pyrolyzed at different temperatures. Figure 5.9 shows the ^{129}Xe NMR spectra of shives and fibers pyrolyzed at 400 °C, acquired every 20 K in the range between 238 K and 298 K.

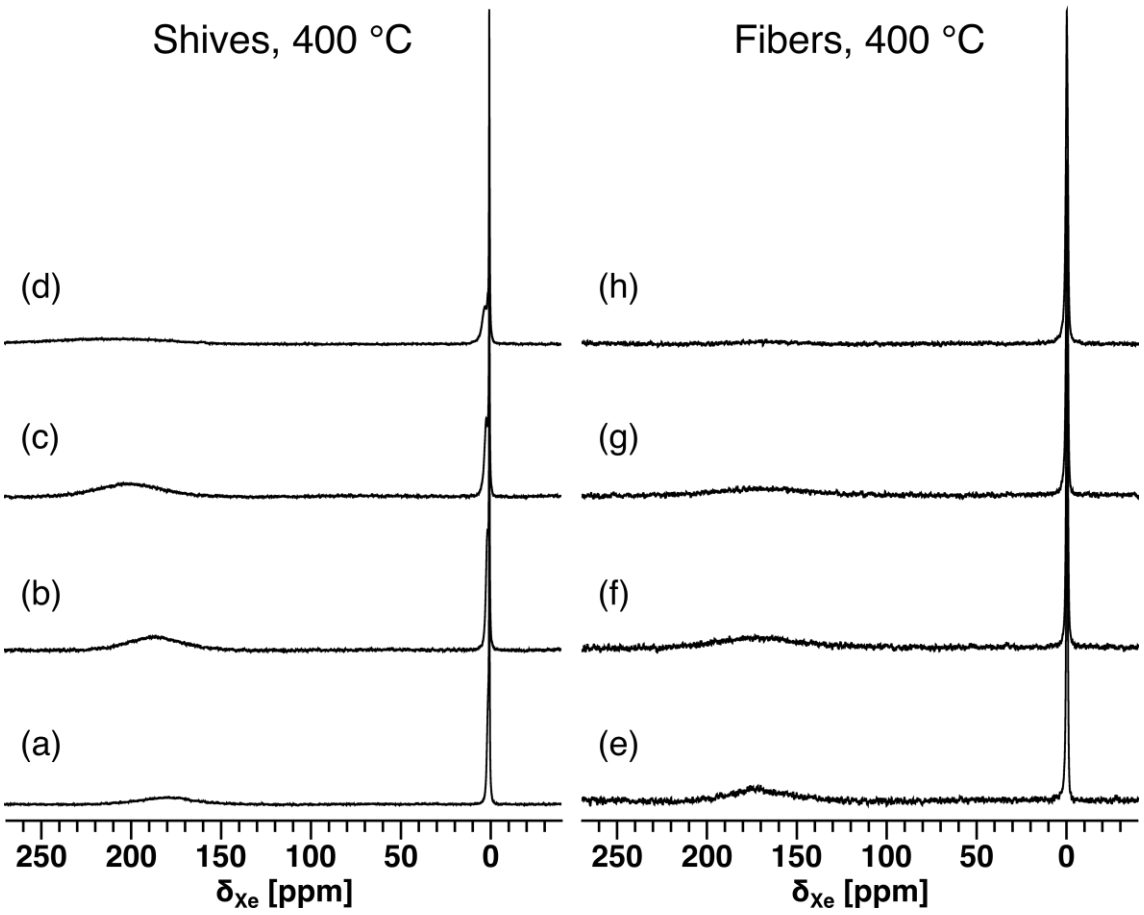

Figure 5.9. ^{129}Xe NMR spectra of hemp shives (left) and hemp fibers (right) pyrolyzed at 400 °C, acquired at (a, e) 298 K, (b, f) 278 K, (c, g) 258 K, and (d, h) 238 K.

The spectra show the intense and sharp free xenon gas peak, set to 0 ppm and used as an internal chemical shift reference, along with a broad and very weak resonance centered roughly in the range between 170 ppm and 180 ppm. This peak derives from xenon sorbed into the porous structure of the pyrolyzed materials. Its low relative intensity indicates that the porosity of these materials is overall very low. Extracting the average dimensions of the pores of carbonaceous materials from the ^{129}Xe chemical shifts is difficult due to their disordered and heterogeneous structures (see Section 1.4.3.3). However, the pores can be qualitatively estimated to be in the microporous range, i.e. with dimensions less than 2 nm, based on other results reported in the literature.[58] Notably, in the spectra of pyrolyzed hemp shives the signal of the free xenon gas has a shoulder peak at roughly 2 ppm. This peak is attributed to xenon atoms exchanging between free gas and large macroporous spaces or surface indentations, where they are only slightly more confined than free gas.[68] The shoulder peak broadens and becomes less intense with decreasing temperature since the dynamics of xenon are slowed down and the atoms are allowed to probe slightly different spaces in the NMR time scale, spending more time in the adsorbed state compared to the free state.

Figure 5.10 illustrates the results for the materials pyrolyzed at 600 °C. The spectra of pyrolyzed fibers show that these materials do not have any significant porous structure in the dimensional range probed by xenon NMR. Thus, these materials are similar to the fibers pyrolyzed at 400 °C. Hemp shives, on the other hand, have a different morphology compared to those pyrolyzed at 400 °C. In the room temperature spectrum, the intense peak centered at roughly 175 ppm reveals the presence of a porous structure generated by the thermal treatment. By lowering the temperature to 258 K, and especially 238 K, the peak splits into two broad resonances. This indicates that the sample has two different populations of pores which become distinguishable only when the xenon dynamics are slowed down by the low temperature. At 278 K and higher, xenon atoms exchange rapidly between the two different populations, and this results in a single average NMR signal. Based on the chemical shifts of the peaks, which are 170 ppm and 221 ppm, respectively, these signals can be qualitatively attributed to micropores with different sizes. In addition to that, the free gas peaks in the spectra of hemp shives have shoulder peaks similar to those visible in Figure 5.9. This indicates

that the large macroporous spaces are retained even when the pyrolysis is performed at 600 °C.

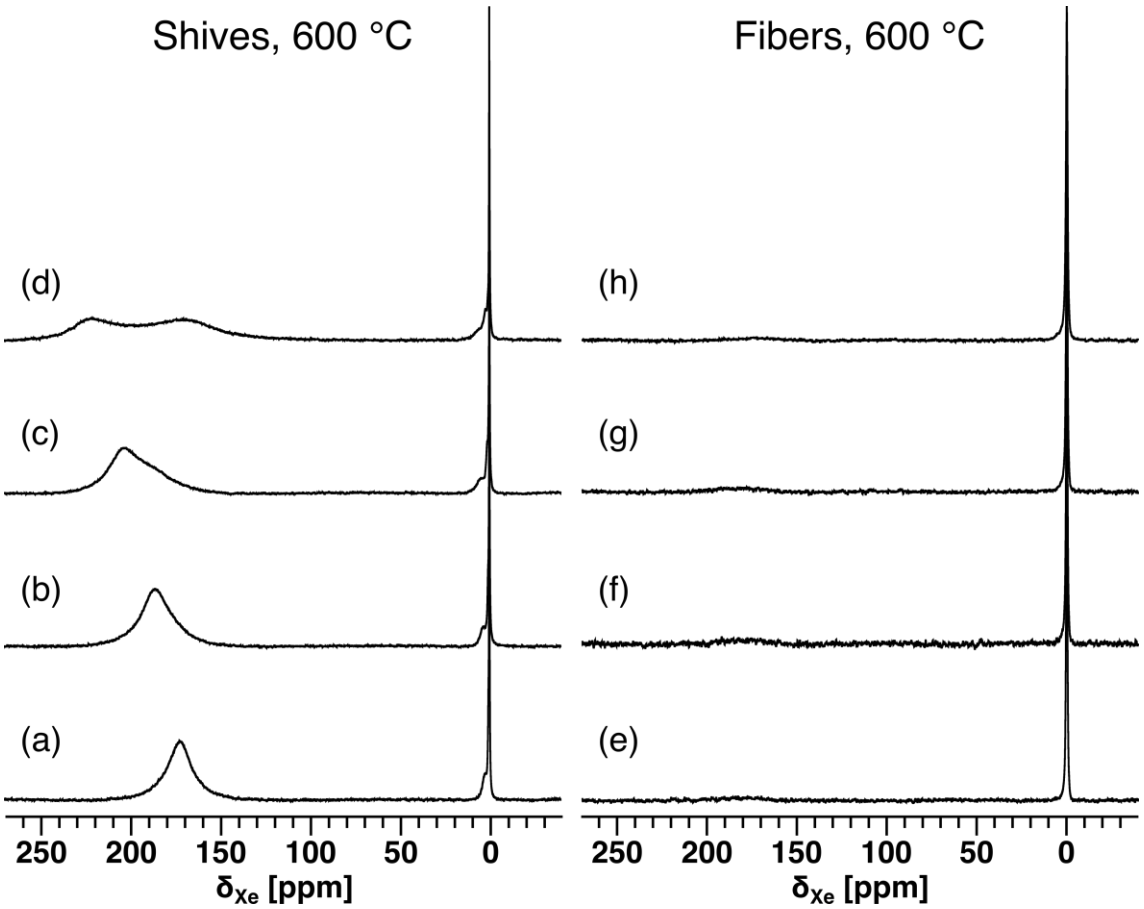

Figure 5.10. ^{129}Xe NMR spectra of hemp shives (left) and hemp fibers (right) pyrolyzed at 600 °C, acquired at (a, e) 298 K, (b, f) 278 K, (c, g) 258 K, and (d, h) 238 K.

Interestingly, the morphology of the shives and fibers is completely changed when the pyrolysis is performed at 800 °C, as clearly visible in the spectra represented in Figure 5.11. The ^{129}Xe NMR spectrum of hemp fibers acquired at 298 K displays two partially superimposed peaks that suggest the presence of two different populations of pores. The presence of a bimodal porous structure is confirmed by low-temperature measurements in which the separation between the peaks is increased along with their intensities relative to the free gas peak. On the other hand, the hemp shives pyrolyzed at 800 °C do not show any significant micro- and mesopores (dimensions between 2 nm and 50 nm), similar to the fibers pyrolyzed at 400 °C and 600 °C. Only large macroporous indentations are visible at 258 K and 238 K, analogous to the lower

pyrolysis temperatures. These results indicate that either the high processing temperature breaks down the pores, increasing their sizes to the point where xenon in the middle of the pores cannot be distinguished from free xenon gas (i.e. big macropores such as those visible in the SEM images in Figure 5.3), or that the small pores are obstructed by ashes or other residues formed during the pyrolysis.

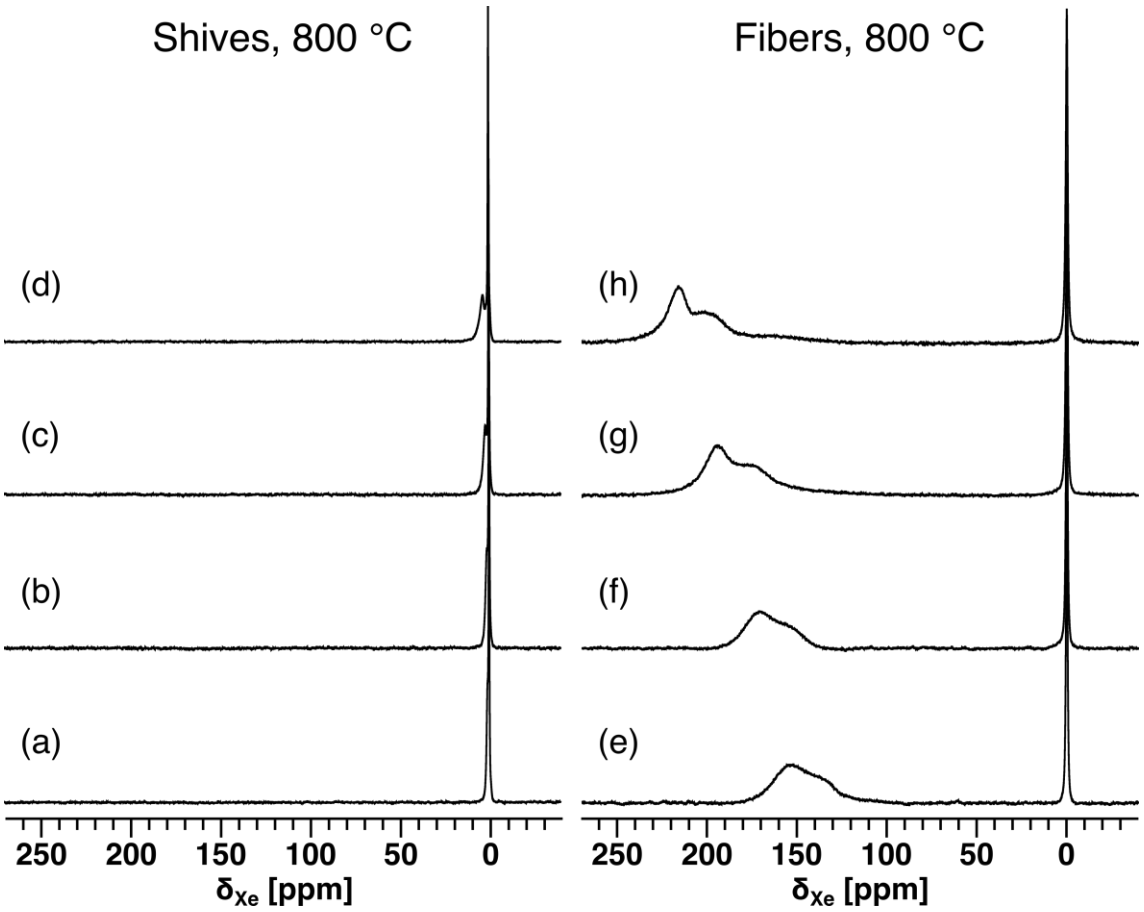

Figure 5.11. ^{129}Xe NMR spectra of hemp shives (left) and hemp fibers (right) pyrolyzed at 800 °C, acquired at (a, e) 298 K, (b, f) 278 K, (c, g) 258 K, and (d, h) 238 K.

To verify whether the pores were blocked by the waste of the thermal treatment, we analyzed the pyrolyzed hemp shives after repeated washing with distilled water under vacuum filtration. Figure 5.12 shows a comparison between the ^{129}Xe NMR spectra of unwashed and washed hemp shives. No downfield peaks appear in the spectra of the washed materials, indicating that, even in this case, there are no meso- or micropores. Notably, the shoulder of the free gas peak becomes more resolved after washing, suggesting that some ashes or residues are indeed removed, but only from the

large macroporous spaces. Overall, these results reveal that the pyrolysis of hemp shives at 800 °C does not generate a micro- or mesoporous structure, but instead, it creates large macroporous spaces with sizes on the order of microns, as demonstrated by SEM (Figure 5.3).

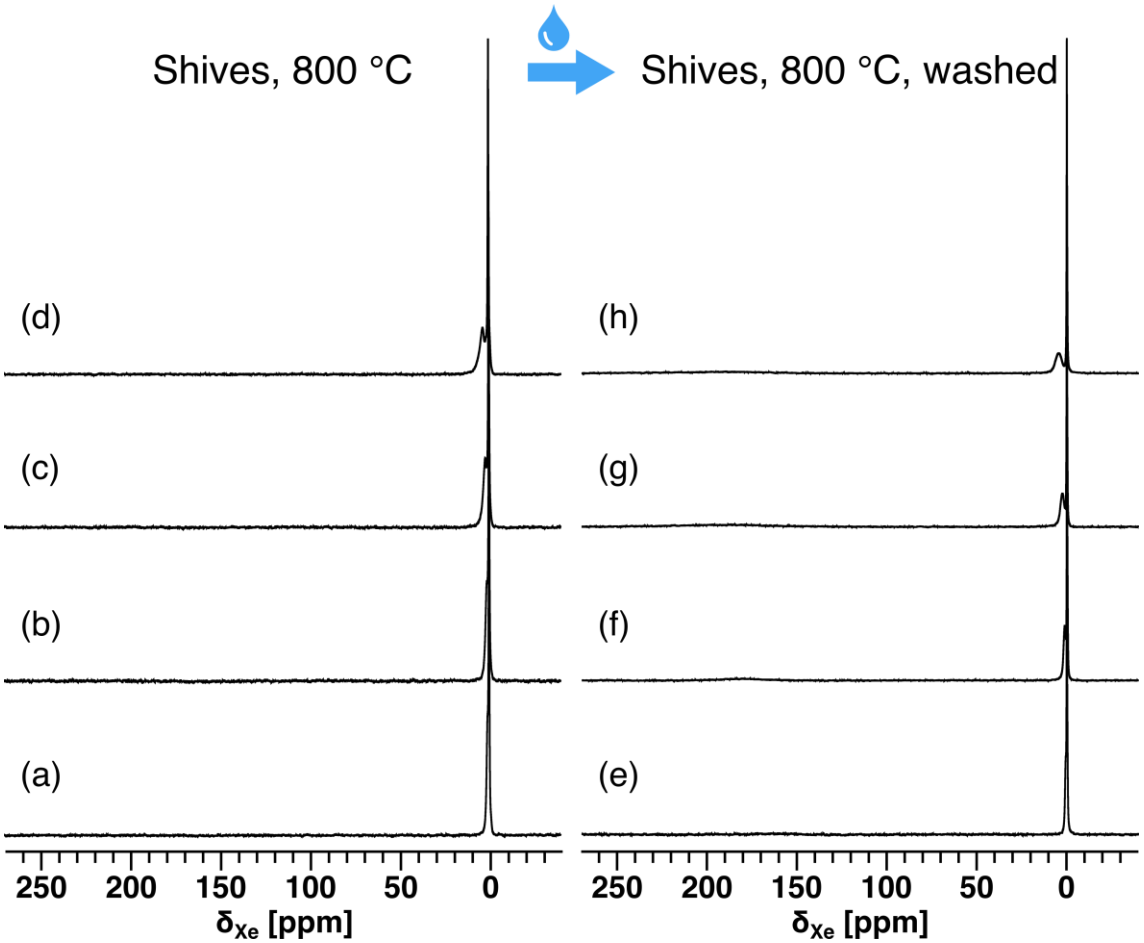

Figure 5.12. ^{129}Xe NMR spectra of hemp shives pyrolyzed at 800 °C, before (left) and after (right) washing with distilled water. The spectra were acquired at (a, e) 298 K, (b, f) 278 K, (c, g) 258 K, and (d, h) 238 K.

5.3.3.2 Activated materials

The effect of the activation with KOH on morphology was studied by analyzing some of the activated samples with ^{129}Xe NMR and comparing the spectra with those of the corresponding materials after pyrolysis. The results for the hemp fibers pyrolyzed at 400 °C are illustrated in Figure 5.13. The differences between the spectra on the left and on

the right demonstrate that the materials have radically different morphologies. Two different resonances at 110 ppm and 133 ppm are visible in the spectrum of activated fibers acquired at 298 K (Figure 5.13e). The chemical shift of these peaks increases with decreasing temperature, reaching 161 ppm and 182 ppm at 238 K, respectively (Figure 5.13h). No additional peaks and no peak splitting are observed upon lowering the temperature. This indicates that the activation with KOH generates a bimodal porous structure in the pyrolyzed hemp fibers. The two peaks are distinguishable even at room temperature, as opposed to the spectra represented in Figure 5.10 in which there is a single exchange signal at 298 K. Thus, we can conclude that there is a significant segregation between the two different populations of pores, as even at room temperature xenon gas is not able to exchange rapidly between them on the NMR time scale.

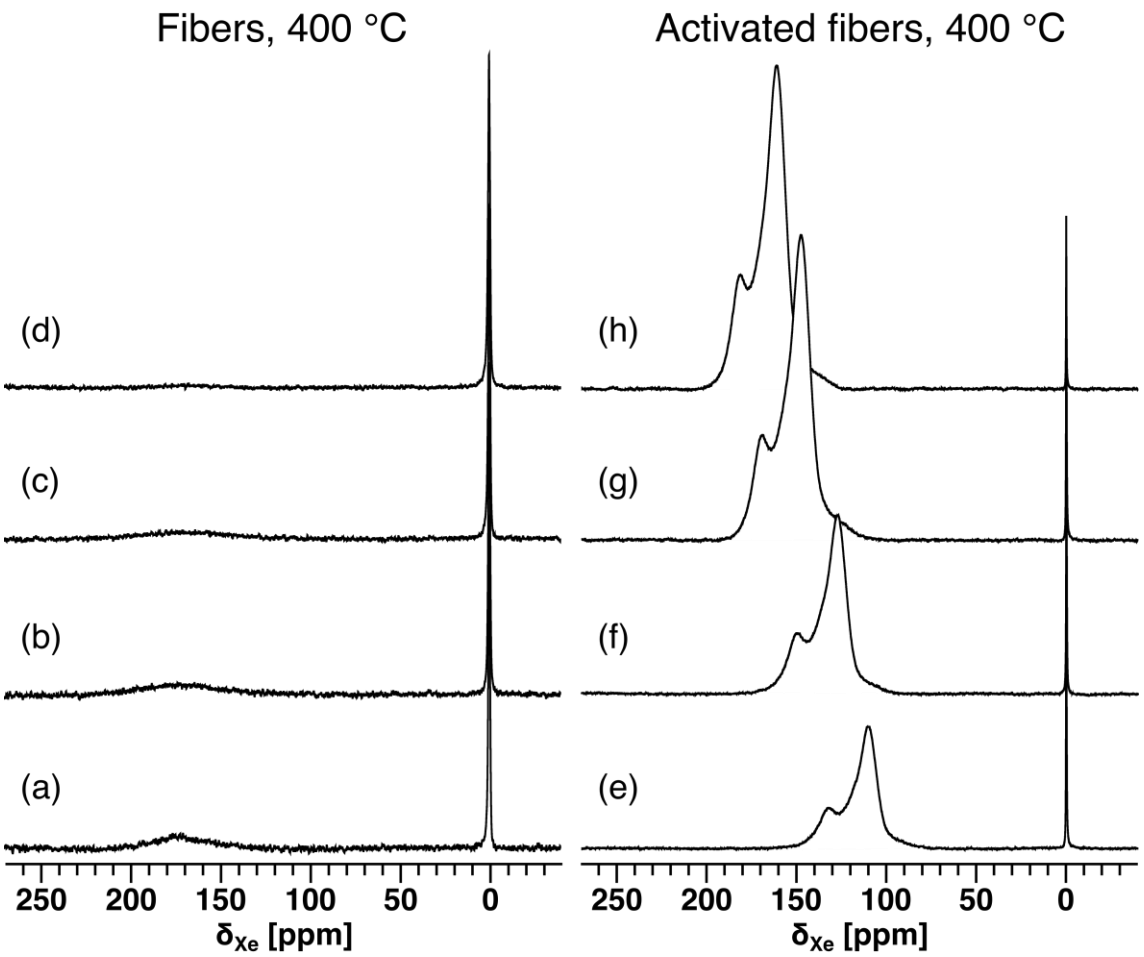

Figure 5.13. ^{129}Xe NMR spectra of hemp fibers with a pyrolysis temperature of 400 °C, before (left) and after (right) activation with KOH. The spectra were acquired at (a, e) 298 K, (b, f) 278 K, (c, g) 258 K, and (d, h) 238 K.

The activation with KOH generates a different porous structure in the fibers treated at 600 °C, as can be seen from the ^{129}Xe NMR spectra represented in Figure 5.14. Here, the spectrum at 298 K shows a single resonance with a chemical shift of 97 ppm that increases almost linearly with decreasing temperature up to 133 ppm at 238 K. Thus, contrary to the fibers pyrolyzed at 400 °C, in this case, the activation process generates a rather homogeneous porous structure with a monomodal distribution of pores estimated to be roughly in the mesopore range based on the chemical shift.[58]

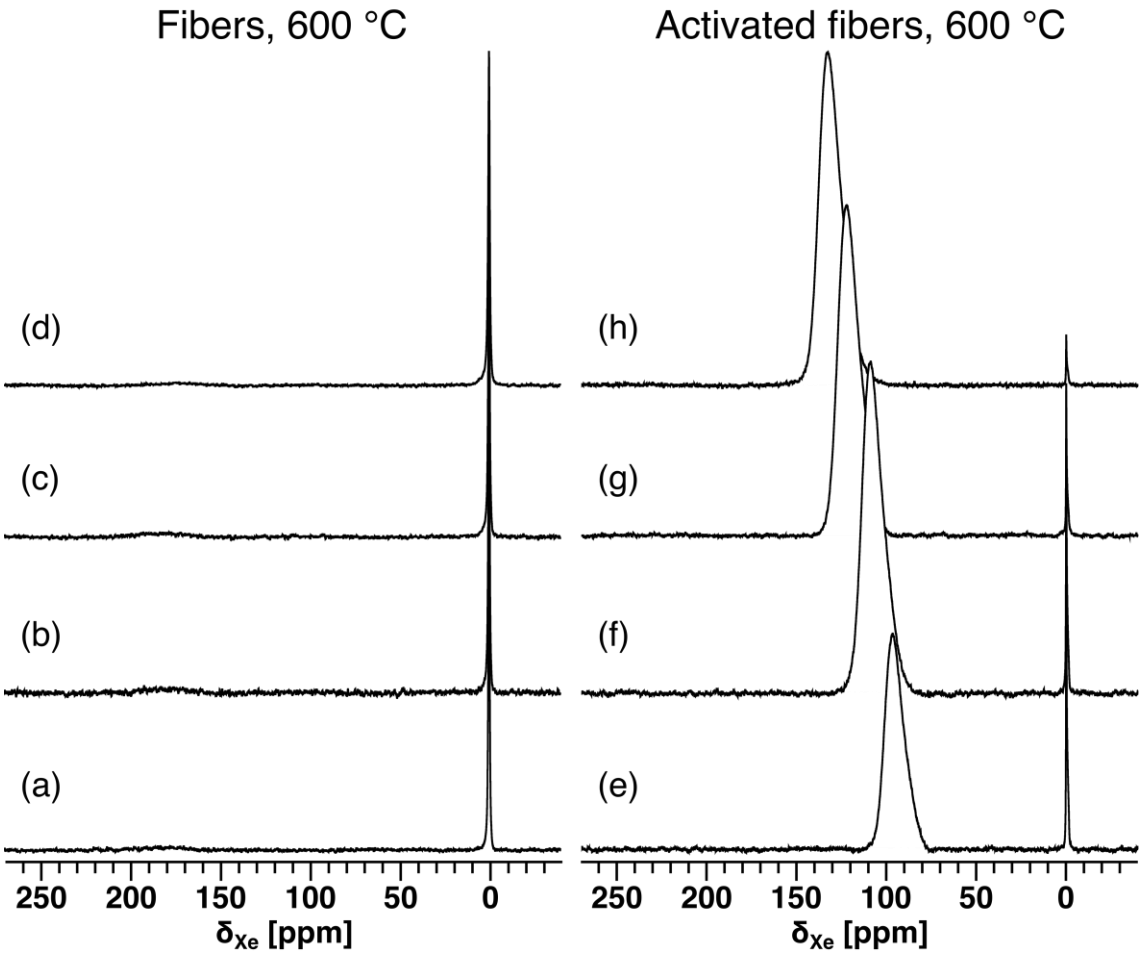

Figure 5.14. ^{129}Xe NMR spectra of hemp fibers with a pyrolysis temperature of 600 °C, before (left) and after (right) activation with KOH. The spectra were acquired at (a, e) 298 K, (b, f) 278 K, (c, g) 258 K, and (d, h) 238 K.

Interestingly, a similar morphology is obtained after the activation of hemp shives pyrolyzed at 600 °C, as evidenced by the spectra represented in Figure 5.15, even though the porous structure of the starting material is completely different from that of

the fibers (see Figure 5.10). The activation with KOH breaks down the bimodal porous structure of the hemp shives, generating a single population of mesopores with rather homogeneous sizes.

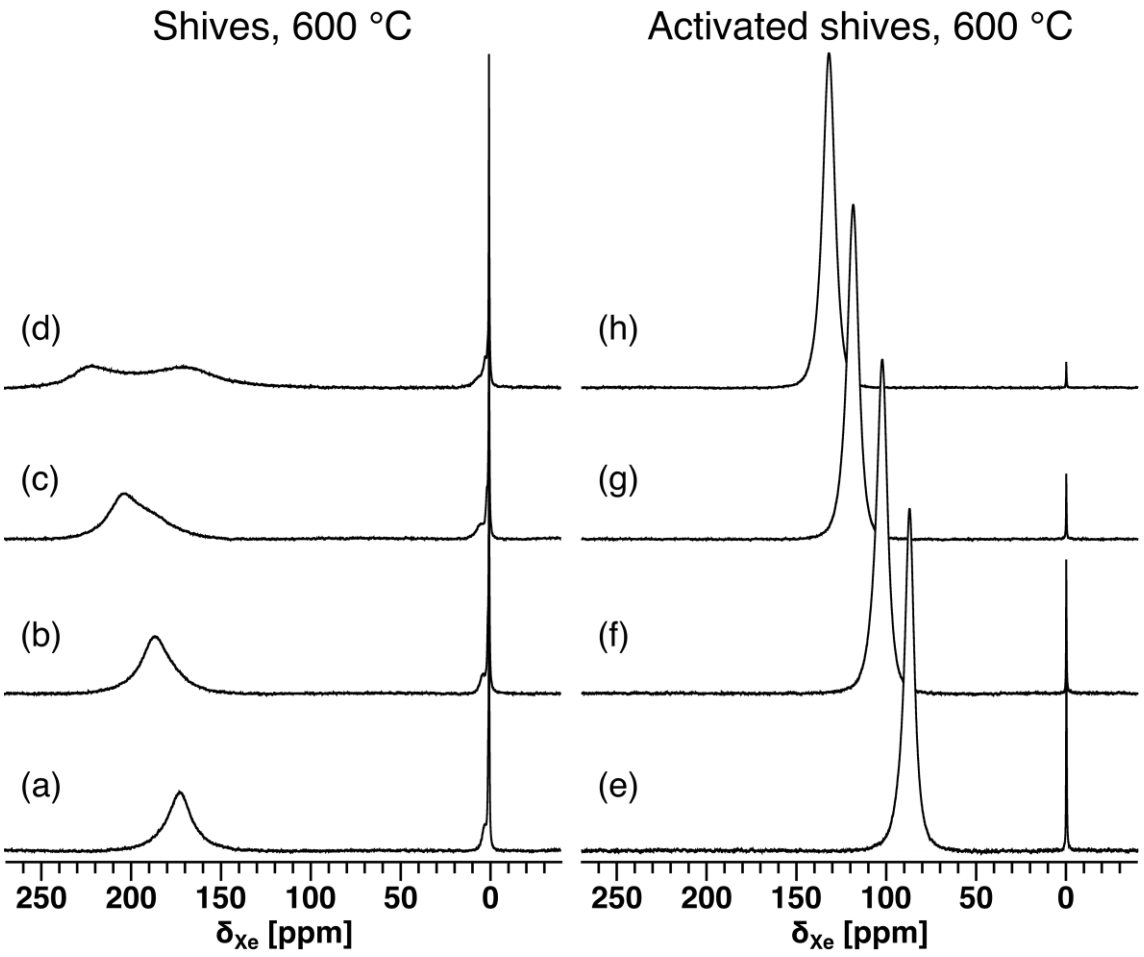

Figure 5.15. ^{129}Xe NMR spectra of hemp shives with a pyrolysis temperature of 600 °C, before (left) and after (right) activation with KOH. The spectra were acquired at (a, e) 298 K, (b, f) 278 K, (c, g) 258 K, and (d, h) 238 K.

Overall, these results show that the activation process significantly alters the morphology of the pyrolyzed materials, leading to a porous structure whose uniformity is influenced by the characteristics of the initial materials. Specifically, homogeneous mesoporous structures are obtained when the starting materials are pyrolyzed at 600 °C, while the activation of the fibers pyrolyzed at 400 °C generates a heterogeneous and bimodal structure, with pores ranging roughly from the small mesopore to the micropore range.

5.3.3.3 Electrocatalysts

Lastly, we performed the ^{129}Xe NMR measurements on the electrocatalysts prepared by functionalizing the activated materials with FePc. The ^{129}Xe NMR spectra, acquired at 278 K, of the electrocatalysts obtained from the starting materials pyrolyzed at different temperatures are represented in Figure 5.16.

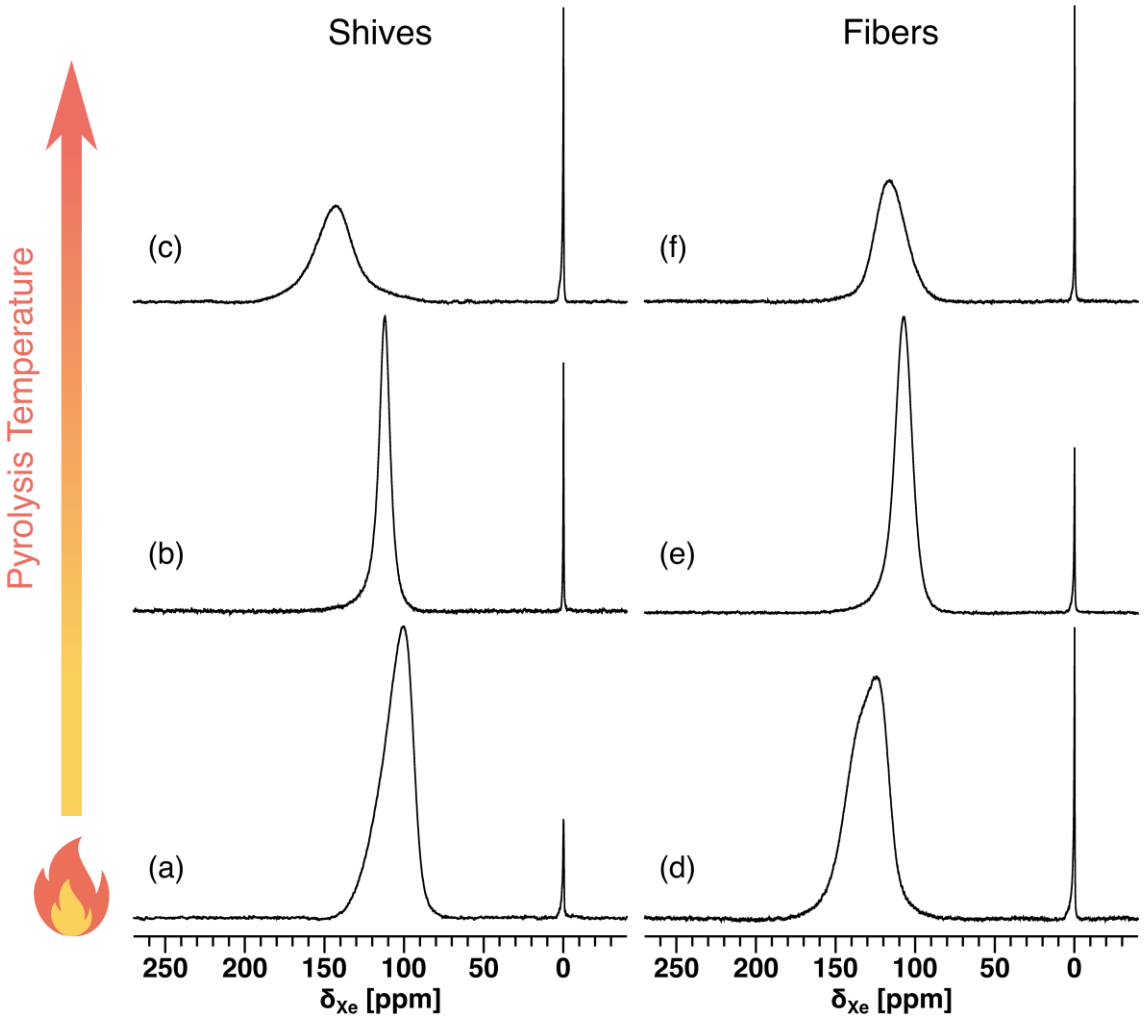

Figure 5.16. ^{129}Xe NMR spectra acquired at 278 K of electrocatalysts obtained from hemp shives (left) and fibers (right) pyrolyzed at (a, d) 400 °C, (b, e) 600 °C, and (c, f) 800 °C.

Single downfield peaks are evident in each spectrum, indicating that all the electrocatalysts possess a notable porous structure in the dimensional range detectable by xenon. For all samples, the pore sizes can be qualitatively estimated to fall within the

mesopore range, based on the chemical shifts of the peaks, between 100-150 ppm. The broadness of the peaks in Figure 5.16a, d, c, f reveals that the electrocatalysts obtained when the starting materials are pyrolyzed at 400 °C, and especially at 800 °C, have a heterogeneous morphology characterized by interconnected pores with different dimensions. Additionally, the downfield peaks in the spectra of samples pyrolyzed at 400 °C are asymmetric and skewed toward higher chemical shifts, denoting that, among the heterogenous pore structure, there is a significant number of small pores that fall into the small meso- or micropore range (Figure 5.16a, d).

In contrast, the peaks from the electrocatalysts obtained after the pyrolysis at 600 °C are sharper and only slightly asymmetric at the base (Figure 5.16b, e), suggesting that they have the most uniform porous structures along the series, similar to what observed for the activation process. Interestingly, these materials also showed the best electrocatalytic performances for the oxygen reduction reaction. The shives-based catalyst (HS600) achieved the highest E_{onset} and $E_{1/2}$, coupled with the lowest peroxide production among all the samples. The electrocatalyst obtained from fibers (HF600) had worse performance in terms of E_{onset} and $E_{1/2}$ but it maintained a low peroxide production and a high number of transferred electrons (see Table 5.2). These results indicate that a homogeneous porous structure is a favorable factor for the performance of the hemp-derived electrocatalysts. The morphological uniformity likely enhances the mass transport and the accessibility of the catalytic sites to the reactants and guarantees that the active sites are well distributed inside the electrocatalyst, leading to improved efficiency. By contrast, the heterogeneous porous structures of the other materials hinder the oxygen reduction reaction, resulting in worse electrocatalytic activities, especially in terms of peroxide production and number of transferred electrons (Table 5.2).

For all the samples, no significant variations of the peak shapes and no additional peaks were observed upon lowering the temperature. As an example, the variable temperature ^{129}Xe NMR spectra of the samples HS600 and HF600 are reported in Figure 5.17. It can be seen that the peak shape is retained across all temperatures from 298 K to 238 K. The only notable difference is the peak chemical shift which goes from 99 ppm and 95 ppm for the shives and fibers at 298 K, respectively, to 143 ppm and 125 ppm at 238 K. This is aligned with the slower gas dynamics at low temperatures which

in turn increase the residence time of xenon atoms on the surface of the pores, resulting in a chemical shift increase.

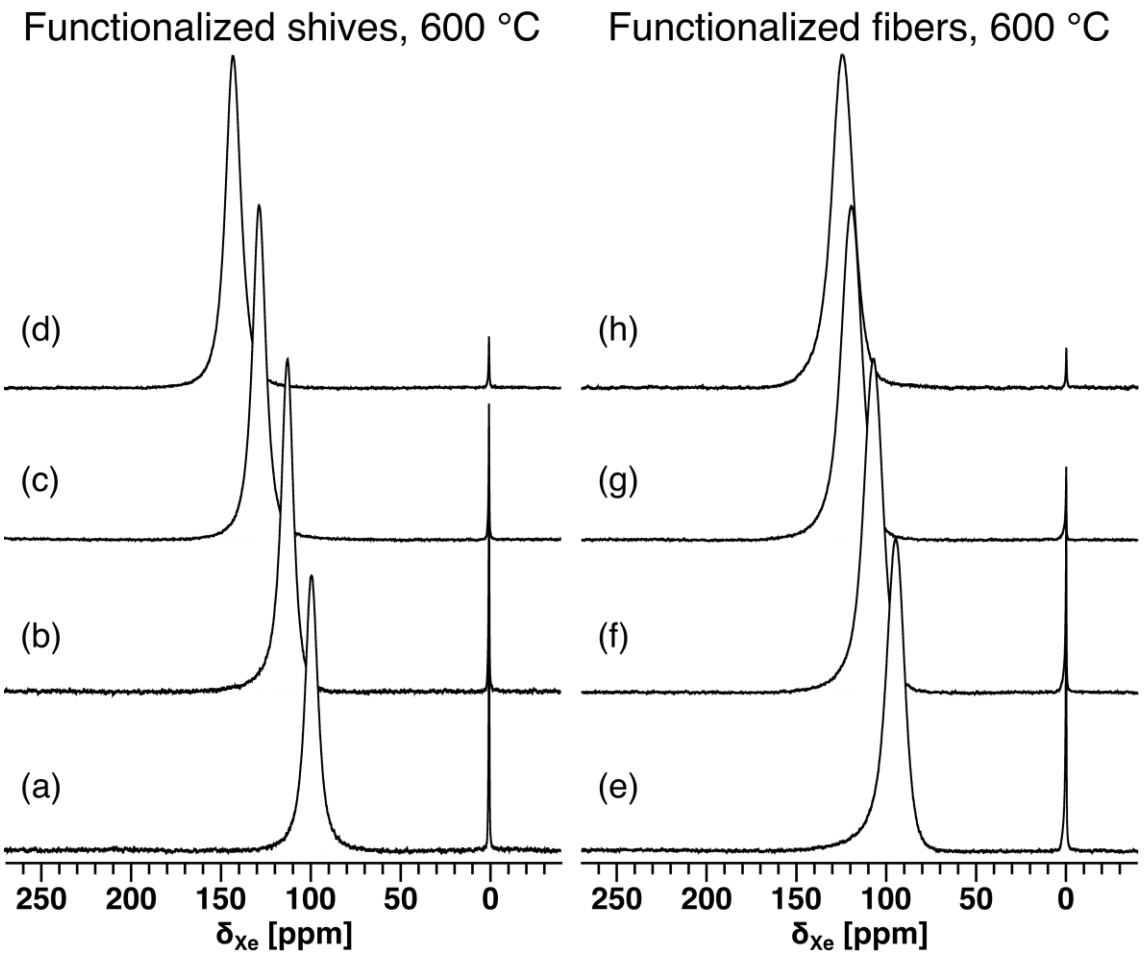

Figure 5.17. ^{129}Xe NMR spectra of electrocatalysts derived from (left) hemp shives and (right) hemp fibers pyrolyzed at 600 °C. The spectra were acquired at (a, e) 298 K, (b, f) 278 K, (c, g) 258 K, and (d, h) 238 K.

Notably, in the case of fibers pyrolyzed at 400 °C, the functionalization with FePc has a significant impact on the morphology of the corresponding activated material, as evidenced by the spectra acquired at 278 K (Figure 5.18). The spectrum of the activated material (Figure 5.18b) shows an intense peak at 127 ppm and a smaller downfield peak at 150 ppm which are related to a bimodal porous structure with significant segregation between the two pore populations, as discussed in Section 5.3.3.2. In the spectrum of the electrocatalyst (Figure 5.18c), the width of the peaks is significantly higher, and the smaller downfield peak is partially superimposed with the more intense central peak.

This indicates that functionalization increases the pore heterogeneity and decreases the segregation between the two pore populations. This effectively transforms the bimodal porous structure of the activated material into a heterogeneous distribution of mesopores in the electrocatalyst in which xenon atoms are able to exchange through all the different spaces during the NMR experiment.

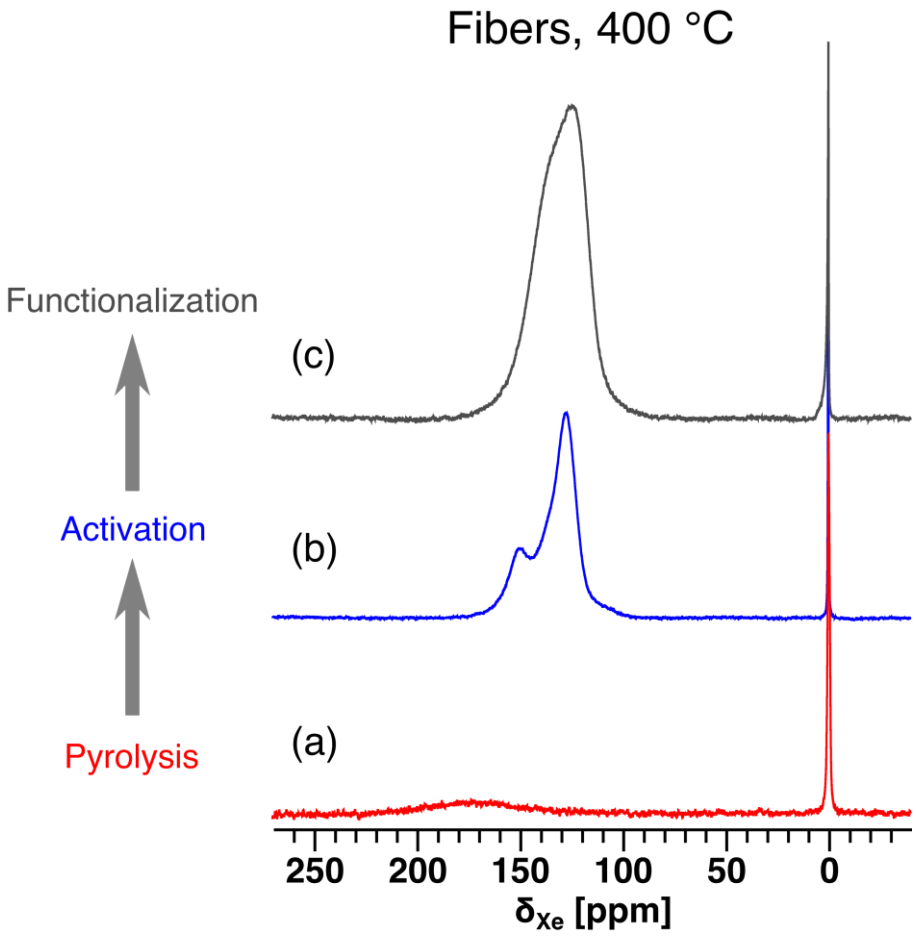

Figure 5.18. ^{129}Xe NMR spectra of hemp fibers (a) after pyrolysis at 400 °C, (b) after activation with KOH, and (c) after functionalization with FePc. The spectra were acquired at 278 K.

Figure 5.19 shows the ^{129}Xe NMR spectra, acquired at 278 K, of the most efficient electrocatalysts HS600 and HF600, along with the spectra of the corresponding pyrolyzed and activated materials. The red spectrum on the left (Figure 5.19a) shows that the hemp shives are porous immediately after pyrolysis. Variable temperature experiments reveal that the porous structure is bimodal and that the peak visible in

Figure 5.19a is an exchange signal (see Figure 5.10). After activation, the peak shifts upfield by 84 ppm, from 186 ppm to 102 ppm, and its line width decreases significantly, indicating that the basic treatment greatly increases the size of the pores while decreasing their segregation. On the other hand, after activation, the chemical shift has a slight increase, from 102 ppm to 112 ppm, along with the broadness of the peak. Thus, upon functionalizing the material with FePc, the average dimension of the voids is reduced, and their homogeneity is slightly decreased.

As discussed previously, the pyrolysis at 600 °C does not generate micro- or mesopores in the hemp fibers, while the activated material shows a distribution of interconnected mesopores. The morphology of the material remains almost unaltered even after functionalization, as clearly visible by comparing Figure 5.199e with Figure 5.19f. The only notable difference is a slight chemical shift decrease and a skewing of the peak towards higher chemical shifts, suggesting the presence of a significant portion of small pores in the distribution. These likely result from a slight reduction in the dimension of the mesopores upon functionalization, as observed in the case of hemp shives.

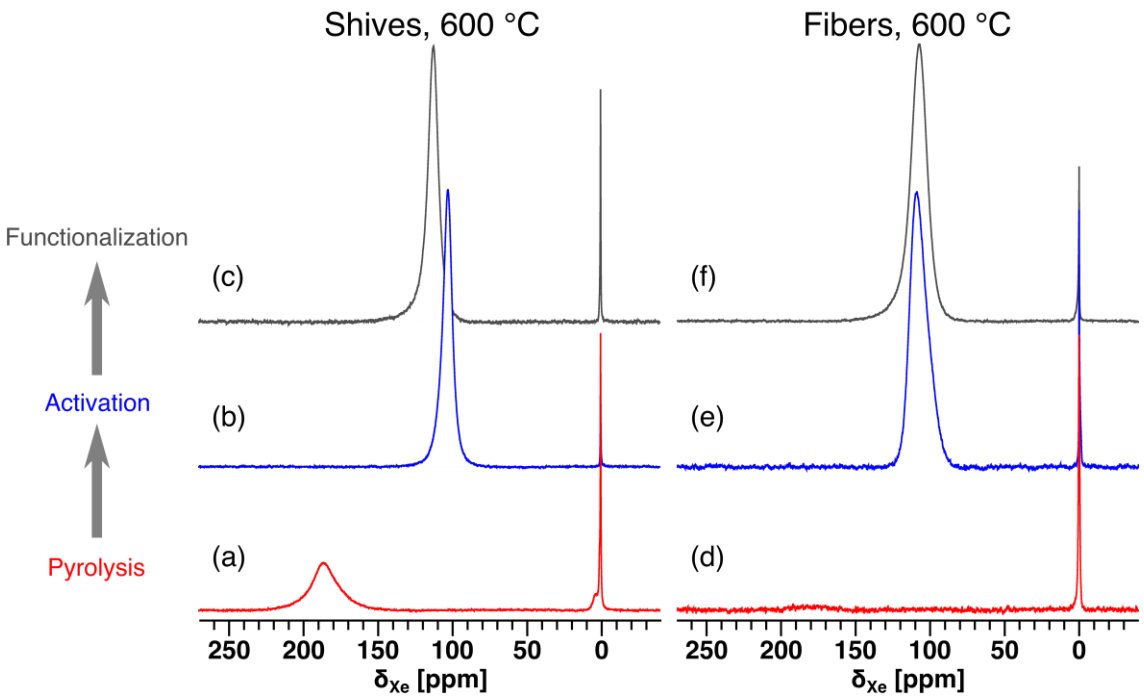

Figure 5.19. ^{129}Xe NMR spectra of (left) hemp shives and (right) hemp fibers (a, d) after pyrolysis at 600 °C, (b, e) after activation with KOH, and (c, f) after functionalization with FePc. The spectra were acquired at 278 K.

Overall, these results show that the materials pyrolyzed at 600 °C have the most homogeneous pore structure after the activation. This property is also retained after functionalization with FePc, resulting in an ideal morphology that enhances the electrocatalytic properties. The materials pyrolyzed at 400 °C and 800 °C exhibit heterogeneous porous structures, and in some cases, show a bimodal distribution after activation. Since the activation process plays a crucial role in determining the morphology of the electrocatalysts, these structures retain their heterogeneity even after functionalization. This results in non-ideal morphologies and worse electrocatalytic performance compared to the HS600 and HF600 electrocatalysts.

5.4 Conclusions

This work presents the successful preparation of novel hemp-based platinum group metal-free electrocatalysts for the oxygen reduction reaction in anion exchange membrane fuel cells. The two main parts constituting hemp stems, fibers and shives, were initially pyrolyzed at different temperatures and activated with a basic treatment to create biochar with interconnected porosity. The biochar was then functionalized with FePc to form monometallic electrocatalysts. XRD and Raman spectroscopy measurements indicated that the structure of the electrocatalysts was constituted by distorted graphitic layers containing a significant amount of Fe atoms. The presence of iron was also confirmed by XRF and XPS. Additionally, XPS analysis denoted that the electrocatalysts derived from hemp fibers had relatively higher iron and nitrogen content (0.7-0.9% and 4.1-4.8%, respectively) compared to those derived from hemp shives.

RRDE measurements in alkaline media, conducted with loadings of 0.2 mg cm^{-2} and 0.6 mg cm^{-2}, confirmed the activity of the electrocatalysts. In alkaline conditions, the HS600 and HF800 electrocatalysts outperformed the others in terms of E_{onset}, with values of 1.02 V and 1.00 V vs RHE, and $E_{1/2}$, with values of 0.91 V and 0.92 V vs RHE, respectively. Notably, HS600 and HF600 also produced the lowest amount of peroxide (7% and 9%, respectively) and achieved the highest electron transfer numbers (3.85 and 3.82, respectively). These materials also showed comparable or better

electrocatalytic performances compared to other electrocatalysts reported in the literature.

The porous structure and the morphology of the hemp-based materials were thoroughly studied by performing variable temperature ^{129}Xe NMR measurements after every single step of the electrocatalyst preparation. First, the materials pyrolyzed at different temperatures were analyzed, determining that pyrolysis created a significant porous structure only in the hemp shives and in the hemp fibers treated at 600 °C and 800 °C, respectively. Variable temperature measurements revealed that these materials had a heterogeneous bimodal porous structure ranging from small mesopores to micropores.

^{129}Xe NMR spectra on some of the activated materials demonstrated that the basic treatment was the key to obtaining significant porous structures, which are essential for good catalytic activity. The morphological features of the activated materials were found to depend strongly on the type of starting material and on the pyrolysis temperature. For example, after activation, the non-porous structure of the fibers pyrolyzed at 400 °C was transformed into a bimodal porous structure with significant separation between the pores. Hemp fibers and shives pyrolyzed at 600 °C, on the other hand, showed more homogeneous mesoporous structures after the treatment with KOH.

The latter materials maintained their morphological features even after the functionalization with FePc, resulting in the electrocatalysts with the most homogeneous porous structures. Notably, these electrocatalysts, named HS600 and HF600, also showed the best catalytic performances, especially in terms of peroxide production and number of transferred electrons. This was attributed to the favorable morphology which enhances mass transport and accessibility to the catalytic sites. On the other hand, the electrocatalysts obtained with different substrates showed less homogeneous structures with broad pore size distributions, which led to worse electrochemical performances.

These results emphasize the potential of xenon NMR in elucidating the morphological history of porous bio-based materials undergoing different treatments. This technique allows to study morphology, pore size distribution, connectivity, and pore blocking with a high level of detail, providing a solid base for the development of structure-property relationships for electrocatalytic materials.

Overall, this Chapter highlights the use of a new biomass raw material for the cost-effective development of electrocatalysts with appropriate physicochemical properties for the oxygen reduction reaction in anion exchange membrane fuel cells.

5.5 Bibliography

[1] P. K. Pathak, A. K. Yadav, S. Padmanaban, *Int. J. Hydrogen Energy* **2023**, *48*, 9921–9927.

[2] C. Song, *Catal. Today* **2002**, *77*, 17–49.

[3] EG&G Technical Services Inc., *Fuel Cell Handbook*, Lulu Press, **2016**.

[4] K. Jiao, J. Xuan, Q. Du, Z. Bao, B. Xie, B. Wang, Y. Zhao, L. Fan, H. Wang, Z. Hou, S. Huo, N. P. Brandon, Y. Yin, M. D. Guiver, *Nature* **2021**, *595*, 361–369.

[5] X. Ren, Q. Lv, L. Liu, B. Liu, Y. Wang, A. Liu, G. Wu, *Sustain. Energy Fuels* **2019**, *4*, 15–30.

[6] X. Ren, Y. Wang, A. Liu, Z. Zhang, Q. Lv, B. Liu, *J. Mater. Chem. A* **2020**, *8*, 24284–24306.

[7] S. Hussain, H. Erikson, N. Kongi, A. Sarapuu, J. Solla-Gullón, G. Maia, A. M. Kannan, N. Alonso-Vante, K. Tammeveski, *Int. J. Hydrogen Energy* **2020**, *45*, 31775–31797.

[8] Z. Ma, Z. P. Cano, A. Yu, Z. Chen, G. Jiang, X. Fu, L. Yang, T. Wu, Z. Bai, J. Lu, *Angew. Chemie - Int. Ed.* **2020**, *59*, 18334–18348.

[9] J. Zhang, Y. Yuan, L. Gao, G. Zeng, M. Li, H. Huang, *Adv. Mater.* **2021**, *33*, 6.

[10] A. Kostuch, I. A. Rutkowska, B. Dembinska, A. Wadas, E. Negro, K. Vezzù, V. Di Noto, P. J. Kulesza, *Molecules* **2021**, *26*, DOI 10.3390/molecules26175147.

[11] M. Liu, X. Xiao, Q. Li, L. Luo, M. Ding, B. Zhang, Y. Li, J. Zou, B. Jiang, *J. Colloid Interface Sci.* **2022**, *607*, 791–815.

[12] X. Li, D. Wang, S. Zha, Y. Chu, L. Pan, M. Wu, C. Liu, W. Wang, N. Mitsuzaki, Z. Chen, *Int. J. Hydrogen Energy* **2024**, *51*, 1110–1127.

[13] J. R. Varcoe, P. Atanassov, D. R. Dekel, A. M. Herring, M. A. Hickner, P. A. Kohl, A. R. Kucernak, W. E. Mustain, K. Nijmeijer, K. Scott, T. Xu, L. Zhuang, *Energy Environ. Sci.* **2014**, *7*, 3135–3191.

[14] D. R. Dekel, *J. Power Sources* **2018**, *375*, 158–169.

[15] S. Gottesfeld, D. R. Dekel, M. Page, C. Bae, Y. Yan, P. Zelenay, Y. S. Kim, *J. Power Sources* **2018**, *375*, 170–184.

[16] J. Hyun, H. T. Kim, *Energy Environ. Sci.* **2023**, *16*, 5633–5662.

[17] G. Wu, P. Zelenay, *Acc. Chem. Res.* **2013**, *46*, 1878–1889.

[18] G. Wu, A. Santandreu, W. Kellogg, S. Gupta, O. Ogoke, H. Zhang, H. L. Wang, L. Dai, *Nano Energy* **2016**, *29*, 83–110.

[19] X. Huang, T. Shen, T. Zhang, H. Qiu, X. Gu, Z. Ali, Y. Hou, *Adv. Energy Mater.* **2020**, *10*, 6.

[20] M. M. Hossen, M. S. Hasan, M. R. I. Sardar, J. bin Haider, Mottakin, K. Tammeveski, P. Atanassov, *Appl. Catal. B Environ.* **2023**, *325*, DOI 10.1002/aenm.201900375.

[21] L. Du, G. Zhang, X. Liu, A. Hassanpour, M. Dubois, A. C. Tavares, S. Sun, *Carbon Energy* **2020**, *2*, 561–581.

[22] S. Zago, L. C. Scarpetta-Pizo, J. H. Zagal, S. Specchia, *Electrochem. Energy Rev.* **2024**, *7*, DOI 10.1007/s41918-023-00197-3.

[23] X. Y. Song, G. X. Pan, Y. W. Bai, F. Liang, J. J. Xing, J. Gao, F. N. Shi, *Fullerenes Nanotub. Carbon Nanostructures* **2019**, *27*, 453–458.

[24] R. Gabhi, L. Basile, D. W. Kirk, M. Giorcelli, A. Tagliaferro, C. Q. Jia, *Biochar* **2020**, *2*, 369–378.

[25] M. Muhyuddin, A. Friedman, F. Poli, E. Petri, H. Honig, F. Basile, A. Fasolini, R. Lorenzi, E. Berretti, M. Bellini, A. Lavacchi, L. Elbaz, C. Santoro, F. Soavi, *J. Power Sources* **2023**, *556*, DOI 10.1016/j.jpowsour.2022.232416.

[26] M. Muhyuddin, D. Testa, R. Lorenzi, G. M. Vanacore, F. Poli, F. Soavi, S. Specchia, W. Giurlani, M. Innocenti, L. Rosi, C. Santoro, *Electrochim. Acta* **2022**, *433*, DOI 10.1016/j.electacta.2022.141254.

[27] M. Muhyuddin, J. Filippi, L. Zoia, S. Bonizzoni, R. Lorenzi, E. Berretti, L. Capozzoli, M. Bellini, C. Ferrara, A. Lavacchi, C. Santoro, *ChemSusChem* **2022**, *15*, DOI 10.1002/cssc.202102351.

[28] S. Muangmeesri, N. Li, D. Georgouvelas, P. Ouagne, V. Placet, A. P. Mathew, J. S. M. Samec, *ACS Sustain. Chem. Eng.* **2021**, *9*, 17207–17213.

[29] S. Liu, L. Ge, S. Gao, L. Zhuang, Z. Zhu, H. Wang, *Compos. Commun.* **2017**, *5*, 27–30.

[30] C. Zhang, J. Shu, S. Shi, J. Nie, G. Ma, *J. Colloid Interface Sci.* **2020**, *559*, 21–28.

[31] J. Demarquay, J. Fraissard, *Chem. Phys. Lett.* **1987**, *136*, 314–318.

[32] J. Fraissard, T. Ito, *Zeolites* **1988**, *8*, 350–361.

[33] R. Ryoo, C. Pak, B. F. Chmelka, *Zeolites* **1990**, *10*, 790–793.

[34] A. Gedeon, R. Burmeister, R. Grosse, B. Boddenberg, J. Fraissard, *Chem. Phys. Lett.* **1991**, *179*, 191–194.

[35] I. L. Moudrakovski, C. I. Ratcliffe, J. A. Ripmeester, *J. Am. Chem. Soc.* **1998**, *120*, 3123–3132.

[36] V. V. Terskikh, I. L. Mudrakovskii, V. M. Mastikhin, *J. Chem. Soc. Faraday Trans.* **1993**, *89*, 4239–4243.

[37] I. L. Moudrakovski, V. V. Terskikh, C. I. Ratcliffe, J. A. Ripmeester, L. Q. Wang, Y. Shin, G. J. Exarhos, *J. Phys. Chem. B* **2002**, *106*, 5938–5946.

[38] S. J. Huang, C. H. Huang, W. H. Chen, X. Sun, X. Zeng, H. K. Lee, J. A. Ripmeester, C. Y. Mou, S. Bin Liu, *J. Phys. Chem. B* **2005**, *109*, 681–684.

[39] N. Mnasri, C. Charnay, L. C. De Ménorval, Y. Moussaoui, E. Elaloui, J. Zajac, *Microporous Mesoporous Mater.* **2014**, *196*, 305–313.

[40] D. Schneider, A. G. Attallah, S. Wassersleben, M. Wenzel, J. Matysik, R. Krause-Rehberg, D. Enke, *Microporous Mesoporous Mater.* **2020**, *307*, 110515.

[41] J. D. Barboza-Carmona, M. Wenzel, L. Eckert, D. Enke, J. Matysik, I. F. Céspedes-Camacho, *J. Sol-Gel Sci. Technol.* **2022**, *101*, 176–184.

[42] J. B. Miller, J. H. Walton, C. M. Roland, *Macromolecules* **1993**, *26*, 5602–5610.

[43] K. J. McGrath, C. M. Roland, *Rubber Chem. Technol.* **1994**, *67*, 629–635.

[44] E. Locci, P. Roose, K. Bartik, M. Luhmer, *J. Colloid Interface Sci.* **2009**, *330*, 344–351.

[45] H. Yoshimizu, S. Ohta, T. Asano, T. Suzuki, Y. Tsujita, *Polym. J.* **2012**, *44*, 821–826.

[46] H. Mikami, S. Higashi, T. Muramoto, M. Tanaka, M. Yamato, H. Kawakami, *J. Photopolym. Sci. Technol.* **2020**, *33*, 313–320.

[47] M. Mansfeld, W. S. Veeman, *Chem. Phys. Lett.* **1994**, *222*, 422–424.

[48] M. Mansfeld, A. Flohr, W. S. Veeman, *Appl. Magn. Reson.* **1995**, *8*, 573–586.

[49] S. Schantz, W. S. Veeman, *J. Polym. Sci. Part B Polym. Phys.* **1997**, *35*, 2681–

2688.

[50] T. Miyoshi, K. Takegoshi, T. Terao, *Polymer (Guildf).* **1997**, *38*, 5475–5480.

[51] D. R. Morgan, E. O. Stejskal, A. L. Andrady, *Macromolecules* **1999**, *32*, 1897–1903.

[52] T. Suzuki, M. Miyauchi, H. Yoshimizu, Y. Tsujita, *Polym. J.* **2001**, *33*, 934–938.

[53] M. Wachowicz, J. Wolak, H. Gracz, E. O. Stejskal, S. Jurga, E. F. McCord, J. L. White, *Macromolecules* **2004**, *37*, 4573–4579.

[54] K. M. Varcoe, I. Blakey, T. V. Chirila, A. J. Hill, A. K. Whittaker, *ACS Symp. Ser.* **2007**, *963*, 391–409.

[55] C. F. M. Clewett, T. Pietraß, *J. Phys. Chem. B* **2005**, *109*, 17907–17912.

[56] K. V. Romanenko, J. B. D'Espinose De La Caillerie, J. Fraissard, T. V. Reshetenko, O. B. Lapina, *Microporous Mesoporous Mater.* **2005**, *81*, 41–48.

[57] T. Onfroy, F. Guenneau, M. A. Springuel-Huet, A. Gédéon, *Carbon N. Y.* **2009**, *47*, 2352–2357.

[58] M. Oschatz, H. C. Hoffmann, J. Pallmann, J. Schaber, L. Borchardt, W. Nickel, I. Senkovska, S. Rico-Francés, J. Silvestre-Albero, S. Kaskel, E. Brunner, *Chem. Mater.* **2014**, *26*, 3280–3288.

[59] M. Mauri, M. Farina, G. Patriarca, R. Simonutti, K. T. Klasson, H. N. Cheng, *Int. J. Polym. Anal. Charact.* **2015**, *20*, 119–129.

[60] M. Farina, M. Mauri, G. Patriarca, R. Simonutti, K. T. Klasson, H. N. Cheng, *RSC Adv.* **2016**, *6*, 103803–103810.

[61] M. Muhyuddin, D. Testa, R. Lorenzi, G. M. Vanacore, F. Poli, F. Soavi, S. Specchia, W. Giurlani, M. Innocenti, L. Rosi, C. Santoro, *Electrochim. Acta* **2022**, *433*, 141254.

[62] D. Testa, G. Zuccante, M. Muhyuddin, R. Landone, A. Scommegna, R. Lorenzi, M. Acciarri, E. Petri, F. Soavi, L. Poggini, L. Capozzoli, A. Lavacchi, N. Lamanna, A. Franzetti, L. Zoia, C. Santoro, *Catalysts* **2023**, *13*, DOI 10.3390/catal13030635.

[63] N. Giulini, M. Muhyuddin, S. Mattiello, M. Sassi, C. Lo Vecchio, V. Baglio, E. Berretti, A. Lavacchi, E. Fazio, L. Beverina, C. Santoro, *Electrochim. Acta* **2024**, *507*, DOI 10.1016/j.electacta.2024.145113.

[64] M. A. Pimenta, G. Dresselhaus, M. S. Dresselhaus, L. G. Cançado, A. Jorio, R.

Saito, *Phys. Chem. Chem. Phys.* **2007**, *9*, 1276–1291.

[65] G. Zuccante, M. Muhyuddin, V. C. A. Ficca, E. Placidi, M. Acciarri, N. Lamanna, A. Franzetti, L. Zoia, M. Bellini, E. Berretti, A. Lavacchi, C. Santoro, *ChemElectroChem* **2024**, *11*, DOI 10.1002/celc.202300725.

[66] S. Zago, M. Bartoli, M. Muhyuddin, G. M. Vanacore, P. Jagdale, A. Tagliaferro, C. Santoro, S. Specchia, *Electrochim. Acta* **2022**, *412*, DOI 10.1016/j.electacta.2022.140128.

[67] M. Muhyuddin, N. Zocche, R. Lorenzi, C. Ferrara, F. Poli, F. Soavi, C. Santoro, *Mater. Renew. Sustain. Energy* **2022**, *11*, 131–141.

[68] S. Pawsey, K. K. Kalebaila, I. Moudrakovski, J. A. Ripmeester, S. L. Brock, *J. Phys. Chem. C* **2010**, *114*, 13187–13195.

6. General conclusions

The objective of this Thesis was to explore the multifaceted applications of ^{129}Xe NMR spectroscopy, demonstrating its versatility and effectiveness in elucidating structural and dynamic properties across a variety of complex systems and materials, from simple liquids to complex mixtures, and from supramolecular complexes to porous electrocatalysts.

Chapter 1 briefly introduced the fundamental principles of nuclear magnetic resonance, highlighting the quantum mechanical interactions that constitute the basis of this powerful technique. The phenomenon of NMR relaxation and the associated mechanisms were also introduced, along with some instrumental aspects and techniques of NMR. Lastly, an introduction to ^{129}Xe NMR spectroscopy was provided, highlighting history, physical description, and applications.

Chapter 2 aimed to expand the fundamental knowledge of the NMR of xenon dissolved in liquids by applying this technique to investigate the liquid structure of dihalomethanes. The combination of experimental data with computational calculations allowed correlating the ^{129}Xe NMR parameters with the structural and dynamic properties of these solvents, emphasizing the role of the xenon-halogen interactions. This Chapter highlighted the potential of a combined experimental and computational approach in studying the physical phenomena that determine the NMR parameters of dissolved xenon and the broader aspects of solvation and solution dynamics.

In Chapter 3, ^{129}Xe NMR was employed to investigate the porous structure of Noria-OEt type II porous liquids. A three-site model was developed to explain the xenon interactions and the complex porous topology of these materials. The study revealed the presence of both intrinsic and extrinsic porosity in the synthesized liquids, generated by the structural indentations of the paddlewheel-like structure of Noria-OEt. The Chapter highlighted the potential of ^{129}Xe NMR in the challenging characterization of porous liquids, particularly in applications related to gas capture and separation.

Chapter 4 demonstrates the applicability of ^{129}Xe NMR in characterizing the structure of deep eutectic solvents and eutectic mixtures. The results revealed how variations in chemical composition influence the free volume and liquid structure. Moreover, it was found that deep eutectic solvents have less free volume available to

xenon due to a more efficient packing of the components. This proof-of-concept Chapter highlights the potential of ^{129}Xe NMR to provide valuable insights into the complex structures of deep eutectic solvents and mixtures, potentially aiding in the understanding of their thermodynamic non-ideality and in the design of efficient solvents for applications such as gas capture and separation.

Finally, Chapter 5 reported the innovative use of hemp-based biochar to prepare platinum group metal-free electrocatalysts for the oxygen reduction reaction. By employing ^{129}Xe NMR, the morphological history of the various biochar throughout the electrocatalyst preparation process were thoroughly analyzed, linking the structural characteristics to the final catalytic performance. This work not only emphasizes the potential of biomass as a raw material for sustainable energy solutions but also illustrates the role of ^{129}Xe NMR in advancing the understanding of structure-property relationships in electrocatalytic materials.

In conclusion, this Thesis demonstrates the power of ^{129}Xe NMR spectroscopy as a tool for investigating the complex structures and dynamics of widely different materials. The insights gained from this research not only contribute to the fundamental understanding of NMR phenomena but also offer practical implications for the development of novel materials in fields such as solution science, porous solids and liquids, and catalysis. Future research can build on these findings, exploring additional applications of ^{129}Xe NMR in novel systems and further enhancing our understanding of their properties.

List of publications

Boventi, M.; Mauri, M.; Simonutti, R. 129Xe: A Wide-Ranging NMR Probe for Multiscale Structures. *Appl. Sci.* **2022**, *12* (6), 3152.

Boventi, M.; Mauri, M.; Golker, K.; Wiklander, J. G.; Nicholls, I. A.; Simonutti, R. Porosity of Molecularly Imprinted Polymers Investigated by 129Xe NMR Spectroscopy. *ACS Appl. Polym. Mater.* **2022**, *4* (12), 8740–8749.

Boventi, M.; Mazzilli, V.; Simonutti, R.; Castiglione, F.; Saielli, G. Exploring the Structure of Halomethanes with Xenon: An NMR and MD Investigation. *J. Mol. Liq.* **2023**, *382* (April), 122011.

Boventi, M.; Mauri, M.; Alexander, F.; James, S. L.; Simonutti, R.; Castiglione, F. Exploring Cavities in Type II Porous Liquids with Xenon. *J. Mol. Liq.* **2023**, *370*, 121038.

Boventi, M.; Mauri, M.; Castiglione, F.; Simonutti, R. Exploring the Structure of Type V Deep Eutectic Solvents by Xenon NMR Spectroscopy. *Faraday Discuss.* **2024**, Advance Article.

Bellotti, V.; Carulli, F.; Mecca, S.; Zaffalon, M. L.; Erroi, A.; Catalano, F.; Boventi, M.; Infante, I.; Rossi, F.; Beverina, L.; Brovelli, S.; Simonutti, R. Perovskite Nanocrystals Initiate One-Step Oxygen Tolerant PET-RAFT Polymerization of Highly Loaded, Efficient Plastic Nanocomposites. *Adv. Funct. Mater.* **2024**, *2411319*, 1–9.

Acknowledgements

For this work, I would like to thank my supervisor, Prof. Roberto Simonutti, for all the opportunities he has given me over the years, not only during my PhD but also beforehand, and for guiding me in my professional growth. I also want to thank Prof. Michele Mauri, to whom I owe a great deal of what I have learned over these years, and Prof. Franca Castiglione for supporting me in various research projects and for teaching me much of what I know about NMR.

I extend my gratitude to all the people with whom I have had the opportunity and pleasure to collaborate: Dr. Giacomo Saielli, PhD, and Valerio Mazzilli for the project on the study of dihalomethanes; Prof. Stuart L. James and Dr. Francesca Alexander, PhD, for preparing and providing me with the fascinating samples of porous liquids; Prof. Carlo Santoro and Dr. Leire Caizán-Juanarena, PhD, for the preparation of electrocatalysts, their characterization, and the invaluable discussions.

Finally, I want to deeply thank all the current and former members of the PoSyLife research group with whom I shared the daily work. Thank you for your help and for the valuable discussions.